

CHEMO-THERMO-MECHANICAL MODELING OF HETEROGENEOUS  
REACTIVE MATERIALS

A Dissertation

Submitted to the Graduate School  
of the University of Notre Dame  
in Partial Fulfillment of the Requirements  
for the Degree of

Doctor of Philosophy

by

Cedric W. Williams

---

Karel Matouš, Director

Graduate Program in Aerospace and Mechanical Engineering

Notre Dame, Indiana

April 2023

This document is in the public domain.

# CHEMO-THERMO-MECHANICAL MODELING OF HETEROGENEOUS REACTIVE MATERIALS

Abstract

by

Cedric W. Williams

Heterogeneous reactive materials are relevant for a variety of scientific and engineering fields. Modeling these complicated systems often requires highly advanced mathematical models, cutting edge numerical algorithms and implementations, and intensive calibration thereof. Much effort has been made in accomplishing these tasks. This has led to a great deal of progress in the modeling and simulation of these material systems which, in turn, has led to vast improvements in the physical understanding of the various mechanisms at play. However, these efforts are often limited by issues with thermodynamic consistency, the inherent nonlinearity of the relevant fields of interest (chemical species, temperature, deformation, etc.), and complex physical coupling between said fields.

To this end, this dissertation develops a chemo-thermal-mechanical model that considers phase transition phenomena, heat generation due to chemical reactions and mechanical deformations, and finite strain elasto-plastic behavior. The dissertation also develops numerical algorithms for the computational implementation of the model which are developed as a state-of-the-art finite element solver. The model is calibrated using available experimental data, then applied to the  $\beta \rightarrow \delta$  phase transition of single crystal HMX as well as to HMX based PBXs.

To the friends who got me here, I owe you everything and more for being the cornerstones of my foundation. Katie Huang, Jordon Lewis, and Annelise Bergeron, where would I be without your love and support.

To the friends who've kept me here, including the entire #Martes crew, I owe you so much for who I am today. Ricardo 'Lord and Savior' Romero Moreno, Elvin 'Manny No Morals' Perez, and Antonio 'Two Toes' Martinez, you were the best friends a guy could ever ask for. You were there for me in the best of times and in the worst of times, you took me in, you supported me, and you went above and beyond; I owe you all the world and so much more. Trés Leches is eternal.

To Josephine, I am eternally grateful to you for giving me so much to live for during our time together. Je vais jamais oublier l'amour que nous avons partagé. Sans cela, je serais certainement pas arrivé là où je suis aujourd'hui. Tu sais bien que je vais toujours t'aimer. Et bien sûr, merci a toi aussi petit Nouni.

Finally, thank you Mom, Dad, Kaylia, Ebony, and the rest of my family for being there whenever I needed you. I love you all, and can't wait to answer your calling me home.

I wish I could thank everyone, but I really would never graduate. Thank you everyone – even if I didn't put your name, rest assured that I am endlessly grateful for all that you've done for me.

## CONTENTS

Figures . . . . .	v
Tables . . . . .	ix
Symbols and Abbreviations . . . . .	x
Acknowledgments . . . . .	xv
Chapter 1: Introduction . . . . .	1
1.1 Motivation for the Modeling of Single Crystal HMX Phase Transition . . . . .	2
1.2 Motivation for the Modeling of Phase Transition in HMX Based PBXs . . . . .	4
1.3 Literature Review . . . . .	5
1.3.1 Chemo-thermo-mechanical Modeling . . . . .	5
1.3.2 Single Crystal HMX . . . . .	7
1.3.3 HMX Based PBXs . . . . .	8
1.4 Novelty of this Dissertation . . . . .	9
1.5 Dissertation Overview . . . . .	11
Chapter 2: Chemo-thermo-mechanical Model of Phase Change Materials . . . . .	13
2.1 Governing Equations . . . . .	13
2.2 Constitutive Equations . . . . .	17
2.3 Thermodynamics . . . . .	19
Chapter 3: Model Specification . . . . .	26
3.1 Chemistry . . . . .	26
3.2 Thermodynamics . . . . .	27
3.3 Mechanics . . . . .	28
Chapter 4: Numerical Implementation . . . . .	31
4.1 Chemo-thermal Solver Spatial Discretization . . . . .	31
4.2 Mechanical Solver Spatial Discretization . . . . .	32
4.2.1 Three-field de Veubeke-Hu-Washizu Variational Principle . . . . .	32
4.2.2 Generalized Plane Strain Condition . . . . .	34
4.3 Temporal Discretization . . . . .	35
4.3.1 Adaptive Time Stepping . . . . .	35

4.3.2	Staggered Solution Strategy . . . . .	36
4.3.3	Chemical Integration Algorithm . . . . .	38
4.3.4	Plastic Integration Algorithm . . . . .	38
4.3.5	High Performance Computing . . . . .	44
Chapter 5:	Model Calibration . . . . .	46
5.1	Chemistry . . . . .	46
5.2	Thermodynamics . . . . .	49
5.3	Mechanics . . . . .	49
5.4	Summary of Material Properties . . . . .	53
Chapter 6:	Modeling of Single Crystal HMX . . . . .	56
6.1	Model Setting . . . . .	56
6.2	Simulation Results . . . . .	59
Chapter 7:	Modeling of HMX Based PBXs . . . . .	67
7.1	Model Setting . . . . .	67
7.2	Simulation Results . . . . .	71
7.2.1	Effect of Particle Volume Fraction . . . . .	78
7.2.2	Effect of Boundary Heating Rate . . . . .	81
Chapter 8:	Conclusions . . . . .	84
8.1	Summary of Contributions . . . . .	84
8.2	Future Directions . . . . .	86
Appendix A:	Lagrangian Frame Representation . . . . .	88
A.1	Conservation of Energy . . . . .	88
A.2	Conservation of Linear Momentum . . . . .	91
A.3	Plastic Integration Algorithm . . . . .	93
Appendix B:	Chemo-thermal Model in Limit of Spatial Homogeneity . . . . .	96
Bibliography	. . . . .	99

## FIGURES

2.1	Kinematics of the framework. . . . .	14
4.1	Graphical depiction of the prescribed adaptive time step. . . . .	36
4.2	Diagram of the CTM solver algorithm. . . . .	37
4.3	A plot of the percent decrease in computation time as a function of the number of threads for the generalized finite element routines (GFEM) and total time (GFEM, linear solvers, input, and output). . . . .	45
5.1	Calibration for the corrective factor, $\hat{A}$ , and the enthalpy of reaction, $\Delta h^{\text{rxn}}$ using the chemical heating, $q_c$ . The markers indicate experimental data points, while the curves are plots of the model using the resultant calibrated parameters. . . . .	48
5.2	Plots of the model of the $\delta$ -HMX mass fraction, $y_\delta$ , given by Eq. 3.2 using the parameters given by the calibration (solid lines) along with experimental conversion data (markers) provided in [97]. . . . .	49
5.3	Calibration of the nonlinear CTE, $\alpha$ , of HMX crystals using dimensional change, $\Delta L$ , (left) and a plot of the resultant (reduced) CTE and its derivative (right). . . . .	51
5.4	Calibration of the mechanical properties of HMX (left) and Viton (right). Here, $\sigma$ and $\varepsilon$ are uniaxial stress and strain, respectively, while $\kappa$ is the bulk modulus. . . . .	53
6.1	A log-log plot of the $L_2$ error in temperature, $\theta$ , computed in a self convergence study. . . . .	57
6.2	(left) A plot showing how the reaction zone thickness, $\Delta_{\text{rxn}}$ , is approximated and (right) a plot showing how the wave speed is approximated. . . . .	58
6.3	Diagram of the HMX single crystal computational domain. Also included are the computational thermal and mechanical boundary conditions. The temperature rate at the boundaries, $\dot{\theta}_\Gamma$ , is one of 1, 5, or 10 [K/min]. . . . .	59
6.4	A plot of the percent change of the sample volume as a function of boundary temperature. Here, $\Delta V/V_0$ refers to the change in volume of with respect to initial volume $V_0$ . Compare to the dimensional change of the first heating cycle in Fig. 2 of [96]. . . . .	60
6.5	A plot of the axial Cauchy stress components showing virtually isotropic response. . . . .	61

6.6	(a) Specific heats at constant pressure and volume as functions of temperature. Horizontal dotted lines indicate the respective reference quantities ${}^0c_p$ and ${}^0c_v$ . (b) The temperature rate as a function of average cell temperature. Both results are from the simulation with 5 [K/min] boundary temperature rate. . . . .	63
6.7	(a) A contour plot of specific heat at constant pressure, $c_p$ . (b) A contour plot of specific heat at constant volume, $c_v$ . Both plots are at the point in the simulation where the boundary temperature, $\theta_\Gamma$ , approximately equals the transition temperature, $\theta_T$ . . . . .	64
6.8	(a) Chemical heating rate as a function of temperature and (b) critical temperature for the chemical heating rate as a function of boundary heating rate. . . . .	65
6.9	(a) A contour plot of the chemical heating. (b) A contour plot of the elastic heating. Both plots are at the point in the simulation where the boundary temperature, $\theta_\Gamma$ , approximately equals the transition temperature, $\theta_T$ . . . . .	66
7.1	Data and fit to determine trimodal particle size distribution. The experimental distribution data is provided by Skidmore et al. [81] in terms of volume percent as a function of particle diameter. The calculated expectation values of each shaded region, from left to right, are $E_1(r) = 24.4 [\mu\text{m}]$ , $E_2(r) = 107 [\mu\text{m}]$ , and $E_3(r) = 295 [\mu\text{m}]$ with associated probabilities $P_1 = 11\%$ , $P_2 = 73\%$ , and $P_3 = 16\%$ , respectively. . . . .	69
7.2	One microstructure for a volume fraction of 50%. Each sample contains randomly placed HMX particles following the trimodal distribution, within a domain of size $4.0 \text{ mm}^2$ . Also included are the computational thermal and mechanical boundary conditions and the finite element mesh. The temperature rate $\dot{\theta}_\Gamma$ at the boundaries is one of 1, 5, or 10 [K/min]. . . . .	70
7.3	(a) A contour plot of specific heat at constant pressure, $c_p$ . The color scale is adjusted to the range of values observed within the particles; the actual minimum $c_p$ observed is $1464 [\text{J}/(\text{kg}\cdot\text{K})]$ , the reference value for the matrix. (b) A contour plot of specific heat at constant volume, $c_v$ . Again, the color scale is adjusted to the range of values observed within the particles; in this case, the actual maximum $c_v$ observed is $1458 [\text{J}/(\text{kg}\cdot\text{K})]$ , the reference value for the matrix. Both plots are at the point in the simulation where the boundary temperature, $\theta_\Gamma$ , approximately equals the transition temperature, $\theta_T$ . . . . .	72

7.4	(a) A contour plot of equivalent plastic strain, $\varepsilon_p$ , at the end of the simulation where the boundary temperature is approximately 550 [K]. Compare the shear bands above to the crack profiles in Fig. 5 of reference [100]. (b) A plot of the percent change of the sample volume as a function of boundary temperature. Here, $\Delta V_r/V_{0,r}$ refers to the change in volume of region $r$ with respect to initial region volume $V_{0,r}$ . Compare to the dimensional change of the first heating cycle in Fig. 2 [96]. . . . .	74
7.5	(a) A contour plot of the pressure experienced by the representative sample at the point in the simulation where the boundary temperature, $\theta_\Gamma$ , approximately equals the transition temperature, $\theta_T$ . (b) A plot of the axial Cauchy stress components for the representative cell showing virtually isotropic response. . . . .	76
7.6	Overall (a) chemical, (b) elastic, and (c) plastic heating rates in the composite sample for the 5 [K/min] boundary heating rate. . . . .	78
7.7	Overall composite Cauchy stress magnitude $\sigma \equiv \sqrt{\sigma : \sigma}$ . The shaded regions indicate $\pm 1$ standard deviation from the mean for five realizations. . . . .	79
7.8	Average chemical heating rate (a) and temperature rate (b) in the domain for the 40%, 50%, and 60% volume fractions at the 5 [K/min] boundary heating rate. The shaded regions indicating $\pm 1$ standard deviation from the mean for five realizations are omitted since standard deviations less than 0.8 [W/kg] for the chemical heating rate and coefficients of variation less than 0.5% for the temperature rate are observed. The coefficient of variation cannot be used for the chemical heating rate since the means reach values near zero before and after the transition regime. . . . .	80
7.9	Overall composite specific heat at constant pressure (a) and constant volume (b) for a boundary heating rate of 5 [K/min]. The shaded regions indicating $\pm 1$ standard deviation from the mean from five realizations are omitted since coefficients of variation less than 0.8% for $c_p$ and less than 0.14% for $c_v$ are observed. . . . .	81
7.10	Overall total heating rates for the different boundary heating conditions. The shaded regions indicating $\pm 1$ standard deviation from the mean from five realizations are omitted since standard deviations of less than 2.8 [W/kg] are observed. The coefficient of variation cannot be used since the means reach values close to zero before and after the transition regime. . . . .	82

7.11	Chemical heating rate in the particles (a) and critical temperature for the chemical heating rate as a function of boundary heating rate (b). The shaded regions indicating $\pm 1$ standard deviation from the mean from five realizations are omitted since standard deviations of less than 6 [W/kg] are observed. The coefficient of variation cannot be used since the means reach values close to zero before and after the transition regime. . . . .	83
B.1	Plots of (a) $y_\delta$ and (b) $\theta$ under spatially homogeneous, adiabatic conditions. Both plots employ a log scale for the $t$ axis in order to highlight the dynamics. . . . .	98

## TABLES

5.1	Calibrated parameters for the CTE model in Eq. 5.3. . . . .	54
5.2	Calibrated parameters for the bulk modulus model in Eq. 5.6. . . . .	54
5.3	Summary of material properties used for the PBX simulations. . . . .	55

## SYMBOLS AND ABBREVIATIONS

CTM	Chemo-thermo-mechanical
HMX	Energetic crystal, octahydro-1,3,5,7-tetranitro-1,3,5,7-tetrazocine
PBX	Plastic bonded explosive
PCM	Phase change material
DSC	Differential scanning calorimetry
CTE	Coefficient of thermal expansion
$\mathcal{O}(10^\bullet)$	On the order of $10^\bullet$
$\Omega_0, \Omega$	Reference, current configuration of a body
$\mathbb{R}$	Set of all real numbers
$\theta$	Temperature
$\theta_\Gamma$	Boundary temperature
$\dot{\theta}_\Gamma$	Boundary temperature rate
$\theta_c$	Critical temperature for chemical heating
$\phi$	Motion of a body
${}^0\vec{x}, \vec{x}$	Position of a particle in reference, current configuration
$\vec{u}$	Displacement vector
$t$	Time
${}^0\Gamma, \Gamma$	Boundary of a body in reference, current configuration
${}^0\vec{n}, \vec{n}$	Unit outward normal vector in reference, current configuration
$\emptyset$	Empty set
$\mathbf{F}$	Total deformation gradient
$\mathbf{F}_e$	elastic deformation gradient

$\mathbf{F}_\theta$	thermal deformation gradient
$\mathbf{F}_p$	plastic deformation gradient
$\mathcal{N}_0, \mathcal{N}$	Neighborhood in reference, current configuration
$\vartheta$	Thermal stretch ratio
$\alpha$	Coefficient of thermal expansion (CTE)
$\mathbf{b}_e$	elastic left Cauchy-Green tensor
$\mathbf{C}$	total right Cauchy-Green tensor
$\mathbf{C}_p$	plastic right Cauchy-Green tensor
$\rho_0, \rho$	Mass density in reference, current configuration
$J$	Determinant of $\mathbf{F}$
$J_e$	Determinant of $\mathbf{F}_e$
$J_\theta$	Determinant of $\mathbf{F}_\theta$
$J_p$	Determinant of $\mathbf{F}_p$
$e$	Internal energy per unit mass
$R$	Energy source per unit mass
$\boldsymbol{\sigma}$	Cauchy (true) stress
$p$	Pressure
${}^0\vec{\mathbf{q}}, \vec{\mathbf{q}}$	Heat source vector in reference, current configuration
${}^0\boldsymbol{\Lambda}, \boldsymbol{\Lambda}$	Thermal conductivity tensor in reference, current configuration
$c_p$	Specific heat at constant elastic strains (i.e., constant pressure)
$c_v$	Specific heat at constant deformation (i.e., constant volume)
$q_c$	Chemical heating per unit mass
$q_e$	Elastic heating per unit mass
$q_p$	Plastic heating per unit mass
$N_s$	Number of chemical species
$N_r$	Number of chemical reactions
$y_n$	Mass fraction of the $n$ -th chemical species

$M_n$	Molar mass of the $n$ -th chemical species
$\nu_{nm}$	Stoichiometric coefficient difference for species $n$ , reaction $m$
$\nu'_{nm}$	Reactant stoichiometric coefficient for species $n$ , reaction $m$
$\nu''_{nm}$	Product stoichiometric coefficient for species $n$ , reaction $m$
$r_{c,m}$	Rate of reaction of the $m$ -th reaction
$\vec{\mathbf{f}}_0, \vec{\mathbf{f}}$	Body force per unit mass in reference, current configuration
${}^0\vec{\mathbf{t}}, \vec{\mathbf{t}}$	Traction vector in reference, current configuration
$\varphi$	Helmholtz free energy
$\varphi_c$	Chemical portion of the Helmholtz free energy
$\varphi_\theta$	Thermal portion of the Helmholtz free energy
$\varphi_e$	Elastic portion of the Helmholtz free energy
$\varphi_p$	Plastic portion of the Helmholtz free energy
$\vec{\mathbf{X}}_p$	Vector of state variables governing plastic deformation
$\chi_n$	Chemical potential per mole of $n$ -th chemical species
$A_m$	Pre-exponential factor for the $m$ -th reaction
$E_{a,m}$	Activation energy for the $m$ -th reaction
$R_u$	Universal gas constant
$\hat{A}_m$	Corrective factor for the $m$ -th reaction
$\kappa$	Bulk modulus
$\mu$	Shear modulus
$\nu$	Poisson ratio
$f_p$	Plastic yield function
$\sigma_0$	Yield stress
$H$	Isotropic plastic hardening modulus
$f_{\text{TQ}}$	Taylor-Quinney factor
$\varepsilon_p$	Plastic hardening variable
$\boldsymbol{\tau}_e$	'Elastic' Kirchhoff stress

$\eta$	Entropy per unit mass
$\mathbf{l}$	Spatial (Eulerian) velocity gradient
$\mathbf{d}$	Symmetric part of $\mathbf{l}$
$\mathbf{l}_e$	Elastic spatial velocity gradient
$\mathbf{d}_e$	Symmetric part of $\mathbf{l}_e$
$\frac{\partial y}{\partial x} \Big _z$	Partial derivative of $y$ with respect to $x$ , holding $z$ fixed
$\ \bullet\ $	Frobenius norm of tensor $\bullet$
$[\bullet]^{\text{sym}}$	Symmetric part of tensor $\bullet$
$\text{DEV}[\bullet], \text{dev}[\bullet]$	Deviatoric part of tensor $\bullet$ in reference, current configuration
$\text{TR}(\bullet), \text{tr}(\bullet)$	Trace of tensor $\bullet$ in reference, current configuration
$\mathcal{D}_c$	Chemical dissipation
$\mathcal{D}_\theta$	Thermal dissipation
$\mathcal{D}_p$	Plastic dissipation
$\ell$	Spatial latent heat tensor at constant total strains
$\ell_e$	Spatial latent heat tensor at constant elastic strains
$\mathbf{T} : \mathbf{S}$	Full contraction of tensors $\mathbf{T}$ and $\mathbf{S}$ (i.e., $\mathbf{T}_{ij} \mathbf{S}_{ij}$ )
$\mathcal{L}_p$	Plastic Lagrange functional
$\mathbf{n}, \mathbf{N}$	Yield surface normal in reference, current configuration
$\dot{\lambda}_p$	Plastic consistency variable (i.e., plastic Lagrange multiplier)
$\widehat{(\bullet)}$	Volume preserving component of strain tensor $\bullet$
$\mathcal{L}_v(\bullet)$	Lie derivative of $\bullet$
$\gamma$	Mechanical volume
$H^k$	Sobolev space
$\vec{\mathbf{y}}$	Vector of chemical species mass fractions
$\vec{\mathbf{M}}$	Vector of molar masses
$\nu$	Matrix of stoichiometric coefficients
$\vec{\mathbf{r}}_c$	Vector of rates of reaction

$\Delta h^{\text{rxn}}$	Heat of reaction per unit mass
$\Delta e^{\text{rxn}}$	Reaction change in internal energy per unit mass
$\alpha_0$	Nonlinear CTE initial magnitude
$\alpha_1$	Nonlinear CTE magnitude parameter
$\omega$	Nonlinear CTE shape parameter
$\theta_T$	Nonlinear CTE transition temperature
$\kappa_0$	Nonlinear bulk modulus initial value
$\kappa'_0$	Nonlinear bulk modulus initial slope
$\kappa_1$	Nonlinear bulk modulus minimum value
$\phi_0$	Nonlinear bulk modulus phase parameter
$\phi_1$	Nonlinear bulk modulus phase parameter
$W$	W Lambert function
$\varepsilon$	Engineering uniaxial strain
$\langle \bullet \rangle_r^n$	Volumetric average of $\bullet$ for domain $r$ in the $n$ -th realization
$\widehat{\langle \bullet \rangle}_r$	Ensemble average of $\bullet$ over all realizations for domain $r$
$\Omega_{0,r}^n$	Domain volume for domain $r$ and realization $n$
$\mathcal{R}_\bullet$	Newton-Raphson residual for field $\bullet$
$\mathcal{K}_{\bullet\circ}$	Newton-Raphson tangent for field $\bullet$ with respect to field $\circ$
$V$	Lagrange functional for the conservation of linear momentum
$\Delta_{\text{rxn}}$	Reaction zone thickness

## ACKNOWLEDGMENTS

I owe so much to so many people that have been present in my pursuit of higher education. First and foremost, I would like to acknowledge my advisor, Karel Matouš, for all his teachings, guidance, and support. I would not be the scientist and engineer that I am today without your countless efforts to get me here.

I would like to thank my undergraduate advisor, Prof. Catherine Deibel, and Prof. Jeffrey Blackmon for providing the opportunity to experience research first-hand along with the countless others in the Louisiana State University Department of Physics, the Department of Mathematics, and LSU in general. I would like to thank Melissa Crawford, Prof. Isiah Warner, and all of LA-STEM for the guidance that I would have been completely lost without.

I, of course, thank the long list of people in AME and at the University of Notre Dame. David Go, Nancy O'Connor, Nancy Davis, Donna Fecher, and Carly Griffin, and really *countless* others have done so much to keep me going. Kathy Knoll and Gail Small, it goes without saying that I would have been lost a long time ago without your presence in CSWARM and the department.

I would also like to acknowledge my labmates for keeping me sane (at least partially) in those cubicles for so many years. Cale, Dewen, and Katherine, you were there for me from day one and I'm so lucky to be able to say that. Cody, Zach, Sion, and Jack you were such welcome additions to our group and it's been great getting to know you all. Sangmin, Mohammed, and Waad, where would I be without your answers to my endless questions?

Of course, I would like to extend my sincerest gratitude to my PhD Committee, both former and present. Dr. Bukač, Dr. Powers, Dr. Price, and Dr. Roberts, it has been and continues to be an honor to work with you.

Once I again, I owe so much to so many others. Even if you're not listed here, I'm forever grateful.

Finally, I would like to acknowledge support from the Department of Energy, National Nuclear Security Administration, under the reward No. DE-NA0002377 as part of the Predictive Science Academic Alliance Program II. I would also like to acknowledge support from Los Alamos National Laboratory under award No. 625808.

## CHAPTER 1

### INTRODUCTION

Heterogeneous materials with complex microstructures are ubiquitous in nature and engineering applications. Energetics (e.g., explosives, solid propellants) arm our militaries and fuel our spaceships. Biomaterials (e.g., cell tissue, solid biomass fuel) form the basis of organic life, and offer sustainable alternative energy sources. In engineering, heterogeneity can induce favorable material behavior when compared to that of a given material's constituents. In biology, heterogeneity in form is necessary for complexity in function. Understanding the physics of the material response of heterogeneous materials often proves crucial to their safe-handling and optimal usage. Successfully predicting the chemo-thermo-mechanical (CTM - i.e., the chemical, thermodynamic, and mechanical) responses of these materials often proves to be worthwhile.

The material response and material properties of heterogeneous systems can be measured experimentally, and predictions can be made based on observation. Prediction can also, however, be done using computational simulations. Such simulations that account for geometry, constituent material properties, internal and external conditions, etc. dramatically reduce the need for extensive experimentation. Models can be calibrated using appropriate experiments, then scientific software can be re-run in any number of configurations and settings to predict material responses without the need to run experiments repeatedly. This saves time and money, and improves efficiency and overall optimality by reducing the usage of expensive, delicate, unsafe, etc. specimens. These capabilities associated with a computational framework that

can model the CTM response of heterogeneous materials make its development a worthwhile contribution to engineering and science.

### 1.1 Motivation for the Modeling of Single Crystal HMX Phase Transition

Understanding the chemo-thermo-mechanical (CTM) processes of materials has long been a focus of scientific endeavor. The highly complex interactions between chemical reactions, energy transfer, deformation, visco-plastic flow, etc. within and between material systems are inherently difficult to describe or predict. However, efforts to do so often prove to be beneficial and even transformative. Phase transition is an example of a CTM process that is common in biology [65], material science [46], manufacturing [12, 53, 60], and many other systems and applications [24, 89]. Phase transition often occurs in systems which are not in thermodynamic equilibrium and can lead to exotic material behavior. For example, experiments have shown large changes in specific heat values. Differential scanning calorimetry (DSC) measurements of several phase change materials have shown order of magnitude variations (i.e., between  $\mathcal{O}(10^3)$  and  $\mathcal{O}(10^4)$  [J/(kg·K)]). Lamberg et al. [46] performed experiments on the phase change material (PCM) paraffin and measured such highly nonlinear specific heats. They proposed fitting functions to model this behavior and used them for numerical computations. Hunger et al. [39] presented a set of experiments on PCM based concretes which also produced such exotic specific heat behavior. They also concluded that increased PCM volume percentages led to increased heat capacity and, in turn, improved thermal performances for the concrete. Cao et al. [12] fabricated geopolymer concretes containing microencapsulated PCMs in order to take advantage of this tendency of PCMs to produce high thermal energy storage capacities within heterogeneous materials. They also developed and validated a numerical fit for the specific heat capacity. Experimental results once again showed highly unfamiliar behavior in the specific heat. Cao et al. [13] further

utilized these results in the study of the construction of single house dwellings with multilayer walls containing PCMs. This work posits the plausibility of exotic specific heat behavior in phase transitioning systems beyond those aforementioned since similar nonlinear, non-equilibrium processes have often been observed. For example, Baldo and Santos [6] performed experiments on silicon dioxide ( $\text{SiO}_2$ ) quartz undergoing solid phase transition. These experiments revealed highly nonlinear coefficient of specific heat behavior (i.e., large spikes in volume) within the phase transition regime. Selbach et al. [71] used high-temperature X-ray diffraction to study bismuth ferrite ( $\text{BiFeO}_3$ , also known as BFO) undergoing phase transition. Similar highly nonlinear dimensional changes were observed. Ran et al. [68] performed measurements on single crystal  $\text{URu}_{2-x}\text{Fe}_x\text{Si}_2$  undergoing phase transition. Their results included data showing exceptionally complex specific heat and coefficient of thermal expansion behavior.

One class of material systems where such non-equilibrium CTM processes are of an interest is energetic materials. Energetic materials (e.g., explosives, solid propellants) are used in many military and commercial applications. A detailed understanding of their behavior under thermal and mechanical loads is quintessential to ensure their safe handling, storage, and use. Due to their high sensitivity, even mild heat or pressure changes may cause microstructural transformations leading to permanent damage with subsequent formation of voids/pores and increase in the material surface area, and can eventually trigger unwanted detonation [100].

In particular, a great deal of previous studies on energetic materials deal with octahydro-1,3,5,7-tetranitro-1,3,5,7-tetrazocine (HMX) as it finds use in many different explosives and solid propellants. HMX phase transitions between four solid phase polymorphs labeled  $\alpha$ -,  $\beta$ -,  $\gamma$ -, and  $\delta$ -HMX [42]. At room temperature, the HMX molecule exists in the solid, stable  $\beta$  phase. When heated to approximately 435 [K], it undergoes a polymorphic transition to the less stable  $\delta$  phase [11, 35, 42, 92]. This

phase change is coupled with a large (6.7%) spike in volume [96].

## 1.2 Motivation for the Modeling of Phase Transition in HMX Based PBXs

Beyond the motivations for studying HMX discussed in Section 1.1, there are many incentives to studying these HMX based PBXs. Plastic bonded explosives (PBXs) are widely used in military and industrial applications due to their high energy output and excellent stability properties. PBXs consist of a high explosive, such as HMX, embedded in a polymer matrix. Despite the effectiveness of HMX-based PBXs, there is still a lack of understanding of their complex behavior and performance under different loading conditions.

Computational modeling provides a powerful tool to gain insight into the underlying physics of PBXs and can aid in the design of safer and more efficient explosives. The computational modeling of PBXs is a challenging task due to the multiscale nature of the problem, where the macroscopic behavior of the PBX is influenced by the microscopic properties of the HMX crystals and the polymer matrix.

As such, it is useful to develop a comprehensive computational model for HMX-based PBXs that can accurately predict their behavior under different loading conditions. The development of a robust computational model for HMX-based PBXs will have significant implications in the design and optimization of new PBX formulations. The model can aid in the identification of critical design parameters that can enhance the safety and performance of PBXs. Moreover, the model can provide insights into the pre-ignition response of PBXs.

In addition, the aforementioned spike in the sample volume which accompanies HMX  $\beta \rightarrow \delta$  phase transition can often lead to partial or total de-bonding of the HMX particles from the surrounding matrix. Experiments show that the thermal cracks, indeed, occur around large crystals [31, 66].

## 1.3 Literature Review

### 1.3.1 Chemo-thermo-mechanical Modeling

Coupled thermo-mechanical models and solvers have existed for quite some time. Čanadija and Brnić [94] developed a model based on associative coupled thermo-plasticity at finite strains with the added novelty of temperature-dependent material parameters. Chen et al. [14] proposed and developed a thermo-elasto-plasticity constitutive model to describe the behavior of metal crystals at finite temperature. Similarly, coupled thermo-chemical solvers have been put into extensive use for over 50 years [99]. In this regard, the literature on reactive liquids and gases is extensive and well developed. The modeling of combustion flow chemistry, laminar flames, etc. has been thoroughly studied and developed over the years, while advances in computational fluid dynamics (CFD) have produced a great number of implementations of said models with great predictive capabilities. Fedkiw et al. [26] developed a framework to solve the compressible Navier-Stokes equations extended to model multi-species chemically reactive gas flow and used finite difference spatial discretization and Runge-Kutta time integration to implement the framework computationally. Powers and Paolucci [63] developed a method for estimating reaction zone thicknesses in gas-phase detonations with detailed kinetics and performed numerical simulations based on the method using various integration schemes and adaptive spatial discretizations in one dimension. Kee et al. [43] developed a solver using the finite difference and Newton's methods to model species and temperature profiles in burner-stabilized and propagating premixed laminar flames while accounting for finite rate chemical kinetics and multicomponent molecular transport. Literature on continuum models of reactive solids, however, is sparse. Frank-Kamenetskii [28] laid the foundation for solid combustion by developing explosion theory based on a balance between chemical reaction and diffusion processes as found in solids. (orig-

inally published in 1955). Since then, traditional modeling efforts have reduced the three-dimensional combustion problem into a one-dimensional model. Such models neglect three-dimensional effects due to material morphology, gas-phase diffusion flames, and other factors [99]. In the past 10 years, Alawieh et al. [2] combined results from molecular dynamics simulations with mixture theory to characterize intermixing rates during different reaction regimes in Ni/Al nanolaminates. Nikbakht and Assadi [61] developed a phase field model to simulate the high-temperature synthesis of intermetallic compounds. Xiao et al. [103] used molecular dynamics simulations to study the mechanical and kinetic properties of  $\beta$ -HMX and  $\beta$ -HMX based polymers.

Jackson and Buckmaster [40] developed one of the most complete numerical frameworks for computational solid combustion which permits the exploration of detailed scientific issues in the combustion of heterogeneous propellants. The framework allows for the modeling of propellant morphology, subscale homogenization, and coupling between the gas and solid phases. The model is quite thorough in that it, in addition to the propellant combustion, the dynamics of the inert rocket case and the joints between case sections, flow through the exit nozzle, surface regression of the propellant as the propellant burns are all simulated in the fully 3D model. [40].

Fully coupled CTM solvers have made great progress in recent years. Davison et al. [18] developed a model and implementation for coupled thermal, hydrological, mechanical, chemical simulations of heterogeneous geosystems utilizing massively parallel processing. The model allows transport of species in multiple phases where transfer between phases and of chemical reactions is specified by phenomenological source terms. It also supports large deformation quasi-static mechanics and a constitutive model that incorporate the influence of liquid saturation and suction on the isothermal elasto-plastic response of porous materials, as well as a separate constitutive model that models creep behavior in two dimensions. It is worthwhile to note that, in 3D, they found the simulations were too time consuming and that it

was frequently difficult to obtain convergence of the equilibrium equations. Yoh and Kim [104] developed a computational framework for studying shock compression of energetic materials based on a small strain formulation. They modeled the reacting flows of high energy explosive materials which generate shock waves and high strain rate deformation of metallic confinements at high pressures and temperatures. Still, there is a great deal of progress to me made on continuum scale fully coupled CTM models and solvers, in particular those which involve reactive heterogeneous solids.

In this light, the development of a thermodynamically consistent, fully coupled, three dimensional, finite strain CTM model of continua to be applied to solid systems serves to make meaningful and novel contributions to computational engineering.

### 1.3.2 Single Crystal HMX

Much effort has been directed towards understanding the chemical behavior of HMX. Smilowitz et al. [83] performed second harmonic generation (SHG) experiments to characterize the transformation kinetics of the  $\beta \rightarrow \delta$  solid state transition of HMX. Weese et al. [97] reported results from differential scanning calorimetry (DSC) experiments and measured the kinetics of the  $\beta \rightarrow \delta$  phase transformation of HMX. Wemhoff and Burnham [98] and ASM [4] used ALE3D to model the kinetics of the  $\beta \rightarrow \delta$  solid-solid phase transformation of HMX. Studies have also been performed to quantify the thermomechanical behavior of HMX. Li et al. [52] used the nanoindentation technique to determine the elastic modulus of the  $\beta$  phase of HMX; the loading-unloading curves presented therein indicate the presence of residual strains in the crystals created by permanent plastic deformations. Weese and Burnham [96] performed thermo-mechanical analysis (TMA) to characterize the coefficient of thermal expansion (CTE) of the  $\beta$  and  $\delta$  polymorphs of HMX. It was found that the CTE is constant until about 440 [K] (the temperature near which the  $\beta \rightarrow \delta$  phase transition starts) and after about 500 [K] (the temperature near which

the  $\beta \rightarrow \delta$  phase transition ends). During the phase transition, from 440 - 500 [K], the CTE experiences a sharp spike which causes a rapid change in the dimensions of the sample.

A great effort has also been directed towards modeling the CTM behavior of energetic materials like HMX through the heating (pre-ignition), ignition, and explosive phases. An experimental effort has been directed towards understanding the chemical [83, 97, 98] and thermomechanical [96] behavior of HMX. A substantial amount of work has also been done on the modeling and simulation of HMX. Yoh and McClelland [105] used ALE3D to calculate temperature fields, the time to explosion, and strain of the vessel wall during scaled thermal explosion experiments. Yoh and Kim [104] developed a computational framework for studying shock compression of energetic materials based on a small strain formulation. McGlaun et al. [57] developed an Eulerian finite volume shock physics code (CTH) which modelled elastic-plastic behavior and high explosive reactions. Baer [5] used CTH to investigate reaction and shock wave structures in a mixture of HMX crystals and binder. Springer et al. [84] performed non-reactive and reactive ALE3D simulations to investigate hot spots in HMX in the absence of thermal diffusion, convection, and radiation. Hu et al. [38] developed a mesoscale phase transition model to investigate the effects of the  $\beta \rightarrow \delta$  phase transition on the thermomechanical behavior of single HMX crystals using ABAQUS.

### 1.3.3 HMX Based PBXs

A great effort has also been directed towards modeling the CTM behavior of energetic materials like PBX through the heating (pre-ignition), ignition, and explosive phases. Funk et al. [29] measured the stress-strain behavior of PBX-9501 (95% HMX, 2.5% BDNPA-F, 2.5% Estane) at varying strain rates and at different temperatures. They found that the compressive strength of PBX-9501 falls with increasing temper-

ature and rises with increasing strain rate. Glascoe et al. [31] studied the damage response of PBXN-9 (92% HMX, 2% HYTEMP, 6% DOA) subjected to thermal insults. They used DSC measurements and thermogravimetric analysis (TGA) to characterize the decomposition kinetics and study thermally induced damage in samples. Barua and Zhou [7] developed a cohesive finite element method framework to study the response of HMX based PBXs at the microstructural level. They studied large deformation, thermomechanical coupling, failure, and frictional heating. Shang et al. [74] used the material point method within the Uintah Computational Framework [10, 20, 32, 59] to model the shock response of PBX-9501. They showed that, under shock loading, a great degree of plastic strain developed on the boundary of HMX grains. Shi et al. [75] used molecular dynamics simulations to research the effects of molar ratio within mixture systems consisting of  $\alpha$ -,  $\gamma$ -, and  $\delta$ -HMX molecules coexisting with  $\beta$ -HMX crystals. They investigated the thermal stability, sensitivity, and mechanical properties of these explosives.

#### 1.4 Novelty of this Dissertation

As described in the previous sections of this chapter, advancements have been made in the modeling and simulation of heterogeneous reactive materials. However, there are still many areas that have yet to be fully investigated. The primary goal of this dissertation is to develop thermodynamically consistent chemo-thermo-mechanical model and computational framework for the analysis of these materials. The contributions of this work to the scientific community are described as follows.

#### **Contribution to the Continuum Formulation**

This dissertation provides a concise presentation of the governing partial differential equations and balance laws necessary to model the desired systems, derived

in a thermodynamic context with respect of the Second Law (of Thermodynamics). These equations are given in both the Eulerian and Lagrangian settings with explicit transformations provided when necessary. Novel, theoretically derived continuum equations for the specific heats at constant elastic strains (i.e., constant pressure,  $c_p$ ) and at constant deformation (i.e., constant volume,  $c_v$ ) are also presented. Furthermore, a novel, theoretically derived equation which predicts the critical temperature at which maximum heat release or consumption occurs for Arrhenius type kinetics is provided. Finally, novel, nonlinear, temperature dependent models for the coefficient of thermal expansion and bulk modulus of material systems undergoing solid-solid phase transition are introduced.

### **Contribution to Computational Modeling**

This dissertation also provides algorithms for discretization and implementation needed to solve the governing equations numerically for the fields of interest. Coupling algorithms and strategies for multiphysics, specifically CTM, phenomena are few and far between. This is due to the scarcity of background literature as previously described, as well as the well known difficulties with computational cost and efficiency associated with solving engineering scale problems. This work focuses on the development and implementation of such algorithms using the finite element method. Two (2) computational modeling manuscripts detailing this work have been submitted for publication. Williams and Matouš [101] detail the  $\beta \rightarrow \delta$  phase transition of single crystal HMX considering reaction phenomena, nonlinear thermal expansion, and nonlinear elastic parameters. Williams et al. [102] extend the work of [101] by investigating HMX based energetic materials with the addition of plasticity and microstructure considerations.

## Contribution to Physical Understanding

This dissertation further provides, in great detail, the results of investigating the multiphysics associated with solid-solid phase transformations. Specifically, detailed simulation results for single crystal HMX as well as HMX based plastic bonded explosives are provided with accompanying analysis. These results yield insight into the intricate relationships between evolving material properties, microstructural geometry, and CTM response to thermo-mechanical stimuli. Specifically, this work contributes ideas on the physics of the evolution of the specific heats, elastic moduli, and coefficient of thermal expansion of materials undergoing phase transition. It also contributes physical understanding of the effect of microstructure on the behavior of plastic bonded explosives. Finally, it contributes physical understanding of the material response of energetic materials experiencing various heating rates and mechanical loading conditions.

### 1.5 Dissertation Overview

The remainder of this dissertation is organized as follows. Chapter 2 provides the general equations of the chemo-thermo-mechanical model of phase change materials, including the governing equations, constitutive equations, and thermodynamics. Chapter 3 specifies the model as it pertains to the material systems and simulations conducted in this work. Chapter 4 provides details on the numerical implementation of the model including descriptions of spatial discretization techniques, temporal discretization techniques, and solution staggering techniques. Chapter 5 details the calibration of the model. Chapter 6 provides results of the computational modeling of the  $\beta \rightarrow \delta$  phase transition of single crystal HMX. Chapter 7 provides results of the computational modeling of HMX based plastic bonded explosives. Chapter 8 concludes the dissertation by summarizing the work presented and outlining possible

directions for future research. Appendix [A](#) provides additional details pertaining to the Lagrangian representation of the model. Appendix [B](#) provides an analysis of the chemo-thermal model under the special case of adiabatic, spatially homogeneous dynamics.

## CHAPTER 2

### CHEMO-THERMO-MECHANICAL MODEL OF PHASE CHANGE MATERIALS

#### 2.1 Governing Equations

In this section, we present a formulation for the coupled chemo-thermo-mechanical (CTM) framework. Let  $\Omega_0 \subset \mathbb{R}^3$  denote the reference configuration of a given body at a uniform reference temperature  $\theta_0$  that undergoes a motion  $\phi({}^0\vec{\mathbf{x}}, t)$ , where  ${}^0\vec{\mathbf{x}} \in \Omega_0$  designates the position of a particle in the reference configuration and  $t \in \mathbb{R}^+$  denotes time (Figure 2.1). The boundary of the body in the reference configuration,  ${}^0\Gamma$ , is partitioned by the Dirichlet ( ${}^0\Gamma_{\vec{\mathbf{u}}}$  for displacement,  ${}^0\Gamma_{\theta}$  for temperature) and Neumann ( ${}^0\Gamma_{\vec{\mathbf{t}}}$  for traction,  ${}^0\Gamma_{\vec{\mathbf{q}}}$  for heat flux) boundaries. Explicitly,  ${}^0\Gamma = {}^0\Gamma_{\vec{\mathbf{u}}} \cup {}^0\Gamma_{\vec{\mathbf{t}}}$  while  ${}^0\Gamma_{\vec{\mathbf{u}}} \cap {}^0\Gamma_{\vec{\mathbf{t}}} = \emptyset$  and  ${}^0\Gamma = {}^0\Gamma_{\theta} \cup {}^0\Gamma_{\vec{\mathbf{q}}}$  while  ${}^0\Gamma_{\theta} \cap {}^0\Gamma_{\vec{\mathbf{q}}} = \emptyset$ . The unit outward normal vector in the reference configuration is denoted  ${}^0\vec{\mathbf{n}}$ . The associated symbols in the current configuration are denoted without the preceding superscript 0 ( $\Gamma$ ,  $\vec{\mathbf{n}}$ , etc.). The motion, accompanied with changes in the energy and the chemical composition of the body, transforms the body to its current configuration denoted by  $\Omega \subset \mathbb{R}^3$ . The current position of the material point is  $\vec{\mathbf{x}}(t) = \phi({}^0\vec{\mathbf{x}}, t)$ , such that  $\vec{\mathbf{x}} = {}^0\vec{\mathbf{x}} + \vec{\mathbf{u}}({}^0\vec{\mathbf{x}}, t)$ , where  $\vec{\mathbf{u}}$  is the displacement vector. We introduce  $\mathbf{F}({}^0\vec{\mathbf{x}}, t) = {}^0\nabla\phi({}^0\vec{\mathbf{x}}, t)$  as the deformation gradient. Here,  ${}^0\nabla$  is the gradient with respect to  ${}^0\vec{\mathbf{x}}$  and  $\mathbf{1}$  is the second-order identity tensor.

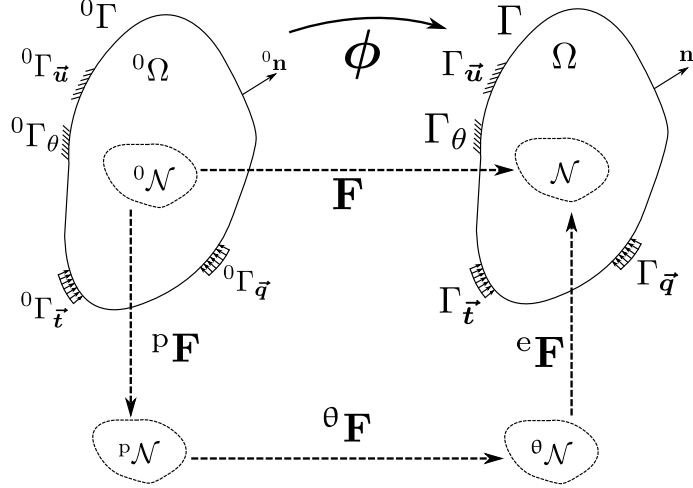


Figure 2.1. Kinematics of the framework.

Next, we consider local stress free states in the neighborhood  $\mathcal{N}_0$  and define a multiplicative decomposition of the total deformation gradient  $\mathbf{F}$  into plastic ( $\mathbf{F}_p$ ), thermal ( $\mathbf{F}_\theta$ ) and elastic ( $\mathbf{F}_e$ ) parts given by [49, 58, 87]

$$\mathbf{F} = \mathbf{F}_e \mathbf{F}_\theta \mathbf{F}_p. \quad (2.1)$$

Throughout this work, tensors adjacent in this manner indicates standard matrix multiplication unless otherwise noted. The plastic deformation gradient,  $\mathbf{F}_p$ , defined in the same sense as the elasto-plastic decomposition from Lee [49], yields an isothermal plastically deformed and relaxed configuration denoted by  $\mathcal{N}_p$ . The thermal deformation gradient,  $\mathbf{F}_\theta$ , allows the free thermal expansion and contraction of  $\mathcal{N}_p$  to obtain the second intermediate stress free state designated by  $\mathcal{N}_\theta$ [37, 95].  $\mathbf{F}_e$  is the isothermal, stress-producing elastic deformation gradient.

It is well known that the intermediate configurations  $\mathcal{N}_p$  and  $\mathcal{N}_\theta$  are unique only

up to a rigid body rotation [49]. In order to remedy this situation, we specify an isotropic thermal deformation gradient given by

$$\mathbf{F}_\theta = \vartheta(\theta)\mathbf{1}, \quad (2.2)$$

where  $\vartheta(\theta)$  represents the stretch ratio in any material direction. The thermal stretch ratio  $\vartheta$  is a function of the coefficient of thermal expansion (CTE) and is defined as

$$\vartheta(\theta) = \exp\left[\int_{\theta_0}^{\theta} \alpha(\tilde{\theta}) \, d\tilde{\theta}\right], \quad (2.3)$$

where  $\theta$  is the current temperature and  $\alpha(\theta)$  is the temperature-dependent CTE. Note that if the CTE is constant, then  $\vartheta(\theta) = \exp[\alpha(\theta - \theta_0)]$ . To uniquely define  $\mathbf{F}_p$ , we assume that the plastic deformations are purely distortional in nature and do not cause any rigid-body rotation [77]. It is also convenient to define the elastic left Cauchy-Green tensor  $\mathbf{b}_e \equiv \mathbf{F}_e \mathbf{F}_e^\top$  which, for isotropic thermal deformation, can be expressed as

$$\mathbf{b}_e = \vartheta^{-2} \mathbf{F} \mathbf{C}_p^{-1} \mathbf{F}^\top, \quad (2.4)$$

where the plastic right Cauchy-Green tensor is defined as  $\mathbf{C}_p \equiv \mathbf{F}_p^\top \mathbf{F}_p$ .

From here, we describe the governing equations of the CTM model. Let  $\rho_0({}^0\vec{\mathbf{x}})$  and  $\rho(\vec{\mathbf{x}}, t)$  be the mass densities in the reference and current configurations, respectively. The conservation of mass in the material description reads

$$\rho_0 = J\rho \quad \text{in } \Omega_0 \times \mathbb{R}^+, \quad (2.5)$$

where  $J({}^0\vec{\mathbf{x}}, t)$  is the determinant of  $\mathbf{F}$ . The conservation of energy is given as

$$\rho \dot{e} = \boldsymbol{\sigma} : \mathbf{l} - \nabla \cdot \vec{\mathbf{q}} + \rho r \quad \text{in } \Omega \times \mathbb{R}^+, \quad (2.6)$$

where  $e$  and  $r$  are the internal energy and the energy source per unit mass,  $\boldsymbol{\sigma}$  is the Cauchy (true) stress, and  $(\dot{\bullet})$  indicates the material time derivative of quantity  $(\bullet)$ , i.e., the time derivative at fixed material point. The heat conduction,  $\vec{\mathbf{q}}$ , is assumed to follow Fourier's model as

$$\vec{\mathbf{q}} = -\mathbf{\Lambda} \nabla \theta, \quad (2.7)$$

where  $\mathbf{\Lambda}$  is the second-order spatial thermal conductivity tensor.

In Section 2.3, we show that the conservation of energy can be expressed in terms of temperature as

$$\rho c_p \dot{\theta} + \nabla \cdot \vec{\mathbf{q}} = \rho (r + q_c + q_e + q_p) \quad \text{in } \Omega \times \mathbb{R}^+, \quad (2.8a)$$

$$\theta(\vec{\mathbf{x}}, t) = \tilde{\theta}(\vec{\mathbf{x}}, t) \quad \text{on } \Gamma_\theta \times \mathbb{R}^+, \quad (2.8b)$$

$$\vec{\mathbf{q}} \cdot \vec{\mathbf{n}} = \tilde{q}(\vec{\mathbf{x}}, t) \quad \text{on } \Gamma_{\vec{\mathbf{q}}} \times \mathbb{R}^+, \quad (2.8c)$$

$$\theta(\vec{\mathbf{x}}, t = 0) = \theta_0 \quad \text{in } \Omega, \quad (2.8d)$$

where  $c_p$  is the specific heat at constant pressure, and  $q_c$ ,  $q_e$ , and  $q_p$  are the chemical, elastic, and plastic heating terms per unit mass, respectively. Here,  $\tilde{\theta}$  and  $\tilde{q}$  are the prescribed temperature and heat flux on the boundary.

Neglecting mass diffusion, since the length scales involved in the continuum model developed herein are much larger than the atomic scale, the conservation of  $N_s$  chemical species in  $N_r$  reactions takes the form

$$\rho \dot{y}_n = \sum_{m=1}^{N_r} M_n \nu_{nm} r_{c,m} \quad \text{in } \Omega \times \mathbb{R}^+, \quad (2.9a)$$

$$y_n(\vec{\mathbf{x}}, t = 0) = y_{n,0} \quad \text{in } \Omega, \quad (2.9b)$$

where  $y_n$  and  $M_n$  are the mass fraction and molar mass of the  $n$ -th chemical species,  $\nu_{nm}$  is the stoichiometric coefficient difference (product minus reactant) for the  $n$ -th

chemical species in reaction  $m$ , and  $r_{c,m}$  is the rate of reaction of the  $m$ -th reaction for  $n = 1, 2, \dots, N_s$  and  $m = 1, 2, \dots, N_r$  [64].

Finally, the conservation of momenta assuming quasi-static motion are given as

$$\nabla \cdot \boldsymbol{\sigma} + \rho \vec{\mathbf{f}} = \vec{\mathbf{0}} \quad \text{in } \Omega, \quad (2.10a)$$

$$\boldsymbol{\sigma} = \boldsymbol{\sigma}^T \quad \text{in } \Omega, \quad (2.10b)$$

$$\vec{\mathbf{u}}(\vec{\mathbf{x}}) = \tilde{\vec{\mathbf{u}}}(\vec{\mathbf{x}}) \quad \text{on } \Gamma_{\vec{\mathbf{u}}}, \quad (2.10c)$$

$$\boldsymbol{\sigma} \cdot \vec{\mathbf{n}} = \vec{\mathbf{t}}(\vec{\mathbf{x}}) \quad \text{on } \Gamma_{\vec{\mathbf{t}}}, \quad (2.10d)$$

where  $\vec{\mathbf{f}}$  is the body force per unit mass and  $\vec{\mathbf{t}}$  is the traction vector. Here,  $\tilde{\vec{\mathbf{u}}}(\vec{\mathbf{x}})$  is the prescribed displacement of the boundary. We assume quasi-static motion since the mechanical wave time scales are much faster than those of the thermal cook-off problem.

## 2.2 Constitutive Equations

The Helmholtz free energy is assumed to follow an additive split given by

$$\varphi(\theta, y_n, \mathbf{b}_e, \vec{\boldsymbol{\chi}}_p) = \varphi_c(\theta, y_n) + \varphi_\theta(\theta) + \varphi_e(\mathbf{b}_e, \theta) + \varphi_p(\vec{\boldsymbol{\chi}}_p), \quad (2.11)$$

where  $\varphi_c$ ,  $\varphi_\theta$ ,  $\varphi_e$ , and  $\varphi_p$  are the chemical, thermal, elastic, and plastic parts of the Helmholtz energy per unit mass, respectively [95]. Here,  $\vec{\boldsymbol{\chi}}_p$  is the vector of state variables governing the plastic deformation. We take  $\varphi_c$  to be

$$\varphi_c(\theta, y_n) = \sum_{n=1}^{N_s} \frac{\chi_n(\theta)}{M_n} y_n, \quad (2.12)$$

where  $\chi_n$  is the chemical potential per mole of species  $n$  which is assumed to be, at most, linear in temperature. The rate of the  $m$ -th reaction,  $r_{c,m}$ , is defined using the

law of mass action, neglecting the reverse reaction, as [64]

$$r_{c,m} = k_{c,m} \prod_{n=1}^{N_s} \left( \frac{\rho y_n}{M_n} \right)^{\nu'_{nm}}, \quad (2.13)$$

where  $k_{c,m}$  is the rate constant and  $\nu'_{nm}$  is the forward (reactant) stoichiometric coefficient for the  $n$ -th species in reaction  $m$ . We model the reaction constant,  $k_c$ , using a modified Arrhenius law given by

$$k_{c,m} = A_m \widehat{A}_m(\dot{\theta}) \exp\left(-\frac{E_{a,m}}{R_u \theta}\right), \quad (2.14)$$

where  $A_m$  and  $E_{a,m}$  are the usual pre-exponential factor and activation energy of reaction  $m$ , respectively.  $R_u$  is the universal gas constant, and  $\widehat{A}_m$  is a corrective factor for reaction  $m$  which is assumed to depend on the heating rate  $\dot{\theta}$  [88, 98].

Inspired by linear theory [95], we take  $\varphi_\theta$  to satisfy the relation  $-\theta(\partial^2 \varphi_\theta / \partial \theta^2) = {}^0c_v + 9\alpha^2 \theta \kappa / \rho_0$  such that

$$\varphi_\theta(\theta) = {}^0c_v(\theta - \theta_0) - {}^0c_v \theta \log \left[ \frac{\theta}{\theta_0} \right] - \int_{\theta_0}^{\theta} \left[ \int_{\theta_0}^{\hat{\theta}} \frac{9\alpha^2(\hat{\theta})\kappa(\hat{\theta})}{\rho_0} d\hat{\theta} \right] d\tilde{\theta}, \quad (2.15)$$

where  $\kappa(\theta)$  is the temperature dependent bulk modulus and  ${}^0c_v$  is the initial state specific heat capacity at constant volume [37, 101].

Finally, we take  $\varphi_e$  to follow the relation given by [78, 85]

$$\rho_0 \varphi_e(\mathbf{b}_e, \theta) = J_p J_\theta (\widehat{W}_e + U_e), \quad (2.16a)$$

$$\widehat{W}_e(\mathbf{b}_e, \theta) = \frac{1}{2} \mu(\theta) [J_e^{-2/3} \text{tr}(\mathbf{b}_e) - 3], \quad (2.16b)$$

$$U_e(J_e, \theta) = \frac{1}{4} \kappa(\theta) [(J_e - 1)^2 + (\ln J_e)^2], \quad (2.16c)$$

where  $J_e$ ,  $J_\theta$ , and  $J_p$  are the determinants of  $\mathbf{F}_e$ ,  $\mathbf{F}_\theta$ , and  $\mathbf{F}_p$  respectively. Note also that  $J_e^2 = \det(\mathbf{b}_e)$ . Here,  $\mu(\theta)$  is the temperature dependent shear modulus.

Little is known on closed forms of the plastic part of the Helmholtz energy,  $\varphi_p$ , due to the nature of cold work as discussed in [69]. We consider rate independent, volume preserving ( $J_p \equiv \det(\mathbf{F}_p) = 1$ ) plastic response with isotropic linear hardening. The yield surface is characterized in the stress space using the classical von Mises-Huber criterion given by [41]

$$f_p(\boldsymbol{\tau}_e, \varepsilon_p) = \|\text{dev}[\boldsymbol{\tau}_e]\| - \sqrt{\frac{2}{3}}(\sigma_0 + H \varepsilon_p), \quad (2.17)$$

where  $\sigma_0$  and  $H$  are the yield stress and isotropic hardening modulus of the material, respectively. The deviator of a spatial tensor is given as  $\text{dev}[\bullet] = (\bullet) - \frac{1}{3}\text{tr}(\bullet)\mathbf{1}$ . The Frobenius norm of a tensor is given as  $\|\bullet\| = \sqrt{\bullet : \bullet}$ .  $\varepsilon_p$  is the plastic hardening variable which is analogous to the equivalent plastic strain, and  $\boldsymbol{\tau}_e$  is analogous to the Kirchhoff stress that can be obtained from the Cauchy stress as  $\boldsymbol{\tau}_e = \mathbf{J}_e \boldsymbol{\sigma}$ .

### 2.3 Thermodynamics

The internal energy is related to temperature through a Legendre transformation given by  $e = \varphi + \eta\theta$ , where  $\eta = \eta(\theta, y_n, \mathbf{b}_e, \vec{\boldsymbol{\chi}}_p)$  is entropy per unit mass. With this, the material time derivative of the internal energy is

$$\dot{e} = \dot{\varphi} + \dot{\eta}\theta + \eta\dot{\theta}. \quad (2.18)$$

It is easy to show from Eq. 2.1 that the spatial velocity gradient can be decomposed in terms of the rates of independent variables as

$$\mathbf{l} = \mathbf{l}_e + \mathbf{F} \left[ \mathbf{F}_p^{-1} \dot{\mathbf{F}}_p \right] \mathbf{F}^{-1} + \alpha \dot{\theta} \mathbf{1} = \mathbf{l}_e + \frac{1}{2} \mathbf{F}^{-\text{T}} \left[ \mathbf{C} \mathbf{C}_p^{-1} \dot{\mathbf{C}}_p \right] \mathbf{F}^{-1} + \alpha \dot{\theta} \mathbf{1}, \quad (2.19)$$

where  $\mathbf{l}_e = \dot{\mathbf{F}}_e \mathbf{F}_e^{-1}$  is regarded as the elastic spatial velocity gradient and  $\mathbf{C}$  is the total right Cauchy-Green tensor. Here, we have taken advantage of the fact that, for

isotropic plasticity,  $\mathbf{F}_p$  causes no rigid body rotation, i.e.,  $[\dot{\mathbf{F}}_p \mathbf{F}_p^{-1}]^{\text{sym}} = \dot{\mathbf{F}}_p \mathbf{F}_p^{-1}$  such that  $\dot{\mathbf{F}}_p = \mathbf{F}_p^{-\text{T}} \dot{\mathbf{C}}_p / 2$ . From Eq. 2.11, we use the chain rule to obtain

$$\dot{\varphi} = \frac{\partial \varphi}{\partial \theta} \dot{\theta} + \sum_{n=1}^{N_s} \frac{\partial \varphi}{\partial y_n} \dot{y}_n + \frac{\partial \varphi}{\partial \mathbf{b}_e} : \dot{\mathbf{b}}_e + \frac{\partial \varphi}{\partial \vec{\chi}_p} \cdot \dot{\vec{\chi}}_p. \quad (2.20)$$

Here, it is convenient to express  $\dot{\mathbf{b}}_e$  as

$$\dot{\mathbf{b}}_e = \mathbf{l}_e \mathbf{b}_e + \mathbf{b}_e \mathbf{l}_e^{\text{T}}, \quad (2.21)$$

such that

$$\frac{\partial \varphi}{\partial \mathbf{b}_e} : \dot{\mathbf{b}}_e = \frac{\partial \varphi}{\partial \mathbf{b}_e} : [\mathbf{l}_e \mathbf{b}_e] + \frac{\partial \varphi}{\partial \mathbf{b}_e} : [\mathbf{b}_e \mathbf{l}_e^{\text{T}}] = \left[ 2 \frac{\partial \varphi}{\partial \mathbf{b}_e} \mathbf{b}_e \right] : \mathbf{l}_e \quad (2.22)$$

where, due to the symmetry of  $\mathbf{b}_e$ , we obtain symmetric derivative,  $\partial \varphi / \partial \mathbf{b}_e$ , also. Note that we have *not* assumed commutativity of  $\partial \varphi / \partial \mathbf{b}_e$  and  $\mathbf{b}_e$ . Thus Eq. 2.20 can be recast as

$$\dot{\varphi} = \frac{\partial \varphi}{\partial \theta} \dot{\theta} + \sum_{n=1}^{N_s} \frac{\partial \varphi}{\partial y_n} \dot{y}_n + \left[ 2 \frac{\partial \varphi}{\partial \mathbf{b}_e} \mathbf{b}_e \right] : \mathbf{l}_e + \frac{\partial \varphi}{\partial \vec{\chi}_p} \cdot \dot{\vec{\chi}}_p. \quad (2.23)$$

In an entirely similar manner, we find that

$$\dot{\eta} = \frac{\partial \eta}{\partial \theta} \dot{\theta} + \sum_{n=1}^{N_s} \frac{\partial \eta}{\partial y_n} \dot{y}_n + \left[ 2 \frac{\partial \eta}{\partial \mathbf{b}_e} \mathbf{b}_e \right] : \mathbf{l}_e + \frac{\partial \eta}{\partial \vec{\chi}_p} \cdot \dot{\vec{\chi}}_p. \quad (2.24)$$

The second law of thermodynamics, in the form of the Clausius-Duhem [62, 93] inequality, reads

$$\boldsymbol{\sigma} : \mathbf{l} - \rho \dot{\varphi} - \rho \dot{\eta} - \frac{1}{\theta} \vec{\mathbf{q}} \cdot \nabla \theta \geq 0. \quad (2.25)$$

Substituting Eqs. 2.19 and 2.23 into Eq. 2.25 and rearranging gives

$$\begin{aligned} \left[ \boldsymbol{\sigma} - 2\rho \frac{\partial \varphi}{\partial \mathbf{b}_e} \mathbf{b}_e \right] : \mathbf{l}_e + \left( \alpha \boldsymbol{\sigma} : \mathbf{1} - \rho \frac{\partial \varphi}{\partial \theta} - \rho \eta \right) \dot{\theta} \\ + \boldsymbol{\sigma} : \left\{ \frac{1}{2} \mathbf{F}^{-\top} \left[ \mathbf{C} \mathbf{C}_p^{-1} \dot{\mathbf{C}}_p \right] \mathbf{F}^{-1} \right\} - \rho \frac{\partial \varphi}{\partial \dot{\boldsymbol{\chi}}_p} \cdot \dot{\boldsymbol{\chi}}_p \\ - \rho \sum_{n=1}^{N_s} \frac{\partial \varphi}{\partial y_n} \dot{y}_n - \frac{1}{\theta} \vec{\mathbf{q}} \cdot \nabla \theta \geq 0. \end{aligned} \quad (2.26)$$

As per the usual Coleman-Noll procedure [15], we conclude that the Cauchy stress is given by

$$\boldsymbol{\sigma} = 2\rho \frac{\partial \varphi}{\partial \mathbf{b}_e} \mathbf{b}_e = \frac{2}{J_e} \frac{\partial W_e}{\partial \mathbf{b}_e} \mathbf{b}_e, \quad (2.27)$$

where  $W_e(\mathbf{b}_e, \theta) = \widehat{W}_e + U_e$ . We also conclude that the entropy reads

$$\eta = \frac{\alpha \boldsymbol{\sigma} : \mathbf{1}}{\rho} - \frac{\partial \varphi}{\partial \theta} \Big|_{\mathbf{b}_e} = - \frac{\partial \varphi}{\partial \theta} \Big|_{\mathbf{F}}. \quad (2.28)$$

Finally, we obtain the respective chemical, thermal, and plastic dissipation inequalities as

$$\mathcal{D}_c \equiv - \sum_{n=1}^{N_s} \frac{\partial \varphi}{\partial y_n} \dot{y}_n \geq 0, \quad (2.29a)$$

$$\mathcal{D}_\theta \equiv - \frac{1}{\theta} \vec{\mathbf{q}} \cdot \nabla \theta \geq 0, \quad (2.29b)$$

$$\mathcal{D}_p \equiv \frac{1}{\rho} \boldsymbol{\sigma} : \left\{ \frac{1}{2} \mathbf{F}^{-\top} \left[ \mathbf{C} \mathbf{C}_p^{-1} \dot{\mathbf{C}}_p \right] \mathbf{F}^{-1} \right\} - \frac{\partial \varphi}{\partial \dot{\boldsymbol{\chi}}_p} \cdot \dot{\boldsymbol{\chi}}_p \geq 0. \quad (2.29c)$$

Using Eqs. 2.19 and 2.23, Eqs. 2.27 and 2.28, as well as Eq. 2.29 in Eq. 2.18 and rearranging yields

$$\rho \dot{e} = \rho \theta \dot{\eta} + \boldsymbol{\sigma} : \mathbf{l} - \rho (\mathcal{D}_c + \mathcal{D}_p). \quad (2.30)$$

Using this result in Eq. 2.6, simplifying, and rearranging gives the entropy form of the conservation of energy as

$$\rho\theta\dot{\eta} = -\nabla \cdot \bar{\mathbf{q}} + \rho(\mathcal{D}_c + \mathcal{D}_p + r). \quad (2.31)$$

Finally, using Eq. 2.24 in Eq. 2.31 and rearranging gives

$$\rho c_p \dot{\theta} + \nabla \cdot \bar{\mathbf{q}} = \rho(r + q_c + q_e + q_p) \quad \text{in } \Omega \times \mathbb{R}^+, \quad (2.32)$$

where

$$c_p \equiv \theta \frac{\partial \eta}{\partial \theta} \Big|_{\mathbf{b}_e} = {}^0c_v + \frac{9\alpha^2\theta}{\rho}(\kappa/J + p) + 3\frac{d\alpha}{d\theta}\theta\frac{p}{\rho} - \alpha \boldsymbol{\ell}_e : \mathbf{1} - \theta \frac{\partial^2 \varphi_e}{\partial \theta^2} \Big|_{\mathbf{b}_e}, \quad (2.33)$$

is the specific heat (at constant elastic strains and, thus, constant pressure). Here,  $\boldsymbol{\ell}_e \equiv -\theta(\partial\sigma/\partial\theta|_{\mathbf{b}_e})/\rho$  is the spatial latent heat tensor at constant elastic strains. It can readily be shown that  $\boldsymbol{\ell}_e : \mathbf{1} = -3p\theta(\kappa'/\kappa)/\rho$  where  $\kappa' = d\kappa/d\theta$ . The respective chemical, elastic, and plastic heating terms are

$$q_c \equiv \mathcal{D}_c - \sum_{n=1}^{N_s} \theta \frac{\partial \eta}{\partial y_n} \dot{y}_n = - \sum_{n=1}^{N_s} \left( \frac{\partial \varphi}{\partial y_n} + \theta \frac{\partial \eta}{\partial y_n} \right) \dot{y}_n = - \sum_{n=1}^{N_s} \frac{\partial e}{\partial y_n} \dot{y}_n, \quad (2.34a)$$

$$q_e \equiv - \left[ 2\theta \frac{\partial \eta}{\partial \mathbf{b}_e} \mathbf{b}_e \right] : \mathbf{l}_e, \quad (2.34b)$$

$$q_p \equiv \mathcal{D}_p - \theta \frac{\partial \eta}{\partial \bar{\boldsymbol{\chi}}_p} \cdot \dot{\bar{\boldsymbol{\chi}}}_p. \quad (2.34c)$$

Here, we have used Eq. 2.12 in Eq. 2.34a. It is straightforward to show that the specific heat at constant total deformation (i.e., constant volume) can be computed as

$$c_v \equiv \theta \frac{\partial \eta}{\partial \theta} \Big|_{\mathbf{F}} = -\theta \frac{\partial^2 \varphi}{\partial \theta^2} \Big|_{\mathbf{F}} = c_p - \alpha \boldsymbol{\ell} : \mathbf{1}, \quad (2.35)$$

where  $\boldsymbol{\ell} \equiv -\theta(\partial\boldsymbol{\sigma}/\partial\theta|_{\mathbf{F}})/\rho$  is the spatial latent heat tensor at constant total strain. It can readily be shown that  $\boldsymbol{\ell} : \mathbf{1} = [9\alpha\theta(\mathbb{J}_e \partial^2 U_e / \partial \mathbb{J}_e^2) - 3p\theta(\kappa'/\kappa)]/\rho$ . By noting that, at the reference state,  $\mathbb{J}_e = 1$ ,  $p = 0$ , and  $\rho = \rho_0$ , for typical volumetric elastic potentials (e.g., Eq. 2.16c), we recover the canonical relation between the heat capacities as

$${}^0c_v = {}^0c_p - \frac{9\alpha_0^2\theta_0\kappa_0}{\rho_0}, \quad (2.36)$$

where  $\alpha_0 = \alpha(\theta_0)$ ,  $\kappa_0 = \kappa(\theta_0)$ , and  $\partial^2 U_e / \partial \mathbb{J}_e^2(\mathbb{J}_e = 1) \rightarrow \kappa$  [22]. Here,  ${}^0c_p$  is the initial state specific heat capacity at constant pressure.

By the principle of maximum plastic dissipation [76, 77], we must maximize Eq. 2.29c, subject to the constraint that the yield function is less than or equal to 0. This corresponds to the constrained optimization problem, formulated in the unstressed configuration,

$$\text{maximize } \mathcal{L}_p \equiv \rho_\theta \mathcal{D}_p - \dot{\lambda}_p f_p, \quad (2.37)$$

where  $\rho_\theta$  is the density in the unstressed configuration and  $\dot{\lambda}_p$  serves as the plastic consistency variable. Noting that  $\rho_0 = \mathbb{J}_p \mathbb{J}_\theta \rho_\theta = J\rho$  such that  $\rho_\theta/\rho = J/(\mathbb{J}_p \mathbb{J}_\theta) = \mathbb{J}_e$ ,  $\mathcal{L}_p$  becomes

$$\begin{aligned} \mathcal{L}_p &= [\mathbb{J}_e \boldsymbol{\sigma}] : \left\{ \frac{1}{2} \mathbf{F}^{-\top} \left[ \mathbf{C} \mathbf{C}_p^{-1} \dot{\mathbf{C}}_p \right] \mathbf{F}^{-1} \right\} - \rho_\theta \frac{\partial \varphi}{\partial \bar{\boldsymbol{\chi}}_p} \cdot \dot{\bar{\boldsymbol{\chi}}}_p - \dot{\lambda}_p f_p, \\ &= \boldsymbol{\tau}_e : \left\{ \frac{1}{2} \mathbf{F}^{-\top} \left[ \mathbf{C} \mathbf{C}_p^{-1} \dot{\mathbf{C}}_p \right] \mathbf{F}^{-1} \right\} + \mathbf{k} \cdot \dot{\bar{\boldsymbol{\chi}}}_p - \dot{\lambda}_p f_p, \end{aligned} \quad (2.38)$$

where we define  $\mathbf{k} \equiv -\rho_\theta \partial\varphi/\partial\bar{\chi}_p$ . The condition  $\partial\mathcal{L}_p/\partial\tau_e = \mathbf{0}$  gives the flow rule as

$$\begin{aligned} \frac{1}{2}\mathbf{F}^{-\top} \left[ \mathbf{C} \mathbf{C}_p^{-1} \dot{\mathbf{C}}_p \right] \mathbf{F}^{-1} &= \dot{\lambda}_p \mathbf{n}, \\ &\iff \\ -\frac{1}{2}\mathbf{F} \left[ \dot{\mathbf{C}}_p^{-1} \mathbf{C}_p \mathbf{C}^{-1} \right] \mathbf{F}^\top &= \dot{\lambda}_p \mathbf{n}, \end{aligned} \quad (2.39)$$

where  $\mathbf{n} \equiv \partial f/\partial\tau_e$  is the normal to the yield surface. The condition  $\partial\mathcal{L}_p/\partial\mathbf{k} = \mathbf{0}$  gives the hardening law as

$$\dot{\bar{\chi}}_p = \dot{\lambda}_p \frac{\partial f_p}{\partial \mathbf{k}}. \quad (2.40)$$

Finally, the complementarity condition requires

$$\dot{\lambda}_p f_p = 0. \quad (2.41)$$

It's worth noting that  $\mathbf{C}_p \mathbf{C}^{-1} = \vartheta^{-2} \mathbf{F}^\top \mathbf{b}_e^{-1} \mathbf{F}^{-\top}$  such that Eq. 2.39 can be expressed as

$$-\frac{1}{2}\vartheta^{-2} \mathbf{F} \dot{\mathbf{C}}_p^{-1} \mathbf{F}^\top \mathbf{b}_e^{-1} = \dot{\lambda}_p \mathbf{n}, \quad (2.42)$$

or simply

$$-\frac{1}{2}\mathbf{F} \dot{\mathbf{C}}_p^{-1} \mathbf{F}^\top = \dot{\lambda}_p \mathbf{n} (\vartheta^2 \mathbf{b}_e). \quad (2.43)$$

We note that  $\vartheta^2 \mathbf{b}_e = (J/J_p)^{2/3} \widehat{\mathbf{b}}_e$ , where the volume preserving component of a strain tensor is given as  $\widehat{(\bullet)} = \det(\bullet)^{-1/3}(\bullet)$ . Therefore, for  $J_p = 1$ , we have the flow

rule in the spatial description,

$$-\frac{1}{2}\mathbf{F}\dot{\mathbf{C}}_p^{-1}\mathbf{F}^\top = \dot{\lambda}_p \mathbf{n} J^{2/3} \widehat{\mathbf{b}}_e. \quad (2.44)$$

Note that this flow rule is entirely similar to that derived in [76]. Namely, in the isothermal limit ( $\theta \rightarrow \theta_0$ ),  $\mathbf{F}\dot{\mathbf{C}}_p^{-1}\mathbf{F}^\top = \mathcal{L}_v(\mathbf{b}_e)$ , the Lie derivative [82] of  $\mathbf{b}_e$ , and  $\mathbf{J} = J_e$  such that  $J^{2/3} \widehat{\mathbf{b}}_e = \mathbf{b}_e$ . Finally, the plastic hardening variable is governed by the evolution equation [41],

$$\dot{\epsilon}_p = \sqrt{\frac{2}{3}} \dot{\lambda}_p. \quad (2.45)$$

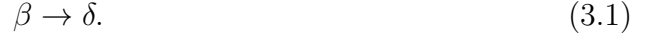
## CHAPTER 3

### MODEL SPECIFICATION

In this section, we use the general theory presented in Chapter 2 and apply it to phase transition in energetic materials (i.e., HMX, PBX).

#### 3.1 Chemistry

We consider a one step reaction ( $N_r = 1$ ) for the  $\beta \rightarrow \delta$  phase transition of HMX as



We note that the molar masses are identical,  $M_\beta = M_\delta = M$ , and that  $\nu'_\beta = 1$ ,  $\nu'_\delta = 0$  with  $y_\beta + y_\delta = 1 \rightarrow y_\beta = 1 - y_\delta$ . Utilizing these identities, Eq. 2.9 and Eq. 2.13 simplify to

$$\dot{y}_n = \nu_n k_c (1 - y_\delta), \quad (3.2)$$

where the reaction rate constant, Eq. 2.14, becomes simply  $k_c$  for  $m = 1$ . I.e., we have

$$r_c = k_c \frac{\rho(1 - y_\delta)}{M}, \quad (3.3a)$$

$$k_c = A\hat{A}(\theta) \exp\left(-\frac{E_a}{R_u\theta}\right). \quad (3.3b)$$

Substituting this into Eq. 2.34a, the chemical heating term reads

$$q_c = -\sum_{n=1}^{N_s} e_n \nu_n k_c (1 - y_\delta) = -k_c (1 - y_\delta) \Delta e^{\text{rxn}}, \quad (3.4)$$

where  $e_n = \partial e / \partial y_n$  and  $\Delta e^{\text{rxn}} = \sum_{n=1}^{N_s} e_n \nu_n = \Delta h^{\text{rxn}} - \Delta(3p/\rho)$  is the change in the internal energy per unit mass for the reaction. Here,  $\Delta h^{\text{rxn}}$  is the heat of reaction per unit mass.

### 3.2 Thermodynamics

In light of Eqs. 2.11 and 2.12, Eqs. 2.15 and 2.16, and Eq. 2.28, we can express entropy as

$$\begin{aligned} \eta = & {}^0c_v \log \left[ \frac{\theta}{\theta_0} \right] + \int_{\theta_0}^{\theta} \frac{9\alpha^2(\hat{\theta})\kappa(\hat{\theta})}{\rho_0} d\hat{\theta} + \frac{3\alpha p}{\rho} - 3\alpha\varphi_e \\ & - \frac{1}{J_e \rho} \left( \frac{\mu'}{\mu} \widehat{W}_e + \frac{\kappa'}{\kappa} U_e \right) - \sum_{n=1}^{N_s} \frac{1}{M_n} \frac{\partial \chi_n}{\partial \theta} y_n, \end{aligned} \quad (3.5)$$

where  $\boldsymbol{\sigma} : \mathbf{1} = 3p$  and  $\mu' = d\mu/d\theta$ . For the elastic potential given by Eq. 2.16, Eq. 2.33 becomes

$$c_p = {}^0c_v + \frac{9\alpha^2\theta}{\rho} (\kappa/J + p) + 3 \frac{d\alpha}{d\theta} \theta \frac{p}{\rho} + 3\alpha\theta \frac{\kappa'}{\kappa} \frac{p}{\rho} - \theta \frac{\partial^2 \varphi_e}{\partial \theta^2} \Big|_{\mathbf{b}_e}, \quad (3.6a)$$

$$\frac{\partial^2 \varphi_e}{\partial \theta^2} \Big|_{\mathbf{b}_e} = 9\alpha^2 \varphi_e + 3 \frac{d\alpha}{d\theta} \varphi_e + \frac{6\alpha}{J_e \rho} \left( \frac{\mu'}{\mu} \widehat{W}_e + \frac{\kappa'}{\kappa} U_e \right) + \frac{1}{J_e \rho} \left( \frac{\mu''}{\mu} \widehat{W}_e + \frac{\kappa''}{\kappa} U_e \right), \quad (3.6b)$$

where  $\mu'' = d^2\mu/d\theta^2$  and  $\kappa'' = d^2\kappa/d\theta^2$ .

### 3.3 Mechanics

For the potential given by Eq. 2.16 and the yield function given by Eq. 2.17, the Cauchy stress,  $\boldsymbol{\tau}_e$ , and the normal to the yield surface become

$$\boldsymbol{\sigma} = \frac{2}{J_e} \frac{\partial W_e}{\partial \mathbf{b}_e} \mathbf{b}_e = (\mu/J_e) \operatorname{dev}[\widehat{\mathbf{b}}_e] + p\mathbf{1}, \quad (3.7a)$$

$$\boldsymbol{\tau}_e = J_e \boldsymbol{\sigma} = \mu \operatorname{dev}[\widehat{\mathbf{b}}_e] + pJ_e \mathbf{1}, \quad (3.7b)$$

$$\mathbf{n} = \frac{\operatorname{dev}[\boldsymbol{\tau}_e]}{\|\operatorname{dev}[\boldsymbol{\tau}_e]\|}, \quad (3.7c)$$

where  $p \equiv \partial U_e / \partial J_e$  is pressure. We model HMX as a hyperelastic solid such that  $\mathbf{F}_p = \mathbf{1}$  while Eq. 2.44 becomes  $\mathbf{0}$ . For the binder, using Eq. 3.7b to express  $\widehat{\mathbf{b}}_e$  as  $\widehat{\mathbf{b}}_e = \operatorname{dev}[\boldsymbol{\tau}_e] / \mu + (1/3) \operatorname{tr}(\widehat{\mathbf{b}}_e) \mathbf{1} = (\|\operatorname{dev}[\boldsymbol{\tau}_e]\| / \mu) \mathbf{n} + (1/3) \operatorname{tr}(\widehat{\mathbf{b}}_e) \mathbf{1}$ , Eq. 2.44 becomes

$$-\frac{1}{2} \mathbf{F} \dot{\mathbf{C}}_p^{-1} \mathbf{F}^\top = \dot{\lambda}_p \mathbf{n} J^{2/3} \left[ \frac{\|\operatorname{dev}[\boldsymbol{\tau}_e]\|}{\mu} \mathbf{n} + \frac{1}{3} \operatorname{tr}(\widehat{\mathbf{b}}_e) \mathbf{1} \right]. \quad (3.8)$$

From this, by neglecting the first term in brackets which is on the order of the flow stress over the moduli, we obtain an associative flow rule given by

$$\mathbf{F} \dot{\mathbf{C}}_p^{-1} \mathbf{F}^\top = -\frac{2}{3} \dot{\lambda}_p J^{2/3} \operatorname{tr}(\widehat{\mathbf{b}}_e) \mathbf{n}. \quad (3.9)$$

By noting that  $\operatorname{tr}(\widehat{\mathbf{b}}_e) = J^{-2/3} (\widehat{\mathbf{C}}_p^{-1} : \mathbf{C})$ , we rearrange Eq. 3.9 to get the flow rule in the material frame as

$$\dot{\mathbf{C}}_p^{-1} = -\frac{2}{3} \dot{\lambda}_p (\widehat{\mathbf{C}}_p^{-1} : \mathbf{C}) \mathbf{N}, \quad (3.10)$$

where

$$\mathbf{N} \equiv \mathbf{F}^{-1} \mathbf{n} \mathbf{F}^{-\top} = \frac{\operatorname{DEV}[\mathbf{S}]}{\sqrt{[\mathbf{C} \operatorname{DEV}[\mathbf{S}]] : [\operatorname{DEV}[\mathbf{S}] \mathbf{C}]}} \quad (3.11)$$

is the normal to the yield surface in the material frame and  $\dot{\Lambda}_p = \dot{\lambda}_p$  is the material frame plastic consistency parameter. Here,  $\text{DEV}[\bullet] = (\bullet) - (\bullet : \mathbf{C}) \mathbf{C}^{-1}$  is the deviator of a material tensor and  $\mathbf{S}$  is the second (symmetric) Piola-Kirchhoff tensor. These quantities are further elaborated upon in Appendix A.2. It's worth noting that, using Eq. 3.9 and the identity  $\dot{\mathbf{C}}_p = -\mathbf{C}_p \dot{\mathbf{C}}_p^{-1} \mathbf{C}_p$ , Eq. 2.29c can be written as

$$\mathcal{D}_p = \frac{\dot{\lambda}_p}{\rho} \boldsymbol{\sigma} : \mathbf{n} - \frac{\partial \varphi}{\partial \vec{\chi}_p} \cdot \dot{\vec{\chi}}_p \geq 0. \quad (3.12)$$

The elastic heating term can be computed by substituting Eqs. 2.27 and 3.5 in Eq. 2.34b to get

$$\begin{aligned} q_e &= - \left[ 2\theta \frac{\partial \eta}{\partial \mathbf{b}_e} \mathbf{b}_e \right] : \mathbf{l}_e = \frac{3\alpha\theta}{\rho} \left[ \text{dev}[\boldsymbol{\sigma}] - \left( J_e \frac{\partial^2 U_e}{\partial J_e^2} \right) \mathbf{1} \right] : \mathbf{l}_e, \\ &= \frac{3\alpha\theta}{\rho} \left[ \text{dev}[\boldsymbol{\sigma}] - \left( J_e \frac{\partial^2 U_e}{\partial J_e^2} \right) \mathbf{1} \right] : \mathbf{d}_e, \end{aligned} \quad (3.13)$$

where  $\mathbf{d}_e = [\mathbf{l}_e]^{\text{sym}}$  is the elastic symmetric velocity gradient. Here, we have noted that  $J_e = [\det(\mathbf{b}_e)]^{1/2}$  which gives  $\partial J_e / \partial \mathbf{b}_e = J_e \mathbf{b}_e^{-1} / 2$ . Moreover, we note that the tensor in brackets is symmetric. By taking the symmetric part of Eq. 2.19 yields

$$\begin{aligned} \mathbf{d}_e &= \mathbf{d} - \frac{1}{2} \mathbf{F}^{-\top} \left[ \mathbf{C} \mathbf{C}_p^{-1} \dot{\mathbf{C}}_p \right]^{\text{sym}} \mathbf{F}^{-1} - \alpha \dot{\theta} \mathbf{1}, \\ &= \frac{1}{2} \mathbf{F}^{-\top} \left[ \dot{\mathbf{C}} - \left[ \mathbf{C} \mathbf{C}_p^{-1} \dot{\mathbf{C}}_p \right]^{\text{sym}} - 2\alpha \dot{\theta} \mathbf{C} \right] \mathbf{F}^{-1}, \end{aligned} \quad (3.14)$$

where  $\mathbf{d} = [\mathbf{l}]^{\text{sym}} = \mathbf{F}^{-\top} \dot{\mathbf{C}} \mathbf{F}^{-1} / 2$  is the total symmetric velocity gradient. Noting from Eq. 2.28 that  $\partial \eta / \partial \vec{\chi}_p = \mathbf{0}$  since  $\varphi_p$  has no temperature dependence in our formulation, making use of Eq. 2.44 and the identity  $\dot{\mathbf{C}}_p = -\mathbf{C}_p \dot{\mathbf{C}}_p^{-1} \mathbf{C}_p$ , the plastic heating term, Eq. 2.34c, becomes

$$q_p = \mathcal{D}_p = \frac{\dot{\lambda}_p}{\rho} \boldsymbol{\sigma} : \mathbf{n} - \frac{\partial \varphi}{\partial \vec{\chi}_p} \cdot \dot{\vec{\chi}}_p \approx \frac{f_{\text{TQ}}}{\rho} \dot{\lambda}_p \boldsymbol{\sigma} : \mathbf{n}. \quad (3.15)$$

As previously noted, little is known on closed forms of the plastic part of the Helmholtz energy,  $\varphi_p$ , due to the nature of cold work. As such, the term in Eq. 3.15,  $(\partial\varphi/\partial\vec{\chi}_p) \cdot \dot{\vec{\chi}}_p$ , is approximated as the product of the first term and  $(1 - f_{TQ})$  where  $f_{TQ} \in (0, 1)$  is the Taylor-Quinney factor [25, 91].

We utilize the nonlinear model for the CTE given by Eq. 5.3 and the nonlinear model for the bulk modulus given by Eq. 5.6. The shear modulus is computed using Eq. 5.6 with the canonical relation  $\mu(\theta) = 3\kappa(\theta)(1 - 2\nu)/(2(1 + \nu))$  where  $\nu$  is the Poisson ratio.

## CHAPTER 4

### NUMERICAL IMPLEMENTATION

#### 4.1 Chemo-thermal Solver Spatial Discretization

In order to employ the finite element method in solving Eqs. 2.8 and 2.9, we introduce the following function spaces for the mass fraction field

$$\Upsilon := \left\{ Y({}^0\vec{x}, t) \in H^k(\Omega_0) \mid Y({}^0\vec{x}, t) = \tilde{Y}({}^0\vec{x}, t) \text{ on } {}^0\Gamma_D \times (0, \mathcal{T}] \right\}, \quad (4.1a)$$

$$\delta\Upsilon := \left\{ \delta Y({}^0\vec{x}) \in H^k(\Omega_0) \mid \delta Y({}^0\vec{x}) = 0 \text{ on } {}^0\Gamma_D \right\}, \quad (4.1b)$$

and temperature field

$$\Theta := \left\{ \theta({}^0\vec{x}, t) \in H^k(\Omega_0) \mid \theta({}^0\vec{x}, t) = \tilde{\theta}({}^0\vec{x}, t) \text{ on } {}^0\Gamma_D \times (0, \mathcal{T}] \right\}, \quad (4.2a)$$

$$\delta\Theta := \left\{ \delta\theta({}^0\vec{x}) \in H^k(\Omega_0) \mid \delta\theta({}^0\vec{x}) = 0 \text{ on } {}^0\Gamma_D \right\}, \quad (4.2b)$$

where  $H^k(\Omega_0)$ ,  $k \in \{1, 2\}$  are standard Sobolev spaces [1]. The existence and uniqueness of the solution will not be addressed in this dissertation. We proceed under the assumption that the relevant initial and boundary value problems admit workable solutions in the aforementioned spaces; thereby, we construct numerical approximations of the solution (see, for example, [8] for further discussion).

## 4.2 Mechanical Solver Spatial Discretization

### 4.2.1 Three-field de Veubeke-Hu-Washizu Variational Principle

To enable the modeling of both compressible and ‘nearly incompressible’ solids, we derive a three field method for the mechanical solver by introducing the ‘mechanical volume’  $\gamma$  as an independent variable

$$\gamma = \mathbf{J}_e \tag{4.3}$$

where Eq. 4.3 is enforced in a weak sense [85] using Lagrange multiplier  $p$  which constitutes the third field of the formulation. The associated Lagrange functional is given as

$$V = \int_{\Omega_0} \left[ \widehat{W}_e(\mathbf{b}_e) + U_e(\gamma) + p(\mathbf{J}_e - \gamma) \right] \mathbf{J}_p \mathbf{J}_\theta \, d\Omega_0, \tag{4.4a}$$

$$\delta V = \mathcal{R}_u + \mathcal{R}_p + \mathcal{R}_\gamma. \tag{4.4b}$$

Taking the appropriate variations of  $V$  gives the residual equations as

$$\mathcal{R}_u \equiv \delta_u V = \int_{\Omega_0} \boldsymbol{\tau}_{ij} : \delta \mathbf{e}_{ij} \, d\Omega_0, \tag{4.5a}$$

$$\mathcal{R}_p \equiv \delta_p V = \int_{\Omega_0} \delta p [\mathbf{J} - \gamma \mathbf{J}_\theta \mathbf{J}_p] \, d\Omega_0, \tag{4.5b}$$

$$\mathcal{R}_\gamma \equiv \delta_\gamma V = \int_{\Omega_0} \delta \gamma [U'_e(\gamma, \theta) - p] \mathbf{J}_\theta \mathbf{J}_p \, d\Omega_0. \tag{4.5c}$$

Eq. 4.5 is solved simultaneously using Newton-Raphson iteration, where the system of equations is given as

$$\begin{bmatrix} \mathcal{K}_{uu} & \mathcal{K}_{up} & \mathcal{K}_{u\gamma} \\ \mathcal{K}_{pu} & \mathcal{K}_{pp} & \mathcal{K}_{p\gamma} \\ \mathcal{K}_{\gamma u} & \mathcal{K}_{\gamma p} & \mathcal{K}_{\gamma\gamma} \end{bmatrix} \begin{bmatrix} \Delta \bar{\mathbf{u}}_{n+1}^{(k+1)} \\ \Delta p_{n+1}^{(k+1)} \\ \Delta \gamma_{n+1}^{(k+1)} \end{bmatrix} = - \begin{bmatrix} \mathcal{R}_u \\ \mathcal{R}_p \\ \mathcal{R}_\gamma \end{bmatrix} \quad (4.6)$$

The associated tangents are

$$\mathcal{K}_{uu} = \int_{\Omega_0} [\delta \mathbf{e}_{ij} : \mathbf{a}_{ijkl} : \delta \mathbf{e}_{kl} + \boldsymbol{\tau}_{ij} : \delta \delta \mathbf{e}_{ij}] d\Omega_0, \quad (4.7a)$$

$$\mathcal{K}_{up} = \int_{\Omega_0} \mathbf{J} \delta_{ij} : \delta \mathbf{e}_{ij} \delta p d\Omega_0 = \mathcal{K}_{pu}^T, \quad (4.7b)$$

$$\mathcal{K}_{u\gamma} = \mathcal{K}_{\gamma u}^T = 0, \quad (4.7c)$$

$$\mathcal{K}_{pp} = 0, \quad (4.7d)$$

$$\mathcal{K}_{\gamma p} = - \int_{\Omega_0} \delta \gamma \delta p \mathbf{J}_\theta \mathbf{J}_p d\Omega_0 = \mathcal{K}_{p\gamma}^T, \quad (4.7e)$$

$$\mathcal{K}_{\gamma\gamma} = \int_{\Omega_0} \delta \gamma \delta \gamma U_e''(\gamma, \theta) \mathbf{J}_\theta \mathbf{J}_p d\Omega_0. \quad (4.7f)$$

Explicit formulae for calculating  $\mathbf{a}_{ijkl}$  are provided in Section 4.3.4 while

$$\delta \mathbf{e}_{ij} \equiv [\delta \mathbf{F} \mathbf{F}^{-1}]_{ij}^{\text{sym}}, \quad (4.8a)$$

$$\delta \delta \mathbf{e}_{ij} \equiv [\mathbf{F}^{-T} \delta \mathbf{F}^T \delta \mathbf{F} \mathbf{F}^{-1}]_{ij}. \quad (4.8b)$$

In order to employ the finite element method in solving Eq. 4.5, we introduce the following function spaces for the displacement field,

$$\mathcal{U} := \left\{ \vec{\mathbf{u}}(\vec{\mathbf{x}}, t) \in H^k(\Omega) \mid \vec{\mathbf{u}}(\vec{\mathbf{x}}, t) = \tilde{\vec{\mathbf{u}}}(\vec{\mathbf{x}}, t) \text{ on } \Gamma_D \times (0, \mathcal{T}] \right\}, \quad (4.9a)$$

$$\delta\mathcal{U} := \left\{ \delta\vec{\mathbf{u}}(\vec{\mathbf{x}}) \in H^k(\Omega) \mid \delta\vec{\mathbf{u}}(\vec{\mathbf{x}}) = \mathbf{0} \text{ on } \Gamma_D \right\}, \quad (4.9b)$$

pressure field,

$$\mathcal{P} := \left\{ p(\vec{\mathbf{x}}, t) \in H^0(\Omega) \right\}, \quad (4.10a)$$

$$\delta\mathcal{P} := \left\{ \delta p(\vec{\mathbf{x}}, t) \in H^0(\Omega) \right\}, \quad (4.10b)$$

and mechanical volume field,

$$\Gamma := \left\{ \gamma(\vec{\mathbf{x}}, t) \in H^0(\Omega) \right\}, \quad (4.11a)$$

$$\delta\Gamma := \left\{ \delta\gamma(\vec{\mathbf{x}}, t) \in H^0(\Omega) \right\}, \quad (4.11b)$$

where  $H^k(\Omega)$ ,  $k \in \{0, 1, 2\}$  are standard Sobolev spaces [1]. As mentioned before, the existence and uniqueness of the solution will not be addressed in this dissertation. We, again, proceed under the assumption that the relevant initial and boundary value problems admit workable solutions in the aforementioned spaces; thereby, we construct numerical approximations of the solution.

#### 4.2.2 Generalized Plane Strain Condition

Generalized plane strain conditions are used in order to reduce the three dimensional problem to a two dimensional one [70]. The motion in the third dimension is taken to be a uniform stretch given by  $u_z(Z, t) = (s(t) - 1) Z$  where  $s(t)$  is chosen to

minimize the residual given by

$$\mathcal{R}_z(t) \equiv \frac{1}{\Omega} \int_{\Omega} \left[ \sigma_{zz} - \frac{1}{2}(\sigma_{xx} + \sigma_{yy}) \right] d\Omega = \frac{1}{\Omega} \int_{\Omega} -\frac{3}{2}(\sigma_{xx}^{\text{dev}} + \sigma_{yy}^{\text{dev}}) d\Omega. \quad (4.12)$$

This is done in order to emulate an isotropic stress response. This equates to modifying the deformation gradient at each gauss point as  $\mathbf{F}_{zz}(t) = s(t)$ . Minimization of Eq. 4.12 is performed as a separate sub-cycle in the staggered scheme using the secant method.

### 4.3 Temporal Discretization

#### 4.3.1 Adaptive Time Stepping

We use an adaptive time stepping scheme in which the time step size varies with the nonlinear CTE of the HMX particles as

$$\begin{aligned} \delta(\theta_{\Gamma}) &\equiv 1 + 4 \left( \frac{\Delta t_{\max}}{\Delta t_{\min}} - 1 \right) \frac{e^{-\omega(\theta_{\Gamma} - \theta_T)}}{[1 + e^{-\omega(\theta_{\Gamma} - \theta_T)}]^2}, \\ \Delta t(\theta_{\Gamma}) &:= \Delta t_{\max} / \delta(\theta_{\Gamma}), \end{aligned} \quad (4.13)$$

where  $\omega$  and  $\theta_T$  are the same parameters as those discussed later in Eq. 5.3 and  $\theta_{\Gamma}$  is the (prescribed) temperature at the boundary of the domain. Here,  $\Delta t_{\max}$  and  $\Delta t_{\min}$  are user prescribed parameters which determine the maximum and minimum time steps taken in the simulation, respectively. Figure 4.1 graphically depicts the qualitative form of Eq. 4.13. The actual values for  $\Delta t_{\max}$  and  $\Delta t_{\min}$  for simulations described in Chapters 6 and 7 are given in Sections 6.1 and 7.1.

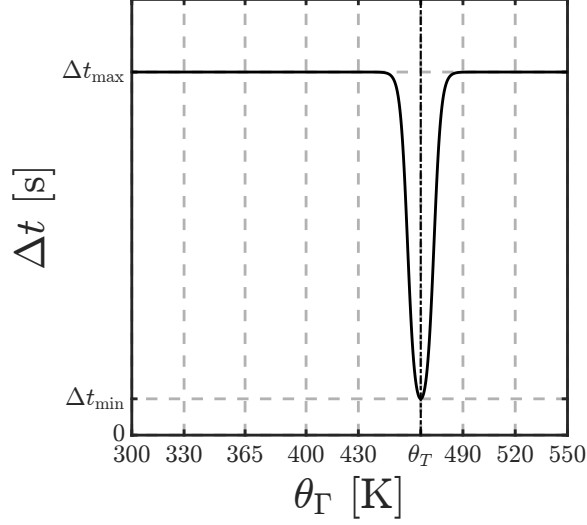


Figure 4.1. Graphical depiction of the prescribed adaptive time step.

### 4.3.2 Staggered Solution Strategy

Figure 4.2 shows an overview of the staggered solution strategy used to solve a full CTM problem. Given the fields at time  $t_n$  for a given time discretization, the CT solver computes the thermal and species fields for time step  $t_{n+1}$  for the first subcycle ( $k = 0$ ) by Newton-Raphson iteration ( $j$ ) with convergence criteria defined as

$$r_{n+1}^{k,j} \equiv \frac{\left\| \mathcal{R}_{n+1}^{k,j} \right\|}{\left\| \mathcal{R}_{n+1}^{k=0,j=0} \right\|} < \text{TOL} \quad (4.14)$$

for small tolerance TOL, typically on the order  $10^{-5}$ . These newly calculated fields are then used, as needed, by the generalized plane strain solver to compute  $s(t)$  required for Eq. 4.12. In turn, the intermediate computed fields are used by the mechanical solver to compute the remaining mechanical fields for time step  $t_{n+1}$  with the same criteria. With the new thermal, species, and mechanical fields, the

convergence criteria Eq. 4.14 are again checked for each field. If each is satisfied, the solutions are considered converged and the time step is propagated; otherwise, the solvers are each called again with these new fields for another subcycle. The number of subcycles required for the simulations described in Chapters 6 and 7 are given in Sections 6.1 and 7.1.

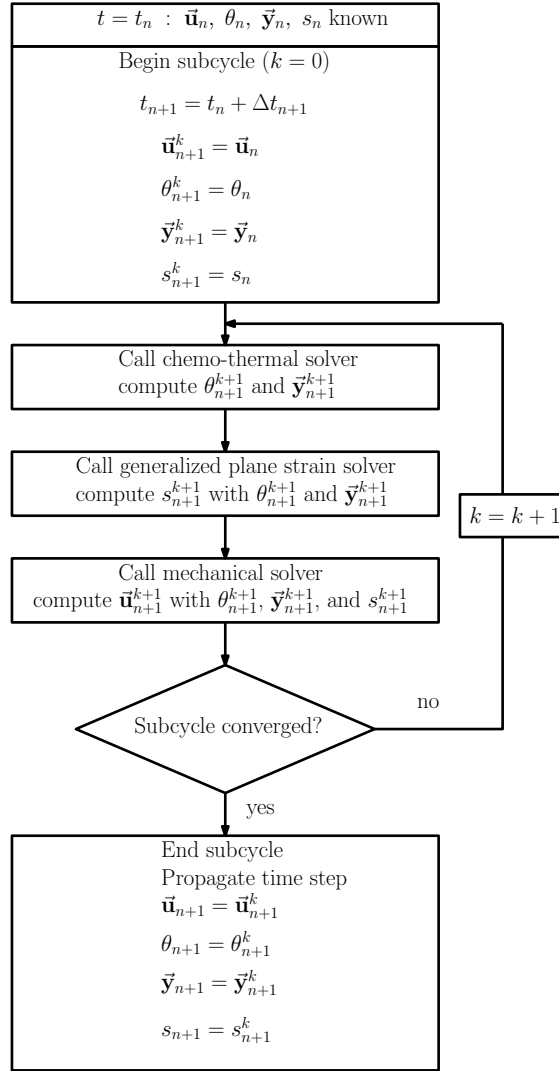


Figure 4.2. Diagram of the CTM solver algorithm.

### 4.3.3 Chemical Integration Algorithm

As previously mentioned, the thermo-chemical and mechanical fields are solved using a staggered scheme (isothermal split) until a global convergence is met [27]. In this manner, the conservation of chemical species, Eq. 2.9, is solved at the Gauss points using a forward finite difference scheme performed during the thermal solver routine. The discretization is given as

$$[\vec{\mathbf{y}}]_{n+1} = [\vec{\mathbf{y}}]_n + \frac{[\Delta t]_{n+1}}{[\rho]_n} \vec{\mathbf{M}} \boldsymbol{\nu} [\vec{\mathbf{r}}_c]_n, \quad (4.15)$$

where  $\vec{\mathbf{y}}$  and  $\vec{\mathbf{M}}$  are vectors of the chemical species mass fractions and their corresponding molar masses,  $\boldsymbol{\nu}$  is a matrix of stoichiometric coefficients with row corresponding to species and column corresponding to reaction number, and  $\vec{\mathbf{r}}_c$  is a vector of the rates of reaction for each reaction.

### 4.3.4 Plastic Integration Algorithm

As previously mentioned, the thermo-chemical and mechanical fields are solved using a staggered scheme (isothermal split) until a global convergence is met [27]. The integration of Eq. 3.9 is done by means of an elastic predictor / plastic corrector algorithm performed in the material frame to preserve objectivity. The process begins with a configuration update using given displacement and temperature fields,

$$[\mathbf{F}]_{n+1} = \mathbf{1} + {}^0\nabla [\vec{\mathbf{u}}]_{n+1}, \quad (4.16a)$$

$$[\mathbf{J}]_{n+1} = \det([\mathbf{F}]_{n+1}), \quad (4.16b)$$

$$[\mathbf{J}_\theta]_{n+1} = \vartheta^3([\theta]_{n+1}). \quad (4.16c)$$

Eq. 3.10 as well as the hardening law, Eq. 2.45, are discretized in time using backward Euler finite difference schemes given by

$$[\mathbf{C}_p^{-1}]_{n+1} = [\mathbf{C}_p^{-1}]_n - \frac{2}{3}\Delta\lambda_p \left( [\widehat{\mathbf{C}}_p^{-1}]_{n+1} : [\mathbf{C}]_{n+1} \right) [\mathbf{N}]_{n+1} \quad (4.17a)$$

$$[\varepsilon_p]_{n+1} = [\varepsilon_p]_n + \sqrt{\frac{2}{3}}\Delta\lambda_p, \quad (4.17b)$$

where, for convenience, we use  $\Delta\lambda_p$  universally. We continue by obtaining the trial elastic predictor state by ‘freezing’ plastic flow such that the plastic configuration remains unchanged. This amounts to supposing  $\Delta\lambda_p = 0$ , such that Eq. 4.17 yields

$$[\widetilde{\mathbf{C}}_p^{-1}] = [\mathbf{C}_p^{-1}]_n, \quad (4.18a)$$

$$[\widetilde{\varepsilon}_p] = [\varepsilon_p]_n, \quad (4.18b)$$

where  $[\widetilde{\bullet}]$  indicates the trial state of quantity  $\bullet$ . Eq. 4.18a is then pushed forward to the material configuration in order to compute

$$[\widetilde{\mathbf{b}}_e] = [\mathbf{J}^{-2/3}]_{n+1} [\mathbf{F}]_{n+1} [\widetilde{\mathbf{C}}_p^{-1}] [\mathbf{F}^T]_{n+1}, \quad (4.19a)$$

$$\text{dev}[\widetilde{\boldsymbol{\tau}}_e] = \mu \text{dev}[\widetilde{\mathbf{b}}_e] = \mu \left( [\widetilde{\mathbf{b}}_e] - \frac{1}{3} \text{tr}(\widetilde{\mathbf{b}}_e) \mathbf{1} \right), \quad (4.19b)$$

$$[\widetilde{f}_p] = \left\| \text{dev}[\widetilde{\boldsymbol{\tau}}_e] \right\| - \sqrt{\frac{2}{3}} \left( \sigma_0 + H [\widetilde{\varepsilon}_p] \right). \quad (4.19c)$$

Eq. 4.19c, along with the discrete Kuhn-Tucker complementarity conditions,

$$\Delta\lambda_p \geq 0, \quad (4.20a)$$

$$f_p \leq 0, \quad (4.20b)$$

$$\Delta\lambda_p f_p = 0, \quad (4.20c)$$

allows us to assess the admissibility of our trial elastic state. In the case of  $[\widetilde{f}_p] \leq 0$ , the result of the elastic predictor is a state which obeys Eq. 4.20 such that the trial elastic step is, indeed, the solution for timestep  $t_{n+1}$ . However, in the case that  $[\widetilde{f}_p] > 0$ , it follows that our trial state is nonadmissible. Namely,  $[\boldsymbol{\tau}_e]_{n+1} \neq [\widetilde{\boldsymbol{\tau}_e}]$ , which implies that  $[\widehat{\mathbf{b}}_e]_{n+1} \neq [\widetilde{\widehat{\mathbf{b}}_e}]$ , which further implies that  $[\mathbf{C}_p^{-1}]_{n+1} \neq [\widetilde{\mathbf{C}_p^{-1}}]$ , such that we must have  $\Delta\lambda_p > 0$ . In such a case, we have a plastic step and must perform a radial return mapping. We begin by noting that, since  $\text{TR}([\mathbf{N}]_{n+1}) = 0$ , we have from Eq. 4.17a that

$$\text{TR}([\mathbf{C}_p^{-1}]_{n+1}) = \text{TR}([\widetilde{\mathbf{C}_p^{-1}}]), \quad (4.21)$$

regardless of the value of  $\Delta\lambda_p$ . Here, the trace of a material tensor is given as  $\text{TR}(\bullet) = \bullet : \mathbf{C}$ . In this case, it is easy to show that  $\text{TR}(\mathbf{N}) = \text{tr}(\mathbf{n}) = 0$ . Eq. 4.21 also implies that  $\text{tr}([\widehat{\mathbf{b}}_e]_{n+1}) = \text{tr}([\widetilde{\widehat{\mathbf{b}}_e}])$ . Substituting these equations into Eqs. 4.17a and 4.19a, then using the results in Eq. 4.19b applied to the  $t_{n+1}$  state, we get

$$\begin{aligned} \text{dev}[\boldsymbol{\tau}_e]_{n+1} &= \mu \text{dev}[\widehat{\mathbf{b}}_e] - \frac{2}{3}\mu\Delta\lambda_p \text{tr}([\widetilde{\widehat{\mathbf{b}}_e}]), \\ &= \text{dev}[\widetilde{\boldsymbol{\tau}_e}] - \frac{2}{3}\mu\Delta\lambda_p \text{tr}([\widetilde{\widehat{\mathbf{b}}_e}]) [\mathbf{n}]_{n+1}. \end{aligned} \quad (4.22)$$

From this, we can proceed by noting that  $\text{dev}[\boldsymbol{\tau}_e]_{n+1} = \|\text{dev}[\boldsymbol{\tau}_e]_{n+1}\| [\mathbf{n}]_{n+1}$  and  $\text{dev}[\widetilde{\boldsymbol{\tau}_e}] = \|\text{dev}[\widetilde{\boldsymbol{\tau}_e}]\| [\widetilde{\mathbf{n}}]$ . Using these, we can recast Eq. 4.22 to get

$$\begin{aligned} \|\text{dev}[\boldsymbol{\tau}_e]_{n+1}\| [\mathbf{n}]_{n+1} &= \|\text{dev}[\widetilde{\boldsymbol{\tau}_e}]\| [\widetilde{\mathbf{n}}] - \frac{2}{3}\mu\Delta\lambda_p \text{tr}([\widetilde{\widehat{\mathbf{b}}_e}]) [\mathbf{n}]_{n+1}, \\ &\iff \\ \|\text{dev}[\widetilde{\boldsymbol{\tau}_e}]\| [\widetilde{\mathbf{n}}] &= \left( \|\text{dev}[\boldsymbol{\tau}_e]_{n+1}\| + \frac{2}{3}\mu\Delta\lambda_p \text{tr}([\widetilde{\widehat{\mathbf{b}}_e}]) \right) [\mathbf{n}]_{n+1}. \end{aligned} \quad (4.23)$$

Thus, if we require that

$$\begin{aligned}
\left\| \text{dev}[\widetilde{\boldsymbol{\tau}}_e] \right\| &= \left\| \text{dev}[\boldsymbol{\tau}_e]_{n+1} \right\| + \frac{2}{3} \mu \Delta \lambda_p \text{tr} \left( \left[ \widetilde{\mathbf{b}}_e \right] \right), \\
&\iff \\
\left\| \text{dev}[\boldsymbol{\tau}_e]_{n+1} \right\| &= \left\| \text{dev}[\widetilde{\boldsymbol{\tau}}_e] \right\| - \frac{2}{3} \mu \Delta \lambda_p \text{tr} \left( \left[ \widetilde{\mathbf{b}}_e \right] \right), \tag{4.24}
\end{aligned}$$

we can assert that

$$[\mathbf{n}]_{n+1} = [\widetilde{\mathbf{n}}], \tag{4.25}$$

$$\iff$$

$$[\mathbf{N}]_{n+1} = [\widetilde{\mathbf{N}}]. \tag{4.26}$$

In addition, we require that  $[f_p]_{n+1} = 0$ . I.e., we must have

$$\begin{aligned}
[f_p]_{n+1} &= \left\| \text{dev}[\boldsymbol{\tau}_e]_{n+1} \right\| - \sqrt{\frac{2}{3}} (\sigma_0 + H [\varepsilon_p]_{n+1}), \\
&= \left\| \text{dev}[\widetilde{\boldsymbol{\tau}}_e] \right\| - \frac{2}{3} \mu \Delta \lambda_p \text{tr} \left( \left[ \widetilde{\mathbf{b}}_e \right] \right) - \sqrt{\frac{2}{3}} \left( \sigma_0 + H \left[ [\varepsilon_p]_n + \sqrt{\frac{2}{3}} \Delta \lambda_p \right] \right), \\
&= \left\| \text{dev}[\widetilde{\boldsymbol{\tau}}_e] \right\| - \sqrt{\frac{2}{3}} (\sigma_0 + H [\varepsilon_p]_n) - \frac{2}{3} \mu \Delta \lambda_p \text{tr} \left( \left[ \widetilde{\mathbf{b}}_e \right] \right) - \frac{2}{3} H \Delta \lambda_p, \\
&= 0,
\end{aligned}$$

or simply

$$[\widetilde{f}_p] - \frac{2}{3} \left( \mu \text{tr} \left( \left[ \widetilde{\mathbf{b}}_e \right] \right) + H \right) \Delta \lambda_p = 0. \tag{4.27}$$

This allows the determination of  $\Delta\lambda_p > 0$  as

$$\Delta\lambda_p = \frac{(3/2)[\widetilde{f}_p]}{\mu \text{tr}\left(\left[\widetilde{\mathbf{b}}_e\right]\right) + H}. \quad (4.28)$$

Thus the discrete governing equations which define the elastic predictor / plastic corrector return-mapping algorithm are determined. Further discussions on this process are readily available [76, 79] including discussions on the importance of determining the discrete governing equations entirely in terms of the trial elastic state. Furthermore, a concise summary of the algorithm including consistent (exact) tangent terms to be used in Eq. 4.7 is provided below. The algorithm is performed at each Gauss point for each Newton-Raphson iteration of the mechanical solver.

### Spatial Plastic Integration Algorithm

#### 1. Update the configuration.

$$\begin{aligned} [\mathbf{F}]_{n+1} &= \mathbf{1} + {}^0\nabla [\vec{\mathbf{u}}]_{n+1} \\ [J]_{n+1} &= \det([\mathbf{F}]_{n+1}) \\ [J_\theta]_{n+1} &= \vartheta^3([\theta]_{n+1}) \end{aligned}$$

#### 2. Compute trial material elastic predictor state.

$$\begin{aligned} [\widetilde{\mathbf{C}}_p^{-1}] &= [\mathbf{C}_p^{-1}]_n, & [\widetilde{\mathbf{b}}_e] &= [J^{-2/3}]_{n+1} [\mathbf{F}]_{n+1} [\widetilde{\mathbf{C}}_p^{-1}] [\mathbf{F}^\top]_{n+1} \\ \text{dev}[\widetilde{\boldsymbol{\tau}}_e] &= \mu \text{dev}[\widetilde{\mathbf{b}}_e], & \text{dev}[\widetilde{\boldsymbol{\tau}}] &= [J_\theta]_{n+1} \text{dev}[\widetilde{\boldsymbol{\tau}}_e] \\ [\widetilde{\mathbf{n}}] &= \frac{\text{dev}[\widetilde{\boldsymbol{\tau}}_e]}{\|\text{dev}[\widetilde{\boldsymbol{\tau}}_e]\|}, & [\widetilde{\mathbf{N}}] &= [\mathbf{F}^{-1}]_{n+1} [\widetilde{\mathbf{n}}] [\mathbf{F}^{-\top}]_{n+1} \\ [\widetilde{\boldsymbol{\varepsilon}}_p] &= [\boldsymbol{\varepsilon}_p]_n \\ [\widetilde{I}_1] &= \text{tr}\left([\widetilde{\mathbf{b}}_e]\right), & \bar{\mu} &= \frac{1}{3}\mu [J_\theta]_{n+1} [\widetilde{I}_1] \\ \Delta\lambda_p &= 0, & \zeta_0 &= \zeta_1 = \zeta_2 = \zeta_3 = \zeta_4 := 0 \end{aligned}$$

3. Check for plastic loading.

$$[\widetilde{f}_p] = \left\| \text{dev}[\widetilde{\boldsymbol{\tau}}_e] \right\| - \sqrt{\frac{2}{3}} \left( \sigma_0 + H [\widetilde{\boldsymbol{\varepsilon}}_p] \right)$$

IF  $[\widetilde{f}_p] \leq 0$ , set  $[\bullet]_{n+1} = [\widetilde{\bullet}]$  and proceed to 5 (elastic step).

ELSE, proceed to 4 (plastic step).

4. Perform return mapping and update the scaling parameters.

$$\begin{aligned} \Delta\lambda_p &:= \frac{(3/2)[\widetilde{f}_p]}{\mu[\widetilde{I}_1] + H} \\ \zeta_0 &:= \frac{\mu[\widetilde{I}_1]}{\left[ \mu[\widetilde{I}_1] + H \right]} \\ \zeta_1 &:= \frac{2\bar{\mu}\Delta\lambda_p}{\left\| \text{dev}[\widetilde{\boldsymbol{\tau}}] \right\|} \\ \zeta_2 &:= (1 - \zeta_0) \frac{2\Delta\lambda_p \left\| \text{dev}[\widetilde{\boldsymbol{\tau}}] \right\|}{3\bar{\mu}} \\ \zeta_3 &:= \zeta_0 - \zeta_1 + \zeta_2 \\ \zeta_4 &:= (\zeta_0 - \zeta_1) \frac{\left\| \text{dev}[\widetilde{\boldsymbol{\tau}}] \right\|}{\bar{\mu}} \end{aligned}$$

5. Compute tangents.

$$\begin{aligned} \mathbb{I}_{ijkl}^{\text{sym}} &\equiv \frac{1}{2} [\delta_{ik} \delta_{jl} + \delta_{il} \delta_{jk}] \\ [\widetilde{\mathbf{a}}]_{ijkl}^{\text{dev}} &\equiv 2\bar{\mu} \left[ \mathbb{I}_{ijkl}^{\text{sym}} - \frac{1}{3} \delta_{ij} \delta_{kl} \right] - \frac{2}{3} \left\| \text{dev}[\widetilde{\boldsymbol{\tau}}] \right\| \left[ [\widetilde{\mathbf{n}}]_{ij} \delta_{kl} + \delta_{ij} [\widetilde{\mathbf{n}}]_{kl} \right] \\ \mathbf{a}_{ijkl}^{\text{dev}} &\equiv [\widetilde{\mathbf{a}}]_{ijkl}^{\text{dev}} - \zeta_1 [\widetilde{\mathbf{a}}]_{ijkl}^{\text{dev}} - 2\bar{\mu} \zeta_3 [\widetilde{\mathbf{n}}]_{ij} [\widetilde{\mathbf{n}}]_{kl} - 2\bar{\mu} \zeta_4 [\widetilde{\mathbf{n}}]_{ij} \text{dev} \left[ [\widetilde{\mathbf{n}}]^2 \right]_{kl} \\ \mathbf{a}_{ijkl}^{\text{vol}} &\equiv [p]_{n+1} [J]_{n+1} [\delta_{ij} \delta_{kl} - 2\mathbb{I}_{ijkl}^{\text{sym}}] \\ \mathbf{a} &\equiv \mathbf{a}^{\text{dev}} + \mathbf{a}^{\text{vol}} \end{aligned}$$

## 6. Update the intermediate configuration and stress.

$$\begin{aligned}
 [\mathbf{C}_p^{-1}]_{n+1} &= [\widetilde{\mathbf{C}_p^{-1}}] - \frac{2}{3}\Delta\lambda_p \text{TR}\left([\widetilde{\mathbf{C}_p^{-1}}]\right) [\widetilde{\mathbf{N}}] \\
 [\widehat{\mathbf{b}}_e]_{n+1} &= [\mathbf{J}^{-2/3}]_{n+1} [\mathbf{F}]_{n+1} [\mathbf{C}_p^{-1}]_{n+1} [\mathbf{F}^\top]_{n+1} \\
 [\varepsilon_p]_{n+1} &= [\widetilde{\varepsilon}_p] + \sqrt{\frac{2}{3}}\Delta\lambda_p \\
 \text{dev}[\boldsymbol{\tau}]_{n+1} &= \text{dev}[\widetilde{\boldsymbol{\tau}}] - 2\bar{\mu}\Delta\lambda_p[\widetilde{\mathbf{n}}] \\
 [\boldsymbol{\tau}]_{n+1} &= \text{dev}[\boldsymbol{\tau}]_{n+1} + [p]_{n+1} [\mathbf{J}]_{n+1} \mathbf{1}
 \end{aligned}$$

We conclude by making a few remarks on the algorithm. First, the fields  $[\widetilde{\mathbf{u}}]_{n+1}$ ,  $[p]_{n+1}$ , and  $[\gamma]_{n+1}$  are *given* from the assumed increment of the Newton-Raphson algorithm. In addition,  $[\theta]_{n+1}$  is *given* by transfer from the chemo-thermal solver. Furthermore, all fields from the previous time step(s) are presumed resolved. Next, we note, due to the assumption of volume preserving plasticity, that  $\mathbf{C}_p$  and  $\widehat{\mathbf{C}}_p$  are interchangeable, and that the computation of  $\mathbf{a}^{\text{vol}}$  is independent of the plastic integration algorithm. Finally we note, since the scaling parameters are initialized to 0 in Step 2. of the algorithm, that  $\mathbf{a}^{\text{dev}}$  reduces simply to  $[\widetilde{\mathbf{a}}]^{\text{dev}}$  in the case of an elastic step.

### 4.3.5 High Performance Computing

The computational implementation is parallelized through the use of multithreading. This is done with the OpenMP application programming interface (API) which is a library of compiler directives and callable routines that extend C++ to utilize shared memory parallelism [17]. Figure 4.3 shows the result of a scaling analysis of the implementation. The percent decrease in total time and time for the generalized finite element (GFEM) routines are computed as  $|t - t_1|/t_1$  where  $t_1$  is the time for one (1) thread (no parallelism). We can see considerable speedup until 16 threads, after which the improvement in efficiency levels out (GFEM) or lessens (total time).

Upon further investigation, the lessening of the total time efficiency is due to the decrease in efficiency of the linear solver routines.

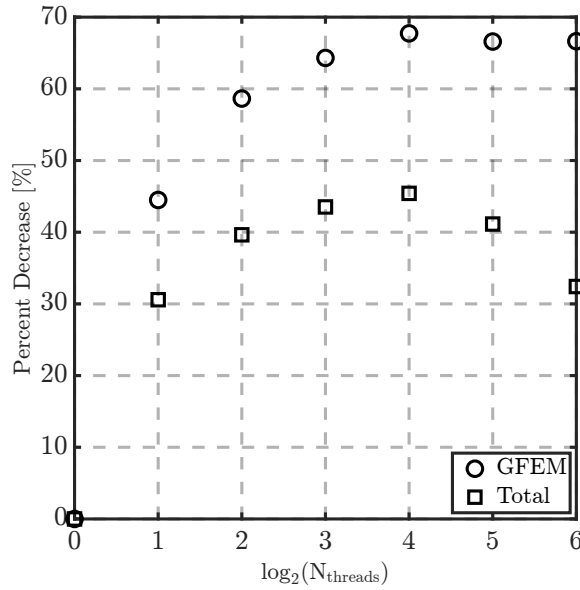


Figure 4.3. A plot of the percent decrease in computation time as a function of the number of threads for the generalized finite element routines (GFEM) and total time (GFEM, linear solvers, input, and output).

This suggests that special attention must be paid to thread number selection, especially when increasing the number of degrees of freedom and, hence, the resources required by the linear solvers. Furthermore, system architecture plays a significant role in the efficiency of the OpenMP implementation. Namely, the number of available processors influences, directly, the performance of the multithreading process.

## CHAPTER 5

### MODEL CALIBRATION

This chapter details this calibration of the model described in Chapters 2 and 4. This calibration is conducted using available experimental data. The simulations described in Chapters 6 and 7 make use of the material parameters determined from this calibration.

#### 5.1 Chemistry

For the chemical model, Weese et al. [97] measured the kinetics of the HMX  $\beta \rightarrow \delta$  phase transformation for heating rates of 1, 2, 5, and 10 [K/min]. They determined first order reaction parameters  $A = 2.000 \times 10^{48}$  [s<sup>-1</sup>] and  $E_a = 432.0$  [kJ/mol]. By substituting Eq. 3.3 into Eq. 2.9 and simplifying, we find that the evolution equation for the  $\delta$ -HMX mass fraction becomes  $\dot{y}_\delta = k_c(1 - y_\delta)$ . By approximating  $\dot{y}_\delta \approx \dot{\theta}(\partial y_\delta / \partial \theta)$  and treating  $\dot{\theta}$  as fixed, this becomes an ordinary differential equation in  $y_\delta$  and  $\theta$  with the initial condition  $y_\delta(\theta_0) = 0$ . The solution can be computed as

$$y_\delta(\theta) = 1 - \exp\left(-A\hat{A}[f_1(\theta) + f_2(\theta)]/\dot{\theta}\right), \quad (5.1)$$
$$f_1(\theta) \equiv \frac{E_a}{R_u} \text{Ei}\left(-\frac{E_a}{R_u\theta}\right), \quad f_2(\theta) \equiv \theta \exp\left(-\frac{E_a}{R_u\theta}\right),$$

where Ei is the exponential integral [30]. Substituting Eq. 5.1 into Eq. 3.4 yields function  $q_c(\theta)$  where, again,  $\dot{\theta}$  is treated as a fixed parameter. It is important to note that treating  $\dot{\theta}$  as fixed is valid *only* in the temperature regime considered for the DSC experiments in which the energy supplied by the DSC is used to traverse the reaction.

This is done since solution of the full model repeatedly for a wide swath of potential parameters, as would be necessary for a nonlinear least squares minimization process, would be computationally expensive. For other settings (e.g., those considered for the simulations described in Chapters 6 and 7),  $\dot{\theta}$  is determined by the physics. We perform a least squares fit of  $q_c(\theta)$  to the DSC heat release data for each heating rate. The corrective factor,  $\widehat{A}$ , is assumed to vary linearly as a function of temperature rate then calibrated as

$$\widehat{A}(\dot{\theta}) = 0.0451\dot{\theta} + 0.0088. \quad (5.2)$$

This calibration also yields heat of reaction,  $\Delta h^{\text{rxn}} = 44.87$  [kJ/kg]. Figure 5.1 shows the results of the calibration and Figure 5.2 shows the resultant  $y_\delta$  curves for each rate accompanied by the experimental data from [97]. One can see that the calibrated parameters capture the experimental data well, including the trough (i.e., the region around the minimum) of the heat curve, the temperature at which the minimum chemical heat is reached (see Figure 5.1), and the time to reaction (see Figure 5.2).

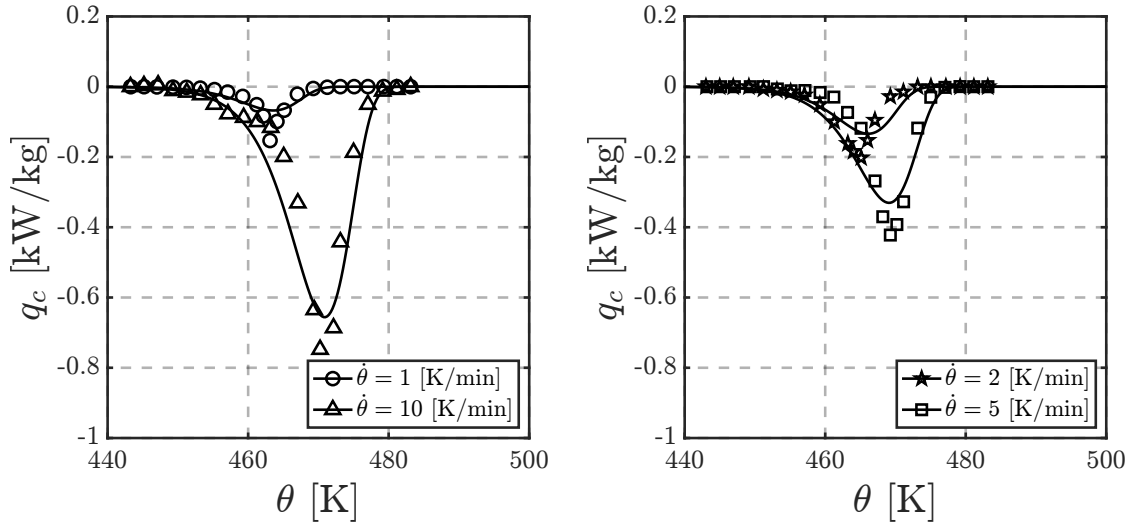


Figure 5.1. Calibration for the corrective factor,  $\hat{A}$ , and the enthalpy of reaction,  $\Delta h^{\text{rxn}}$  using the chemical heating,  $q_c$ . The markers indicate experimental data points, while the curves are plots of the model using the resultant calibrated parameters.

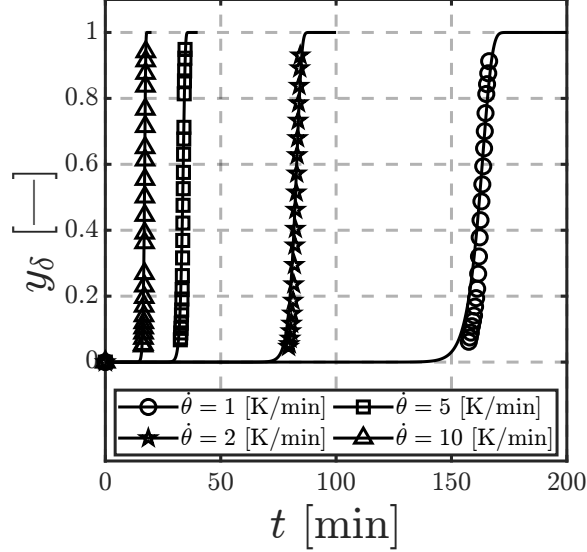


Figure 5.2. Plots of the model of the  $\delta$ -HMX mass fraction,  $y_\delta$ , given by Eq. 3.2 using the parameters given by the calibration (solid lines) along with experimental conversion data (markers) provided in [97].

## 5.2 Thermodynamics

For the thermo-mechanical model, Dobratz and Crawford [21] provide the densities, thermal conductivities, and reference heat capacities for HMX and Viton, as well as the CTE for Viton (the bonding matrix for the HMX based PBXs).

## 5.3 Mechanics

Weese and Burnham [96] performed experimental studies related to the dimensional changes of the  $\beta$  and  $\delta$  polymorphs of HMX. With this in mind, we capture the overall thermal expansion behavior of single crystal HMX by utilizing a model given by

$$\alpha(\theta) = \alpha_0 + \frac{\alpha_1 e^{-\omega(\theta-\theta_T)}}{[1 + e^{-\omega(\theta-\theta_T)}]^2}, \quad (5.3)$$

where  $\alpha_0$ ,  $\alpha_1$ ,  $\omega$ , and  $\theta_T$  are material parameters. The dimensional change of a long HMX specimen can be computed as

$$\Delta L = L_0 \int_{\theta_0}^{\theta} \alpha(\hat{\theta}) d\hat{\theta}, \quad (5.4)$$

where  $L_0$  is the initial length. Substituting Eq. 5.3 into Eq. 5.4 gives

$$\Delta L = L_0 \left[ \alpha_0 \theta + \frac{\alpha_1/\omega}{1 + e^{-\omega(\theta-\theta_T)}} - \left( \frac{\alpha_1/\omega}{1 + e^{-\omega(\theta_0-\theta_T)}} + \alpha_0 \theta_0 \right) \right]. \quad (5.5)$$

In view of Figure 5.3, which shows the results of the calibration of Eq. 5.5 to the experimental data, it should be noted that  $L\alpha_0$  is equal to the slope of the linear portion of the graph ( $340 \leq \theta \leq 460$  [K]),  $L\alpha_1/\omega$  is directly proportional to the magnitude of the jump in dimensional change during  $\beta \rightarrow \delta$  phase transformation ( $460 \leq \theta \leq 480$  [K]), and  $\theta_T$  is the approximate temperature at which the  $\beta \rightarrow \delta$  transformation occurs.  $\omega$  is a parameter that controls the sharpness of the transition curve. The experimental data provided in [96] corresponds to HMX expansion with not fully described porosity that leads to 17% sample volume changes. In order to compensate for this and better match the reported theoretical volume increase of 6.7%, we calibrate the CTE in two stages. First we calibrate the shape parameter,  $\omega$ , and the transition temperature,  $\theta_T$ , using the data in Figure 5.3. Next, we utilize the theoretical density values to correct  $\alpha_0$  and  $\alpha_1$  to match the theoretical volume change of 6.7%. The results of our CTE fit are summarized in Table 5.1. Figure 5.3(b) also includes a line indicating the value of the CTE for the Viton binder provided by Dobratz and Crawford [21]. It can be seen that the binder has a higher CTE than that of HMX except during the transition regime between approximately 459 [K] and 473 [K]. These points prove to be critical in the analysis of the PBX material response as is further discussed in Section 7.2.

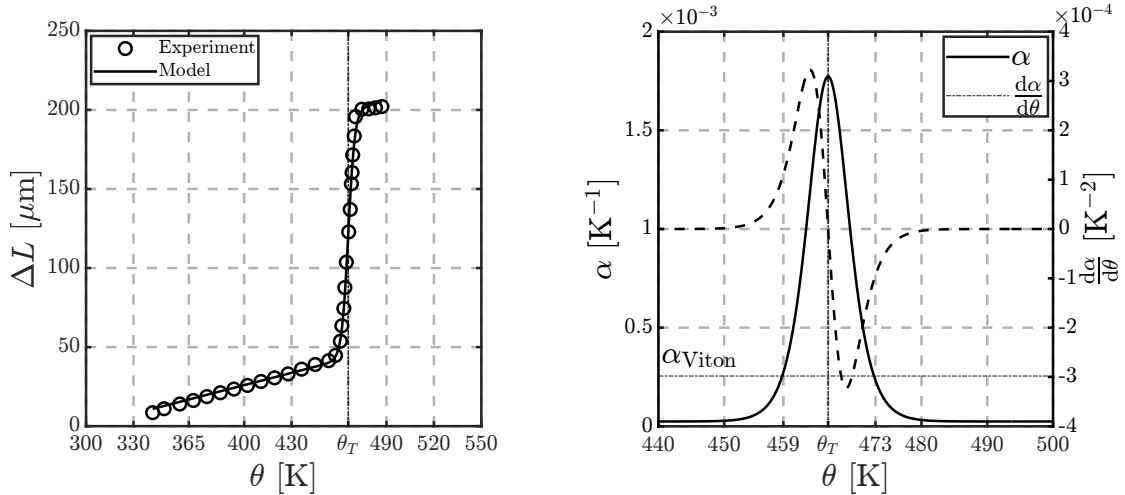


Figure 5.3. Calibration of the nonlinear CTE,  $\alpha$ , of HMX crystals using dimensional change,  $\Delta L$ , (left) and a plot of the resultant (reduced) CTE and its derivative (right).

We continue with the calibration of the elastoplastic properties. In this work, we model HMX as a hyperelastic solid. Rae et al. [67] measured the quasi-static compressive stress versus strain response of single crystals of  $\beta$ -HMX. The data provided in [67] are used to calibrate the initial elastic modulus, and Poisson ratio,  $\nu$ , using a nonlinear least squares fit. The temperature dependent data of the bulk modulus, Eq. 5.6, during the phase transition are not well understood. However, Levitas et al. [50] proposed the stress-induced virtual melting mechanism for HMX during the  $\beta \rightarrow \delta$  transition. This would suggest that the bulk modulus precipitously decreases. This softening behavior of elastic constants (e.g., the bulk modulus) during phase transition has been observed for polymer gels [36] as well as for quartz [3]. Therefore, we assume a similar response of HMX and use molecular dynamics simulations from Long and Chen [55] and Cui et al. [16] to guide the material HMX material calibration. In particular, In order to capture the behavior of the elastic moduli during

phase transition (see, for example, [23, 51]), we propose a model given as

$$\begin{aligned}\kappa(\theta) &= f_\kappa(\kappa_0 + \kappa'_0(\theta - \theta_0)) + (1 - f_\kappa)\kappa_1, \\ f_\kappa(\theta) &\equiv \frac{1}{2} \left[ 1 - \tanh\left(\frac{\theta - \theta_T - \phi_0}{2}\right) \right] \\ &\quad + \frac{1}{2} \left[ 1 + \tanh\left(\frac{\theta - \theta_T - \phi_1}{2}\right) \right],\end{aligned}\tag{5.6}$$

where  $\kappa_0$ ,  $\kappa'_0$ ,  $\kappa_1$ ,  $\phi_0$ , and  $\phi_1$  are material parameters. The resultant bulk modulus and its derivative is shown in Figure 5.4(a). The parameters are summarized in Table 5.2. The Poisson ratio is calibrated as a constant,  $\nu = 0.31$  [—] [21], and the shear modulus is computed using the canonical relation  $\mu(\theta) = 3\kappa(\theta)(1 - 2\nu)/(2(1 + \nu))$ .

Laurent et al. [48] investigated the thermo-mechanical behavior of Viton rubbers using tension and compression cyclic loadings and relaxation. We use the data provided in these works on the yield stress and hardening function at room temperature to calibrate the elastic moduli as well as the hardening modulus ( $H$ ) and yield stress ( $\sigma_0$ ) for the Viton matrix. We assume a constant Poisson ratio of  $\nu = 0.49$  (nearly incompressible). We use a nonlinear least squares fit between the experimental data and a numerical implementation of the model provided by Eqs. 3.7a and 3.9 for the binder. In Figure 5.4(b), we consider the engineering uniaxial strain given by the experimental data as  $\varepsilon = \Delta L/L$  which is used to compute the deformation gradient as

$$\mathbf{F}(\varepsilon) = \begin{bmatrix} 1 + \varepsilon & 0 & 0 \\ 0 & \sqrt{J/(1 + \varepsilon)} & 0 \\ 0 & 0 & \sqrt{J/(1 + \varepsilon)} \end{bmatrix},\tag{5.7}$$

where the volume change for uniaxial deformation is given as  $J(\varepsilon) = 1 + \varepsilon(1 - 2\nu)$ . This is then used to calculate the Cauchy stress given by Eq. 3.7a, assuming that  $\mathbf{b}_e = \mathbf{F} \mathbf{F}^\top$ . The elasto-plastic integration scheme used for Eq. 3.9 assuming isothermal deformation is described in detail by Simo and Ju [80]. The results of the calibration

for the Viton binder are depicted in Figure 5.4(b).

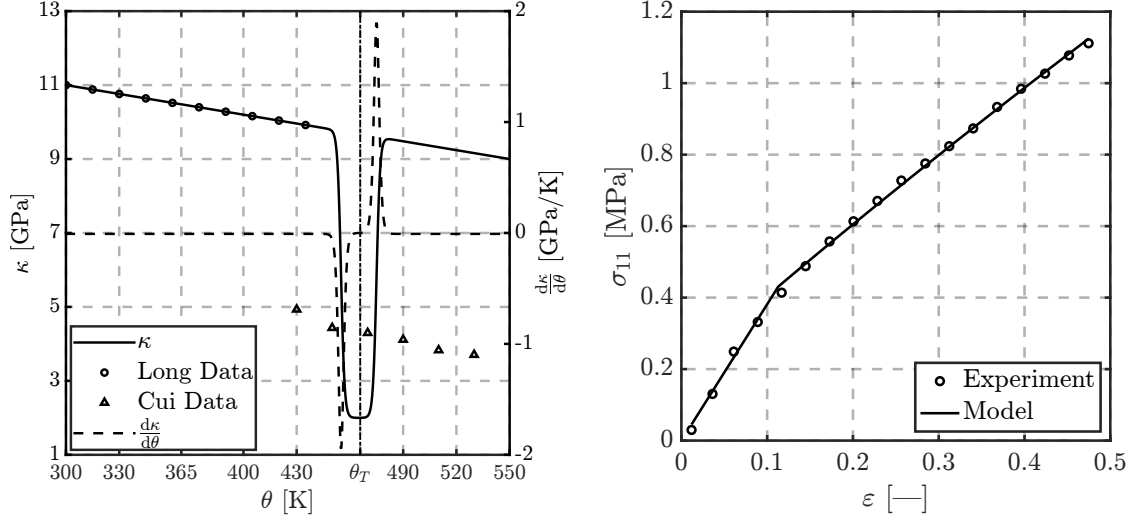


Figure 5.4. Calibration of the mechanical properties of HMX (left) and Viton (right). Here,  $\sigma$  and  $\varepsilon$  are uniaxial stress and strain, respectively, while  $\kappa$  is the bulk modulus.

#### 5.4 Summary of Material Properties

For the sake of convenience, the material data used in this work is presented in Table 5.3. In particular, Table 5.1 gives the results of the nonlinear CTE fit, Table 5.2, gives the results of the nonlinear bulk modulus fit, and Table 5.3 represents a concise summary of the results of the remaining calibrations described previously. These material properties are used for the simulations described in Chapter 6 and Chapter 7. All calibrated parameters are within the ranges of values reported in the literature.

TABLE 5.1

CALIBRATED PARAMETERS FOR THE CTE MODEL IN EQ. 5.3.

<b>CTE Calibration</b>	
$\alpha_0$ [K <sup>-1</sup> ]	$2.443 \times 10^{-5}$
$\alpha_1$ [K <sup>-1</sup> ]	0.007
$\theta_T$ [K]	465.8
$\omega$ [K <sup>-1</sup> ]	0.4794

TABLE 5.2

CALIBRATED PARAMETERS FOR THE BULK MODULUS MODEL  
IN EQ. 5.6.

<b>Bulk Modulus Calibration</b>	
$\kappa_0$ [MPa]	11000
$\kappa'_0$ [MPa·K <sup>-1</sup> ]	-8.000
$\kappa_1$ [MPa]	2000.0
$\phi_0$ [K]	-10.80
$\phi_1$ [K]	9.200

TABLE 5.3

SUMMARY OF MATERIAL PROPERTIES USED FOR THE PBX  
SIMULATIONS.

<b>Chemical Properties</b>		
<b>Property</b>	<b>HMX</b>	<b>Binder (Viton)</b>
Activation Energy $E_a$ [kJ/mol]	432.0	–
Arrhenius Const. $A$ [ $s^{-1}$ ]	$2.000 \times 10^{48}$	–
Heat of Reaction $\Delta h^{rxn}$ [kJ/kg]	44.87	–
Corrective Factor $\hat{A}$ [-]	Eq. 5.2	–
<b>Thermal Properties</b>		
Thermal Cond. $\Lambda$ [W/(m·K)]	0.5560	0.2260
(Ref.) Heat Capacity ${}^0c_p$ [J/(kg·K)]	1035	1464
(Ref.) Heat Capacity ${}^0c_v$ [J/(kg·K)]	1026	1458
<b>Mechanical Properties</b>		
(Ref.) Density $\rho_0$ [kg/m <sup>3</sup> ]	1910	1815
Bulk Mod. $\kappa$ [MPa]	Eq. 5.6	63.53
Poisson Ratio $\nu$ [-]	0.3100	0.4900
Yield Stress $\sigma_0$ [MPa]	–	0.4319
Isotropic Hardening Mod. $H$ [MPa]	–	4.336
Taylor-Quinney factor $f_{TQ}$ [-]	–	0.9000
CTE $\alpha$ [K <sup>-1</sup> ]	Eq. 5.3	$2.548 \times 10^{-4}$

## CHAPTER 6

### MODELING OF SINGLE CRYSTAL HMX

#### 6.1 Model Setting

For the numerical simulations, a 1 mm  $\times$  1 mm crystal of HMX is heated at the boundary,  $\Gamma$ , at a steady rate,  $\dot{\theta}_\Gamma$ , from an initial temperature of  $\theta_0 = 300$  [K]. We consider temperature rates of 1, 5, and 10 [K/min] and simulation times of 15000, 3000, and 1500 [s] to achieve a final temperature of 550 [K]. To provide well resolved results, we have performed a mesh verification and used an adaptive time stepping strategy as in [73, 86]. Figure 6.1 is a representative mesh convergence study performed using two dimensional bilinear quadrilateral shape functions. The “true” solution is taken to be the finite element interpolation computed using a mesh 10 times more refined than that of the smallest mesh used in the study. Here, the error measure is the standard  $L_2$  norm used.

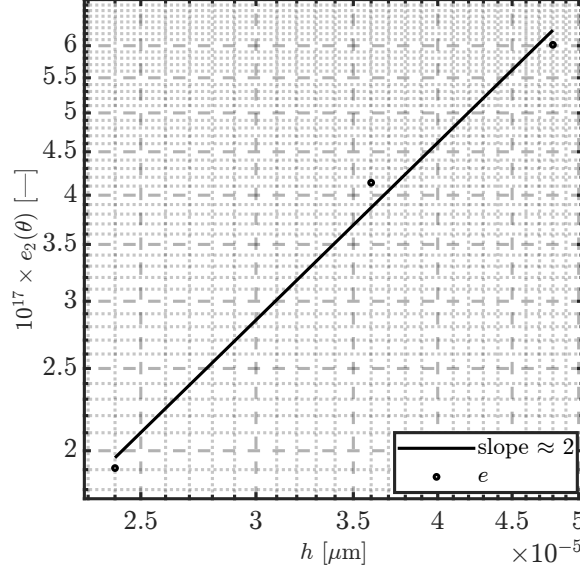


Figure 6.1. A log-log plot of the  $L_2$  error in temperature,  $\theta$ , computed in a self convergence study.

We can also investigate the length and time scales associated with the chemical species. Figure 6.2 shows snapshots from a quasi-linear simulation of a long HMX specimen. In Figure 6.2(a), we can see from the profile of the  $\delta$  phase mass fraction along the spatial dimension that the reaction zone thickness is  $\Delta_{\text{rxn}} \approx 7$  [mm]. Similarly, by looking at the  $y_\delta$  profile at different points in time, we can estimate the wave propagation speed to be roughly  $\Delta x / \Delta t \approx 0.0111$  [mm/s].

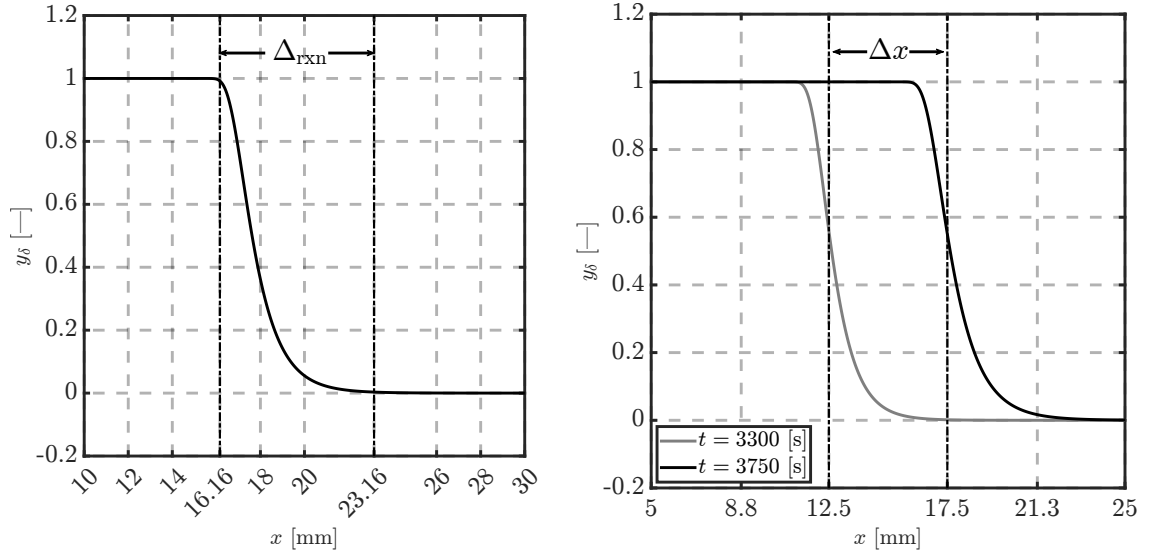


Figure 6.2. (left) A plot showing how the reaction zone thickness,  $\Delta_{\text{rxn}}$ , is approximated and (right) a plot showing how the wave speed is approximated.

For the adaptive time stepping scheme, Eq. 4.13, the actual values for  $\Delta t_{\text{max}}$  are 100, 20, and 10 [s] for the 1, 5, and 10 [K/min] heating rates, respectively. For  $\Delta t_{\text{min}}$ , the actual values are 10, 2, and 1 [s] for the 1, 5, and 10 [K/min] heating rates, respectively. For the staggering scheme described in Section 4.3.2, between 5 and 16 subcycles are required at each time step to achieve full system convergence. Figure 6.3 is a diagram of the computational domain. The associated mesh consists of 10,000 bilinear quadrilateral finite elements and 10,201 nodes.

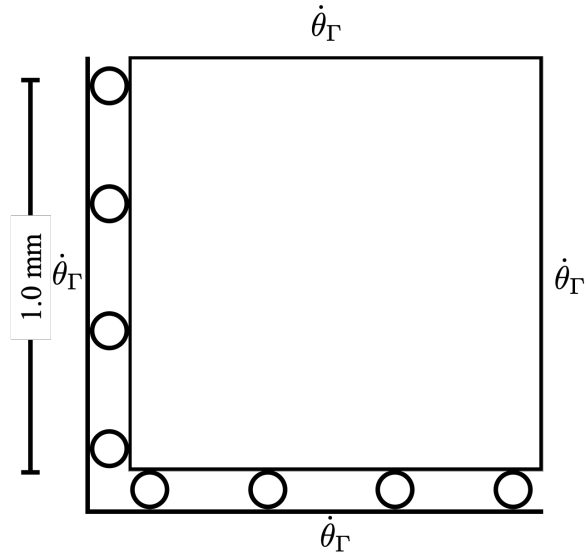


Figure 6.3. Diagram of the HMX single crystal computational domain. Also included are the computational thermal and mechanical boundary conditions. The temperature rate at the boundaries,  $\dot{\theta}_\Gamma$ , is one of 1, 5, or 10 [K/min].

## 6.2 Simulation Results

Figure 6.4 shows that our model predicts  $\approx 6.4\%$  average volume change computed as  $\Delta V/V_0 = J - 1$ , which compares favorably to the theoretical estimate of  $6.7\%$  [96].

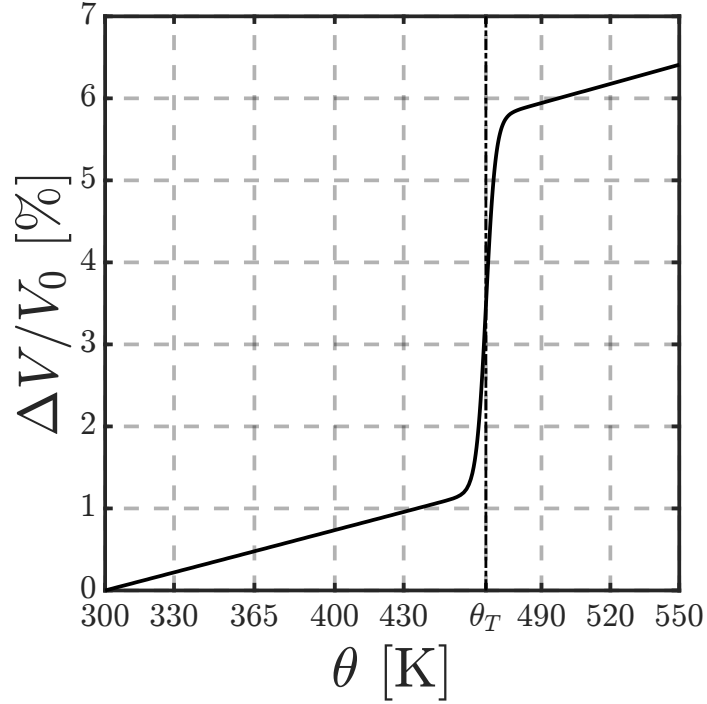


Figure 6.4. A plot of the percent change of the sample volume as a function of boundary temperature. Here,  $\Delta V/V_0$  refers to the change in volume of with respect to initial volume  $V_0$ . Compare to the dimensional change of the first heating cycle in Fig. 2 of [96].

Figure 6.5 depicts the axial components of the Cauchy stress tensor. As prescribed by the generalized plane strain condition, we can see that the normal stress components,  $\sigma_{11}$ ,  $\sigma_{22}$ , and  $\sigma_{33}$ , are nearly identical in behavior and magnitude (i.e., a virtually isotropic stress response of the material).

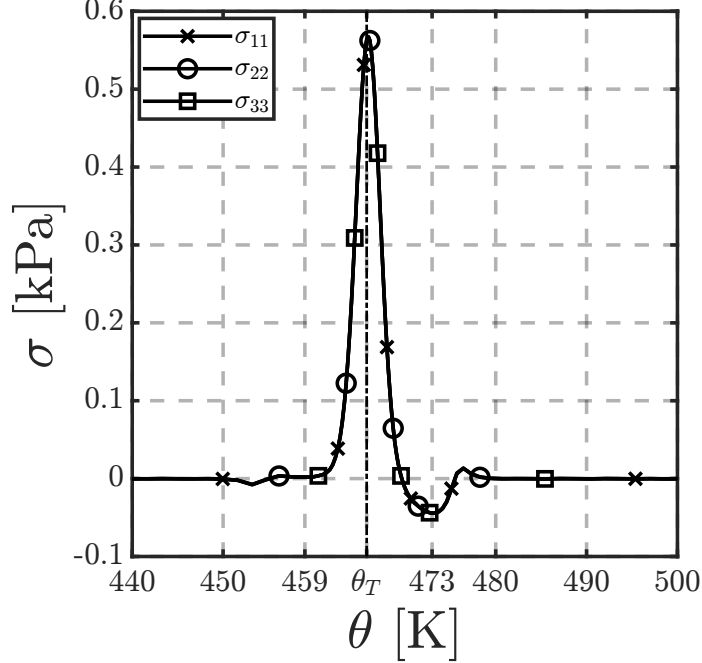


Figure 6.5. A plot of the axial Cauchy stress components showing virtually isotropic response.

Figure 6.6(a) shows the specific heats at constant elastic strains,  $c_p$ , and volume,  $c_v$ , averaged over the computational cell. We observe large changes in magnitude for both specific heats (i.e.,  $c_p$  will increase to  $\approx 14840$  [J/(kg·K)] and  $c_v$  will decrease to  $\approx 528$  [J/(kg·K)]). In light of Eqs. 2.33 and 2.35, the model predicts that the highly nonlinear  $\alpha(\theta)$ ,  $\kappa(\theta)$ , and their derivatives (see Figure 5.3(b) and Figure 5.4(a)) play a large role and compete in a highly nonlinear fashion. Furthermore, we observe a rapid temperature rate decrease and subsequent increase due to the nonlinearity of specific heats (see Figure 6.6(b)). However, the overall temperature rate variations with respect to the boundary heating rate,  $\dot{\theta}_\Gamma$ , are small in part due to the crystal size. This is a surprising result not observed for HMX that requires a careful analysis. First, we note that experimental results on specific heat of HMX often consider

individual phases separately [34, 44]. Moreover, measurements are often performed at relatively large temperature intervals potentially under-resolving the transition that occurs over a narrow temperature range. Furthermore, spikes in DSC traces for HMX have been observed [44]. Levitas et al. [50] estimated that the elastic energy relaxed during the stress-induced virtual melting is  $\Delta h \sim 30649$  [J/kg]. Considering the transition window of  $\Delta\theta \sim 5.358$  [K] as shown in Figure 6.6(a) (i.e., computed as an average transition temperature interval over the  $c_p$  profile), we estimate change of the specific heat during the stress-induced virtual melting as  $\Delta c_p = \Delta h / \Delta\theta \sim 5720.2$  [J/(kg·K)]. This value is smaller than our predictions, but we point to large material data sensitivity of  $\alpha(\theta)$  and  $\kappa(\theta)$ . Second, we note that nonlinear CTEs are common in phase transitioning materials [6, 9, 68, 71] and that the  $c_p$  profile in Figure 6.6(a) is similar to DSC measurements on geopolymer concrete [13]. Therefore, the nonlinearity of  $c_p$  as predicted by our model is plausible.

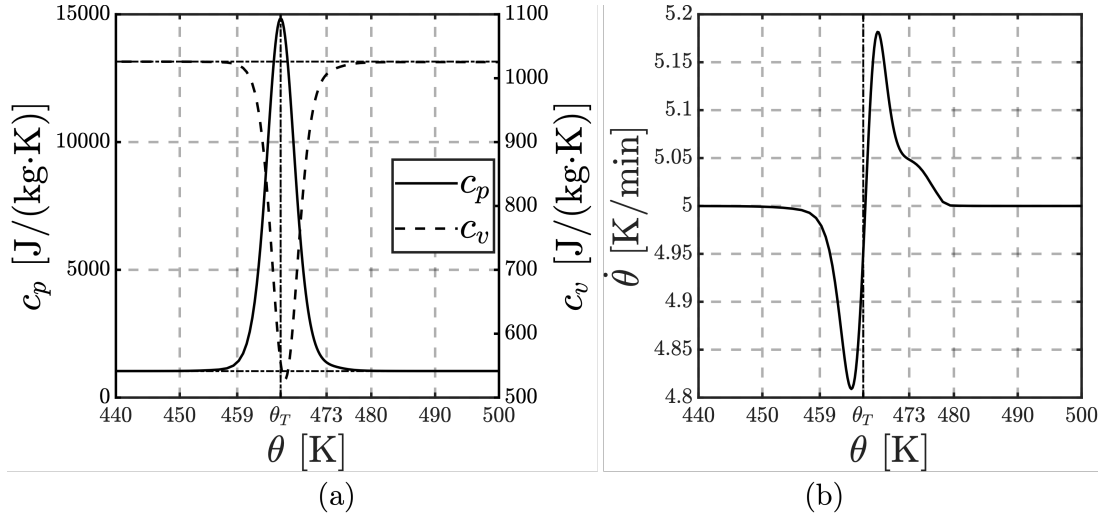


Figure 6.6. (a) Specific heats at constant pressure and volume as functions of temperature. Horizontal dotted lines indicate the respective reference quantities  ${}^0c_p$  and  ${}^0c_v$ . (b) The temperature rate as a function of average cell temperature. Both results are from the simulation with 5 [K/min] boundary temperature rate.

We also include contour plots of the specific heat at constant pressure,  $c_p$ , and constant volume,  $c_v$ , shown in Figure 6.7(a) and Figure 6.7(b), respectively. The plots are depicted at the point in the simulation where the boundary temperature,  $\theta_\Gamma$ , approximately equals the  $\beta \rightarrow \delta$  CTE transition temperature,  $\theta_T$ .

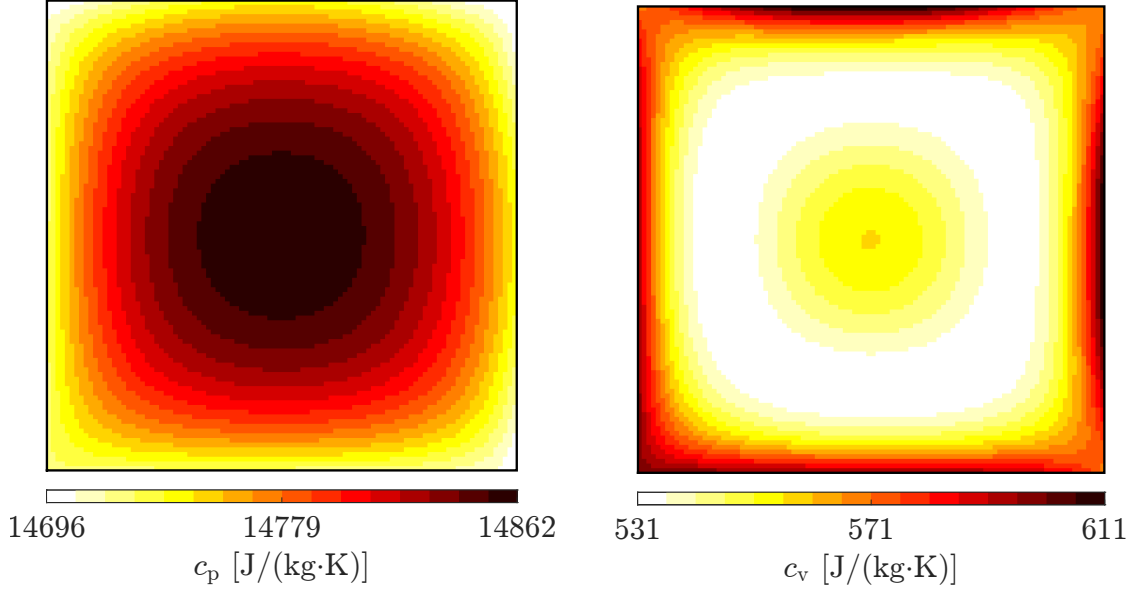


Figure 6.7. (a) A contour plot of specific heat at constant pressure,  $c_p$ . (b) A contour plot of specific heat at constant volume,  $c_v$ . Both plots are at the point in the simulation where the boundary temperature,  $\theta_\Gamma$ , approximately equals the transition temperature,  $\theta_T$ .

Finally, we note some model limitations. Specifically, the Helmholtz free energy, especially its thermal part in Eq. 2.15, is not well known. Moreover, we note the lack of pressure dependency and reaction reversibility [42], as well as crystal anisotropy, and pressure and temperature dependency of elastic parameters, especially  $\kappa$  [72].

We continue by deriving a novel estimate for the critical temperature at which the chemical heating rate occurs. Substituting the  $y_\delta$  approximation, Eq. 5.1, into the chemical heating rate, Eq. 2.34a, setting the derivative of the resulting  $q_c$  with respect to  $\theta$  equal to 0, then solving for  $\theta$ , we find

$$\theta_c(\dot{\theta}) \approx \frac{E_a/R_u}{2W \left( \sqrt{\left( \frac{A\hat{A}E_a}{4\theta R_u} \right)} \right)}, \quad (6.1)$$

where  $W$  is the  $W$  Lambert function [47]. For our parameters,  $\theta_c$  tends to 474.2 [K] as  $\dot{\theta}$  tends to infinity. In Figure 6.8(a), we plot the chemical heating rate averaged over the computational cell for each boundary temperature rate. For each  $\dot{\theta}_\Gamma$ , we note the associated critical temperature,  $\theta_c$ , at which the chemical heating rate extremum occurs. We mark these  $(\dot{\theta}_\Gamma, \theta_c)$  coordinate pairs in Figure 6.8(a). In Figure 6.8(b), we plot the  $(\dot{\theta}_\Gamma, \theta_c)$  coordinate pairs alongside the predictions from Eq. 6.1. We note the remarkable agreement between the critical temperatures from simulations and those predicted by this equation. Furthermore, this provides a solution verification of the computational results.

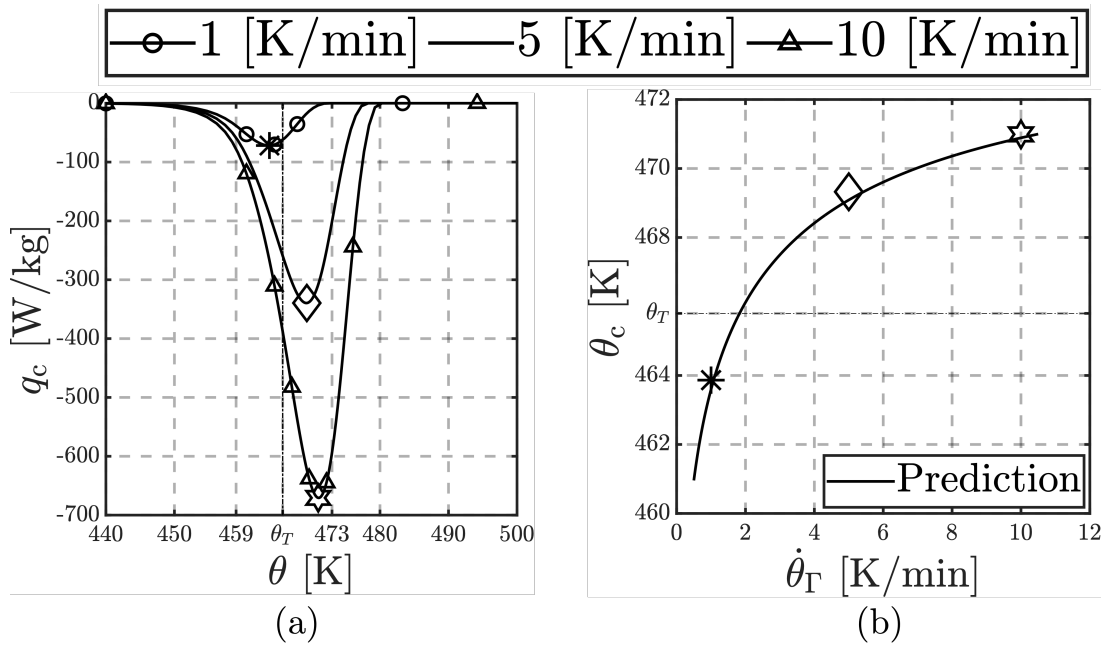


Figure 6.8. (a) Chemical heating rate as a function of temperature and (b) critical temperature for the chemical heating rate as a function of boundary heating rate.

We also include contour plots of the chemical and elastic heating terms shown in Figure 6.9(a) and Figure 6.9(b), respectively. The plots are depicted at the point in the simulation where the boundary temperature,  $\theta_\Gamma$ , approximately equals the  $\beta \rightarrow \delta$  CTE transition temperature,  $\theta_T$ .

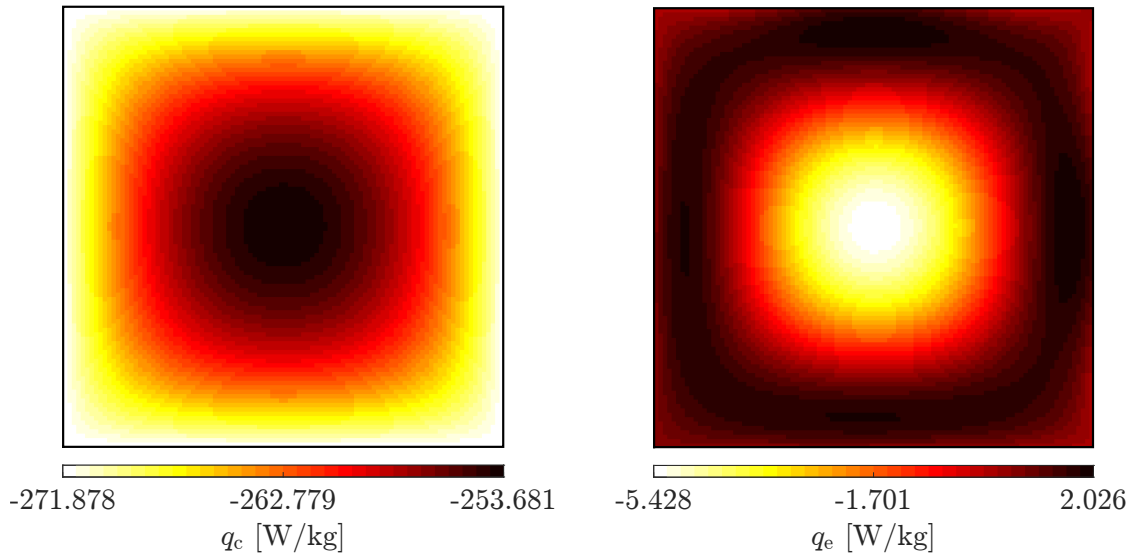


Figure 6.9. (a) A contour plot of the chemical heating. (b) A contour plot of the elastic heating. Both plots are at the point in the simulation where the boundary temperature,  $\theta_\Gamma$ , approximately equals the transition temperature,  $\theta_T$ .

## CHAPTER 7

### MODELING OF HMX BASED PBXS

#### 7.1 Model Setting

We are interested in the behavior of heterogeneous energetic materials under thermal and mechanical loading conditions. Our objective is to simulate the CTM response for the HMX  $\beta \rightarrow \delta$  phase transition for energetic crystals plastically bounded in a Viton rubber matrix. Due to the complexity of the multi-physics model, we make an effort to generate representative unit cells with appropriate boundary conditions to best approximate the material behavior such as in cook-off studies [19].

The representative unit cells are generated with microstructures such that i.) the particle sizes follow a trimodal distribution (radii equal to 24.4, 107, and 295  $\mu\text{m}$  with probabilities nearing 11, 73, and 16% respectively) derived from morphologies presented by Skidmore et al. [81] on coarse (unpressed) HMX, ii.) the overall HMX volume fraction within the unit cell is approximately one of 40, 50, or 60%, and iii.) the unit cell size selection is informed by the minimum representative volume element sizes for heterogeneous materials [45][54].

In particular, Skidmore et al. [81] used laser diffraction methods to report on the morphology of “as received” HMX powders. The particle size distribution for course class HMX provided therein is used to determine a trimodal particle size distribution when generating the microstructures for the CTM simulations. The data for the volume percent as a function of the  $\log_{10}$  of the particle radius is fit with a Gaussian

curve,  $\Phi(\xi)$  where  $\xi \equiv \log_{10}(r)$ , then scaled as

$$\phi(\xi) \equiv \frac{\Phi(\xi)}{\int_{\xi} \Phi(\xi) d\xi}, \quad (7.1)$$

such that  $\int_{\xi} \phi(\xi) d\xi = 1$ . We thereby treat  $\phi$  as a probability density function (PDF) for particle radius. Due to the computational cost associated with generating the finite element meshes required to accurately model particles with radii less than  $1 \mu\text{m}$  within the relevant geometries, we neglect the region defined by  $-1 < \xi < 1$ . These small particles are often lumped with a binder to create a homogeneous blend (i.e., a “dirty binder”) [33]. However, since the properties of the blend are not fully known we treat the blend as a single material (i.e., inert Viton). The remaining domain,  $\xi \in (1, 3)$ , is split into three modes defined by  $\xi \in (1, \frac{5}{3})$ ,  $\xi \in (\frac{5}{3}, \frac{7}{3})$ , and  $\xi \in (\frac{7}{3}, 3)$  and assigned an expectation value,  $E(\xi_i \leq \xi \leq \xi_f)$ , of  $\xi$  within the interval  $(\xi_i, \xi_f)$  calculated in the standard way for a continuous PDF.

$$E(\xi_i \leq \xi \leq \xi_f) = \frac{\int_{\xi_i}^{\xi_f} \xi \phi(\xi) d\xi}{\int_{\xi_i}^{\xi_f} \phi(\xi) d\xi} \quad (7.2)$$

The associated probability  $P(\xi_i \leq \xi \leq \xi_f \mid \xi > 1)$ , which is the probability that  $\xi \in (\xi_i, \xi_f)$  given that  $\xi \notin (-1, 1)$ , is also computed in the standard way for a continuous PDF.

$$P(\xi_i \leq \xi \leq \xi_f \mid \xi > 1) = \frac{\int_{\xi_i}^{\xi_f} \phi(\xi) d\xi}{1 - \int_{-1}^1 \phi(\xi) d\xi}. \quad (7.3)$$

The expectation values of  $\xi$  are then use to compute the expectation values of  $r$  as  $E(r) = 10^{E(\xi)}$ . Finally, we generate particles following these expectation values and probabilities and distribute them, using random sequential addition (RSA) [90],

throughout a computational domain with side length  $L > 5r_{\max}$  as informed by [45, 54] for the volume fractions of interest. Figure 7.1 details the results of these computations for each of the three modes. For the purpose of gathering statistics, five microstructures are generated for each volume fraction for a total of 15 different microstructures.

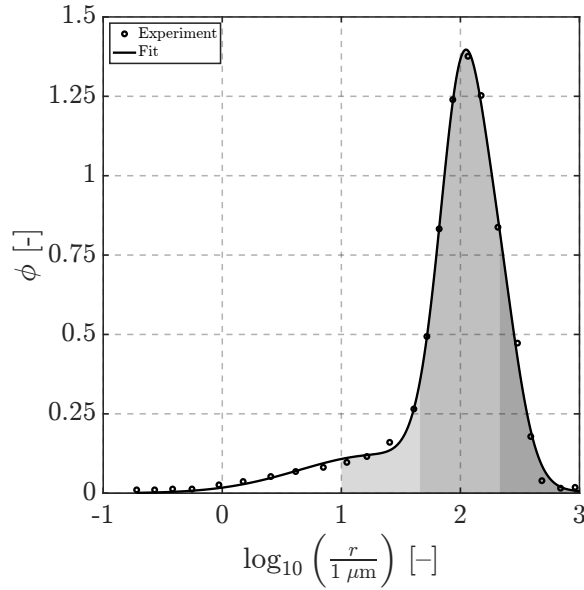


Figure 7.1. Data and fit to determine trimodal particle size distribution. The experimental distribution data is provided by Skidmore et al. [81] in terms of volume percent as a function of particle diameter. The calculated expectation values of each shaded region, from left to right, are  $E_1(r) = 24.4 [\mu\text{m}]$ ,  $E_2(r) = 107 [\mu\text{m}]$ , and  $E_3(r) = 295 [\mu\text{m}]$  with associated probabilities  $P_1 = 11\%$ ,  $P_2 = 73\%$ , and  $P_3 = 16\%$ , respectively.

Figure 7.2 shows an example of one of the generated microstructures for a volume fraction of approximately 50% overlaid by the finite element mesh used for this particular realization. The unit cell in Figure 7.2 consists of 34,859 quadratic triangle

finite elements and 70,276 nodes. Similar mesh densities are used for all cells.

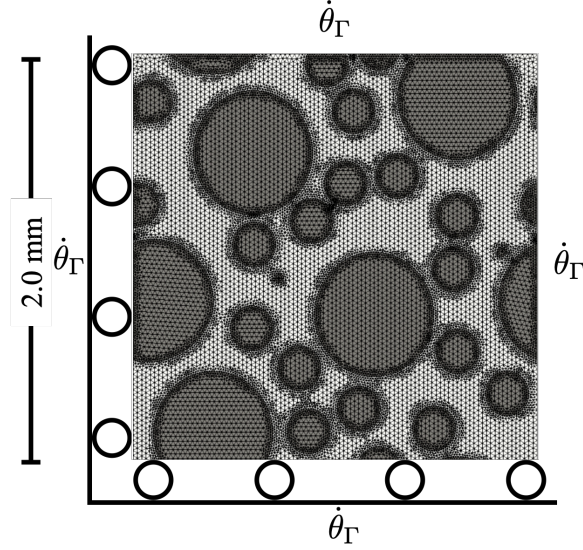


Figure 7.2. One microstructure for a volume fraction of 50%. Each sample contains randomly placed HMX particles following the trimodal distribution, within a domain of size  $4.0 \text{ mm}^2$ . Also included are the computational thermal and mechanical boundary conditions and the finite element mesh. The temperature rate  $\dot{\theta}_\Gamma$  at the boundaries is one of 1, 5, or 10 [K/min].

Figure 7.2 also shows roller mechanical boundary conditions and Dirichlet thermal boundary conditions. Specifically, the cell boundary is heated at a steady rate,  $\dot{\theta}$ , from a global initial temperature of  $\theta_0 = 300 \text{ [K]}$ . Heating rates of 1, 5, and 10 [K/min] as considered in the experimentation done by Weese et al. [97] are used in an effort to model thermal cook-off conditions. For the adaptive time stepping scheme, Eq. 4.13, the actual values for  $\Delta t_{\max}$  are 100, 20, and 10 [s] for the 1, 5, and 10 [K/min] heating rates, respectively. For  $\Delta t_{\min}$ , the actual values are 10, 2, and 1 [s] for the 1, 5, and 10 [K/min] heating rates, respectively. For the staggering scheme

described in Section 4.3.2, between 8 and 17 subcycles are required at each time step to achieve full system convergence. Total simulation times of 15000, 3000, and 1500 [s] are used for the 1, 5, and 10 [K/min] heating rates, respectively, to achieve a final temperature of 550 [K]. This final temperature is sufficient to bring the phase conversion to completion. Furthermore, these heating profiles allow for the highly nonlinear CTE and associated fields to fully develop in the material sample.

## 7.2 Simulation Results

In this section, we present the results of the CTM simulations. To illustrate the various fields, we select a representative cell with a 50% particle volume fraction and a boundary heating rate of 5 [K/min]. In order to ensure the quality of the numerical results, we performed solution verification by comparing predictions from simulations using nominal mesh sizes of 0.012, 0.024, and 0.048 [mm]. We concluded that a nominal mesh size of 0.024 [mm] was sufficient for our modeling purposes. Section 7.2.1 discusses the effect of particle volume fraction on the CTM response, and Section 7.2.2 discusses the effect of boundary heating rate on the CTM response.

We begin with contour plots of specific heat at constant pressure,  $c_p$ , and constant volume,  $c_v$ , shown in Figure 7.3(a) and Figure 7.3(b), respectively. The plots are depicted at the point in the simulation where the boundary temperature,  $\theta_T$ , approximately equals the  $\beta \rightarrow \delta$  CTE transition temperature,  $\theta_T$ . The spatial heterogeneity of the specific heats (see Eqs. 2.35 and 3.6), especially within the particles, is evident. This heterogeneity is largely the result of small variations in the temperature which lead to relatively large variations in the CTE and its derivative (see Figure 5.3(b)). The heterogeneity of the specific heat can also be attributed to variations in pressure throughout the domain. We will return to this point later. Interestingly, Figure 7.3(a) shows  $c_p$  values significantly larger than  ${}^0c_p$  while Figure 7.3(b) shows  $c_v$  values significantly smaller than  ${}^0c_v$ . This exotic material response of HMX was

previously discussed in Section 6.2 and is further examined in the context of PBXs in Section 7.2.1.

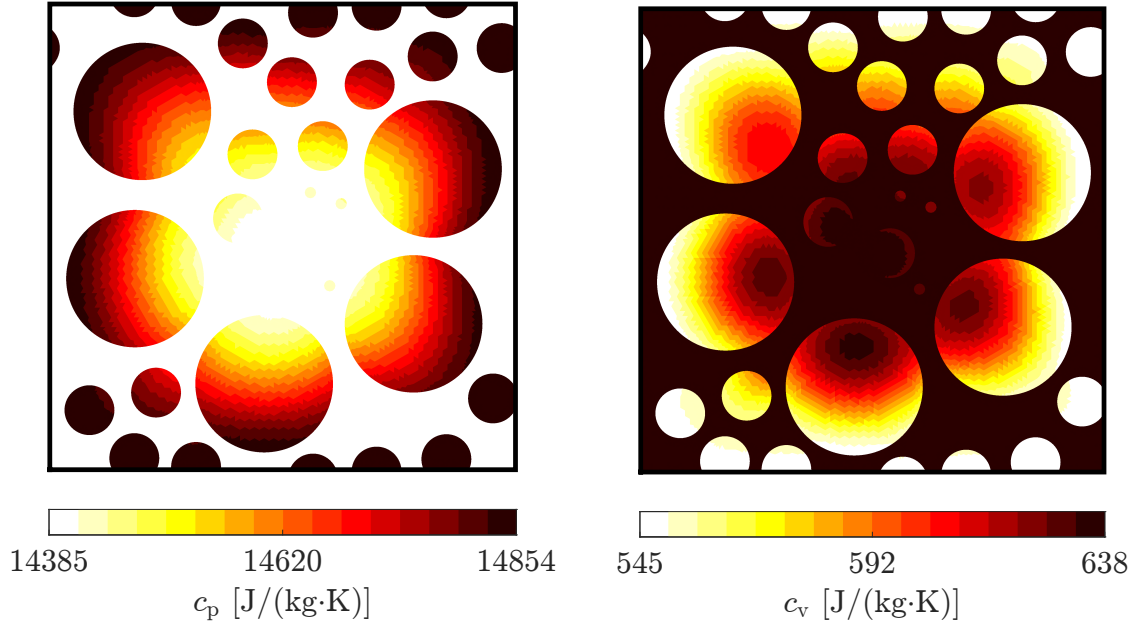


Figure 7.3. (a) A contour plot of specific heat at constant pressure,  $c_p$ . The color scale is adjusted to the range of values observed within the particles; the actual minimum  $c_p$  observed is 1464 [J/(kg·K)], the reference value for the matrix. (b) A contour plot of specific heat at constant volume,  $c_v$ . Again, the color scale is adjusted to the range of values observed within the particles; in this case, the actual maximum  $c_v$  observed is 1458 [J/(kg·K)], the reference value for the matrix. Both plots are at the point in the simulation where the boundary temperature,  $\theta_\Gamma$ , approximately equals the transition temperature,  $\theta_T$ .

We continue with a contour plot of the accumulated equivalent plastic strain,  $\varepsilon_p$ , shown at the end of the simulation where the boundary temperature is 550 [K] (see Figure 7.4(a)). It can be seen that the majority of plastic shearing occurs within

the matrix in regions of high stress concentration (i.e., between particles). Willey et al. [100] performed X-ray microtomography before and after heating HMX-based samples through the  $\beta \rightarrow \delta$  phase transition and showed the extensive microstructural damage resulting from the solid-state phase transition. The shear bands predicted by our simulations in Figure 7.4(a) compare favorably to the crack patterns observed in Fig. 5 of that work [100]. We also include a plot of the percent change in volume of the sample, particles, and matrix as a function of boundary temperature in Figure 7.4(b). Here,  $\Delta V_r/V_{0,r}$  refers to the change in volume of region  $r$  with respect to initial region volume  $V_{0,r}$ . We see that, initially, the sample undergoes quasi-linear thermal expansion. Prior to transition onset, the expansion is dominated by that of the matrix due to its larger CTE (see Table 5.3). During the  $\beta \rightarrow \delta$  transition, the CTE of HMX spikes (see Figure 5.3(b)) which causes a rapid volumetric expansion of the particles and, thereby, the sample. After the transition is complete, sample expansion is again dominated by the quasi-linear expansion of the matrix. The dimensional changes predicted for the particles (i.e.,  $\sim 6.7\%$  volume increase) compare favorably to the theoretical values presented in Fig. 5 by Weese and Burnham [96]. One should note that in PBXs with more realistic particle volume fractions (e.g., 85% HMX loading), the overall percent volume change tends to that of HMX. Shortly after the  $\beta \rightarrow \delta$  phase transition (at approximately 490 [K]),  $\Delta V/V_0 \approx \phi_p \times 6\% + (1 - \phi_p) \times 15\%$  for particle volume fraction  $\phi_p$ . For example, for the aforementioned  $\phi_p = 85\%$ ,  $\Delta V/V_0 \approx 7.35\%$ . This is, again, close to experiments. As previously indicated, we neglect the formation of voids within the particles and matrix.

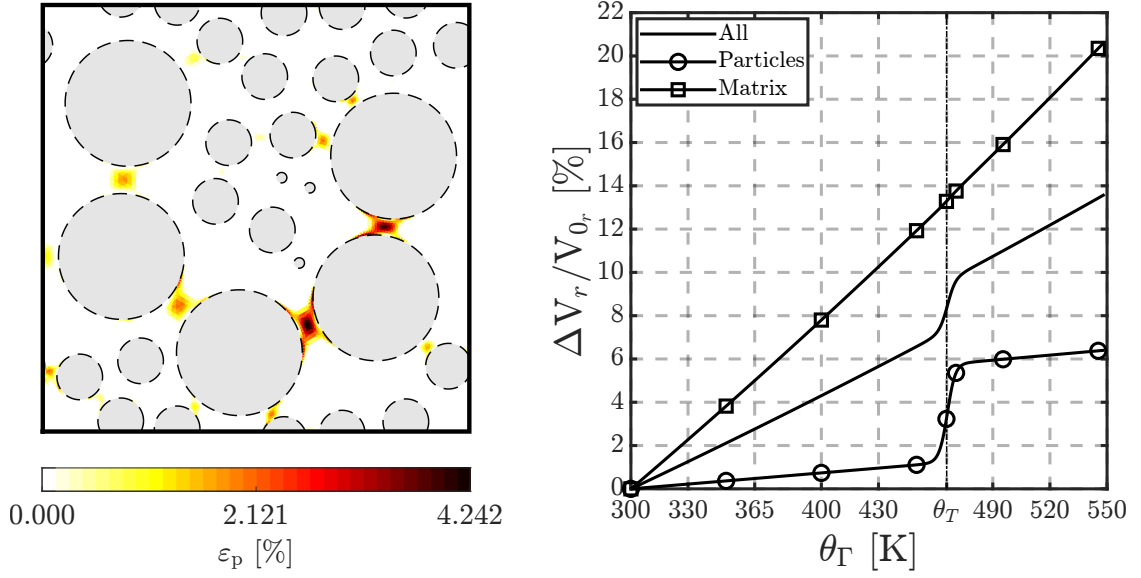


Figure 7.4. (a) A contour plot of equivalent plastic strain,  $\varepsilon_p$ , at the end of the simulation where the boundary temperature is approximately 550 [K]. Compare the shear bands above to the crack profiles in Fig. 5 of reference [100]. (b) A plot of the percent change of the sample volume as a function of boundary temperature. Here,  $\Delta V_r/V_{0_r}$  refers to the change in volume of region  $r$  with respect to initial region volume  $V_{0_r}$ . Compare to the dimensional change of the first heating cycle in Fig. 2 [96].

Throughout the remainder of this paper, we define volumetric and ensemble averages of the relevant quantities as

$$\langle \bullet \rangle_r^n = \frac{1}{\Omega_{0_r}^n} \int_{\Omega_{0_r}^n} (\bullet) d\Omega_{0_r}^n, \quad (7.4a)$$

$$\widehat{\langle \bullet \rangle}_r = \frac{1}{N} \sum_{n=1}^N \langle \bullet \rangle_r^n, \quad (7.4b)$$

$$\Omega_{0_r}^n = \int_{\Omega_{0_r}^n} d\Omega_{0_r}^n, \quad (7.4c)$$

where  $r$  indicates the domain of interest;  $r = p$  indicates the particles,  $r = m$  indicates

the matrix, and no subscript indicates the entire cell (i.e., overall cell response). Here,  $n$  indicates a given realization, where  $N$  is the total number of realizations included in the average for a given particle volume fraction at a given heating rate. A total of  $N = 5$  realizations are used for each particle volume fraction.

Figure 7.5(a) shows a contour plot of the pressure experienced throughout the domain, again near the point in the simulation where the boundary temperature,  $\theta_\Gamma$ , approximately equals the transition temperature,  $\theta_T$ . It can be seen that the pressure experiences large variations throughout the computational domain. As mentioned previously, this greatly impacts  $c_p$  and  $c_v$  (see Eqs. 2.35 and 3.6 and Figure 7.3). Figure 7.5(b) depicts the average of the axial components of the Cauchy stress tensor. As prescribed by the generalized plane strain condition, we can see that the normal stress components,  $\sigma_{11}$ ,  $\sigma_{22}$ , and  $\sigma_{33}$ , are nearly identical in behavior and magnitude (i.e., a virtually isotropic stress response of the material). These results are mirrored throughout all computations.

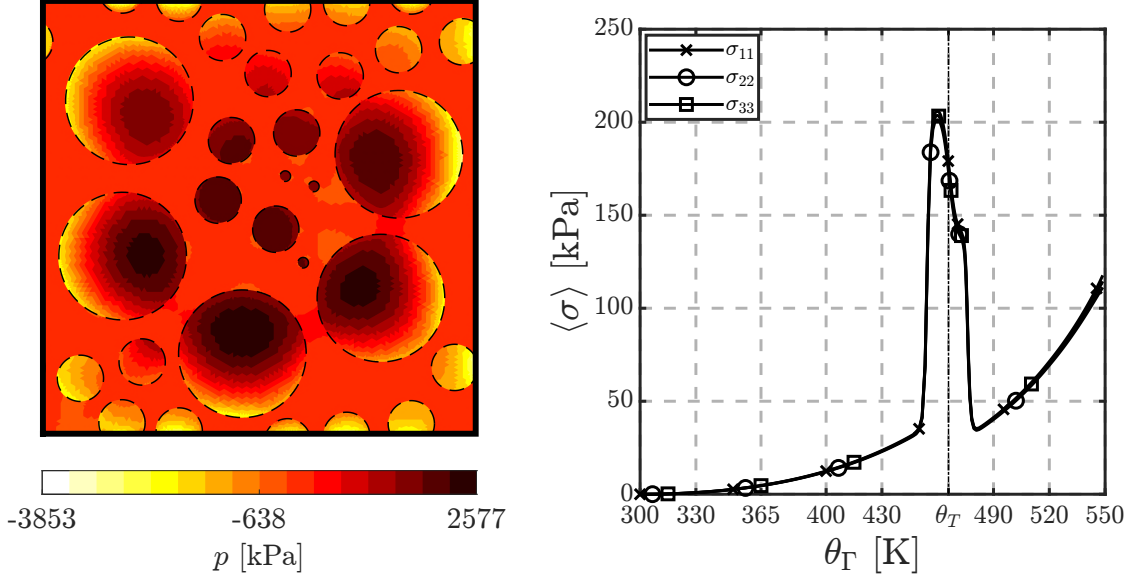


Figure 7.5. (a) A contour plot of the pressure experienced by the representative sample at the point in the simulation where the boundary temperature,  $\theta_\Gamma$ , approximately equals the transition temperature,  $\theta_T$ . (b) A plot of the axial Cauchy stress components for the representative cell showing virtually isotropic response.

We continue by analyzing the average heating rates experienced within the domain. In Figure 7.6 it can be seen that the chemical heating rate extremum does not occur at the CTE transition temperature,  $\theta_T$ . This is discussed further in Section 7.2.2. Note that the chemical heating rate is negative since the  $\beta \rightarrow \delta$  transition is endothermic. Furthermore, the majority of elastic heating occurs within the transition regime, specifically between 459 [K] and 473 [K]. As mentioned in Section 5.3, these are the temperatures at which the CTE of HMX overtakes that of the Viton matrix and subsequently drops beneath it again. To further understand the elastic and plastic heating rates (see Eqs. 3.13 and 3.15) in Figure 7.6, we need to analyze the stress states. The corresponding stress state regimes are as follows: (i) between

300 [K] and 459 [K], the matrix expands but this expansion is dampened by the stiff HMX particles which builds stress within the matrix and eventually causes it to yield plastically, (ii) between 459 [K] and 473 [K], since the HMX now has a larger CTE than that of Viton, it no longer dampens the expansion of the matrix but rather amplifies it such that the matrix unloads elastically and pauses plastic deformation, (iii) between 473 [K] and 520 [K] the CTE of the HMX particles is again lower than that of the Viton matrix such that the matrix again loads elastically back to the previous yield surface, and (iv) beyond 520 [K] stress continues to build within the matrix while it again deforms elasto-plastically. Figure 7.6(c) shows that the plastic heating rate corresponds directly with these stress states (e.g., the 0.0 [W/kg] rate between 459 [K] and 520 [K] where the matrix is unloading and reloading back to the yield surface). We note that the stresses experienced by the particles for our heating and mechanical loading conditions are well below the HMX yield stress and, thus, the particles do not flow plastically. In terms of overall heating effects, the chemical heating significantly outweighs both mechanical heating terms. Locally (e.g., within matrix regions confined between close particles, see Figure 7.4(a)) all effects are important.

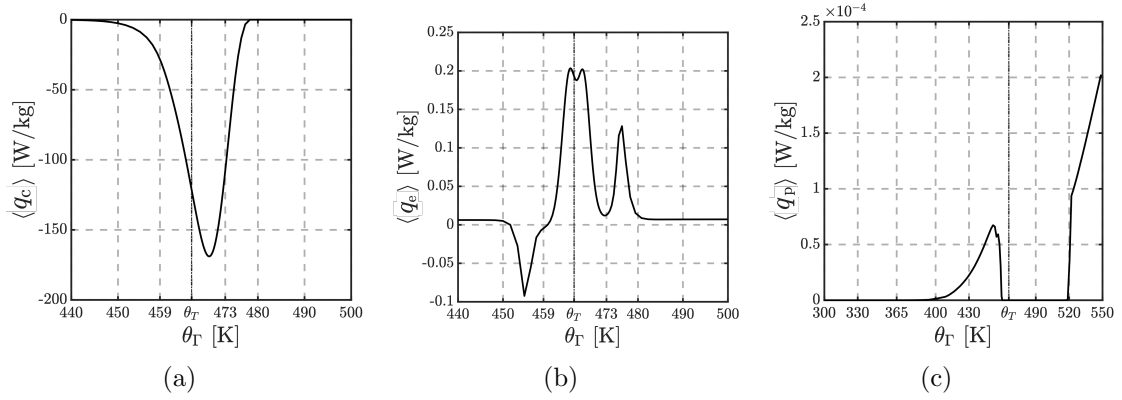


Figure 7.6. Overall (a) chemical, (b) elastic, and (c) plastic heating rates in the composite sample for the 5 [K/min] boundary heating rate.

### 7.2.1 Effect of Particle Volume Fraction

In this section, we discuss the effect of particle volume fraction on the CTM material response. The results are averaged across five realizations at the various volume fractions, and at a fixed boundary heating rate of 5 [K/min]. The ensemble and volumetric averages over the relevant domains (entire domain, particles, or matrix) are defined in Eq. 7.4.

We begin with Figure 7.7 which shows that the average stress magnitude,  $\sigma \equiv \sqrt{\boldsymbol{\sigma} : \boldsymbol{\sigma}}$ , experienced by the composite increases with particle volume fraction. This behavior can be explained by the increasing particle density. The particles are significantly stiffer than the matrix. Therefore, for a fixed domain size, more particles means larger stress magnitudes. Figure 7.7 also includes shaded regions which indicate  $\pm 1$  standard deviation from the mean.

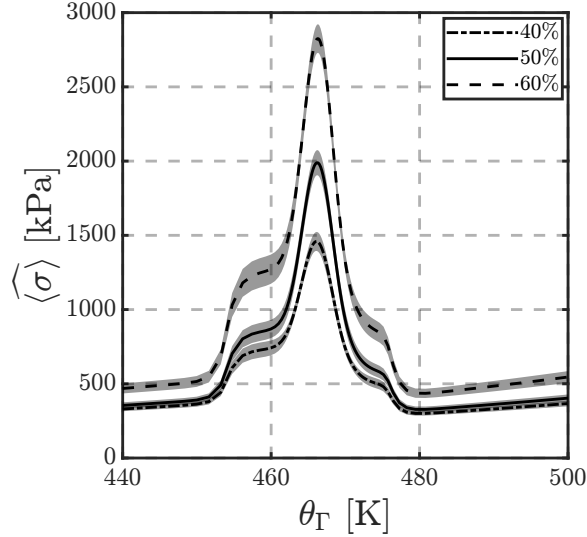


Figure 7.7. Overall composite Cauchy stress magnitude  $\sigma \equiv \sqrt{\boldsymbol{\sigma} : \boldsymbol{\sigma}}$ . The shaded regions indicate  $\pm 1$  standard deviation from the mean for five realizations.

We continue by analyzing the average chemical heating rates and temperature rates experienced in the entire domain. As can be seen in Figure 7.8(a), increasing the particle volume fraction increases the magnitude of the average chemical heating within the domain. Figure 7.8(b) shows that increasing the particle volume fraction increases the magnitude of variation between the temperature rates experienced within the sample as compared to the prescribed boundary temperature rate (5 [K/min]).

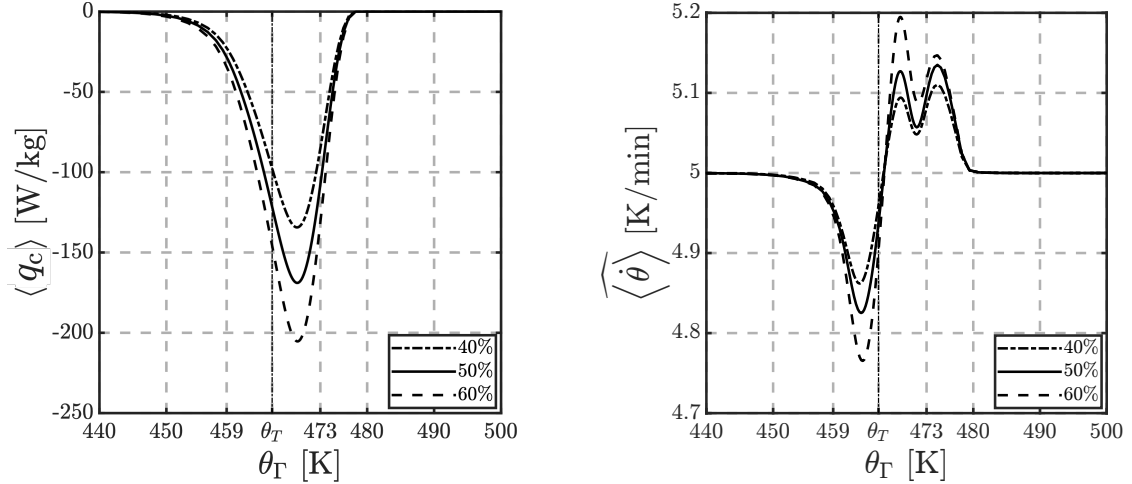


Figure 7.8. Average chemical heating rate (a) and temperature rate (b) in the domain for the 40%, 50%, and 60% volume fractions at the 5 [K/min] boundary heating rate. The shaded regions indicating  $\pm 1$  standard deviation from the mean for five realizations are omitted since standard deviations less than 0.8 [W/kg] for the chemical heating rate and coefficients of variation less than 0.5% for the temperature rate are observed. The coefficient of variation cannot be used for the chemical heating rate since the means reach values near zero before and after the transition regime.

We continue by discussing the average domain specific heats at constant pressure and volume for the entire cell in Figure 7.9. We observe that the magnitudes of both specific heat curves change considerably with increasing particle volume fraction. This can be expected considering the influence of the highly nonlinear CTE of the particles (see Eqs. 2.35 and 3.6). We note that while  $c_p$  with such large magnitudes may seem unrealistic, such behavior has been experimentally measured. For example, in the work of Lamberg et al. [46] on phase-change materials, the  $c_p$  of technical grade paraffin was found to vary between  $\mathcal{O}(2 \times 10^3)$  and  $\mathcal{O}(6 \times 10^4)$  [J/(kg·K)] using DSC measurements (see Fig. 5 in [46]). In the work of Cao et al. [13], DSC measurements

showed that the specific heat capacity of phase change material RT21 also experienced such strong variations in value.

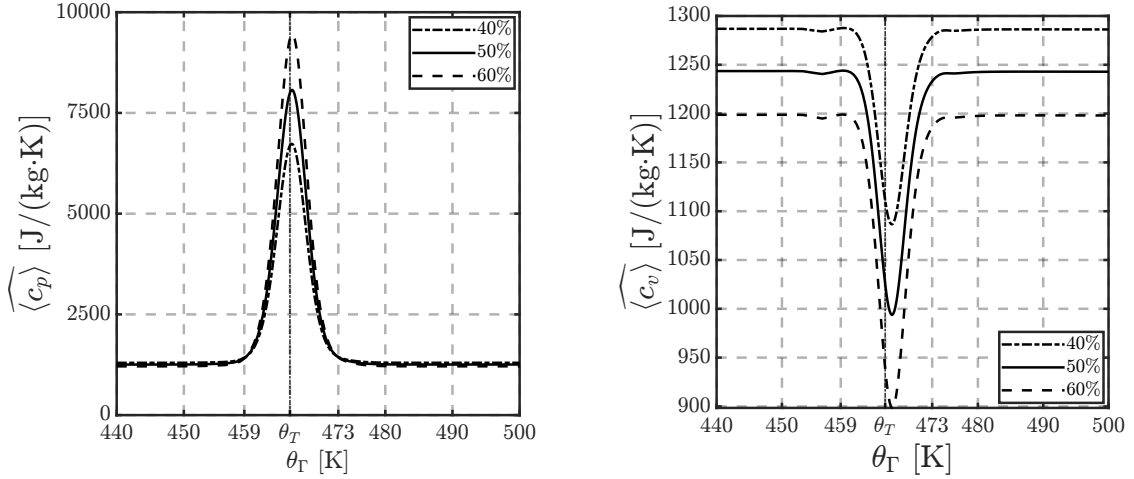


Figure 7.9. Overall composite specific heat at constant pressure (a) and constant volume (b) for a boundary heating rate of 5 [K/min]. The shaded regions indicating  $\pm 1$  standard deviation from the mean from five realizations are omitted since coefficients of variation less than 0.8% for  $c_p$  and less than 0.14% for  $c_v$  are observed.

## 7.2.2 Effect of Boundary Heating Rate

In this section, we discuss the effect of the boundary heating rate on the CTM material response. The results are averaged across five realizations at the various boundary heating rates, and at a fixed particle volume fraction of 50%. The ensemble and volumetric averages over the relevant domains (entire domain, particles, or matrix) are defined in Eq. 7.4.

In Figure 7.10, we plot the average total heating rates and compare them across different boundary heating conditions. We can see that the magnitudes of the total

heating rates increase with increasing boundary heating rate,  $\dot{\theta}_\Gamma$ .

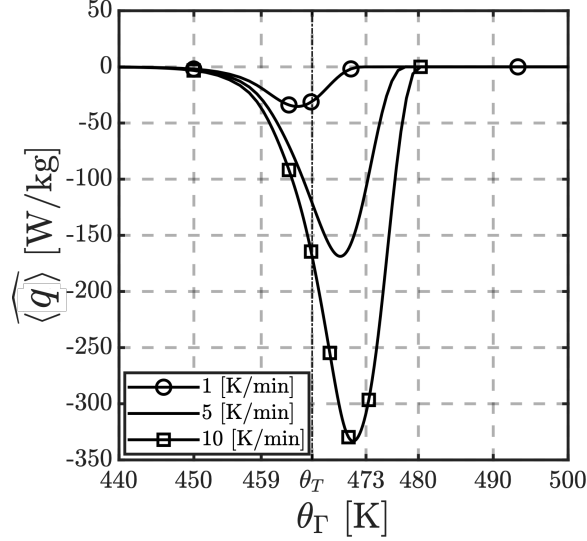


Figure 7.10. Overall total heating rates for the different boundary heating conditions. The shaded regions indicating  $\pm 1$  standard deviation from the mean from five realizations are omitted since standard deviations of less than 2.8 [W/kg] are observed. The coefficient of variation cannot be used since the means reach values close to zero before and after the transition regime.

As previously discussed in Section 6.2, for a chemical heating rate given by Eq. 3.4 and a reaction constant given by Eq. 2.14, the chemical heating rate extremum in the particles occurs at temperature  $\theta_c$  given by Eq. 6.1. With this estimate for the temperature at which the chemical heating rate extremum occurs, we can further elaborate on the extrema for different heating rates in Figure 7.10.

In Figure 7.11(a), we plot the average chemical heating rate in the particles for each boundary heating rate,  $\dot{\theta}_\Gamma$ , and note the critical temperature,  $\theta_c$ , at which the chemical heating rates reach their extrema. We call this pair of data  $(\dot{\theta}_\Gamma, \theta_c)$  and

mark them in Figure 7.11(a) for easy identification. In Figure 7.11(b), we plot these corresponding extrema as  $(\dot{\theta}_T, \theta_c)$  coordinate pairs along with the prediction from Eq. 6.1. Figure 7.11(b) shows remarkable agreement between the critical temperatures predicted by the computational simulations in Figure 7.11(a) and this theoretically derived equation for the critical temperature in the particles. Furthermore, we note that this serves as a strong solution verification of the computational results.

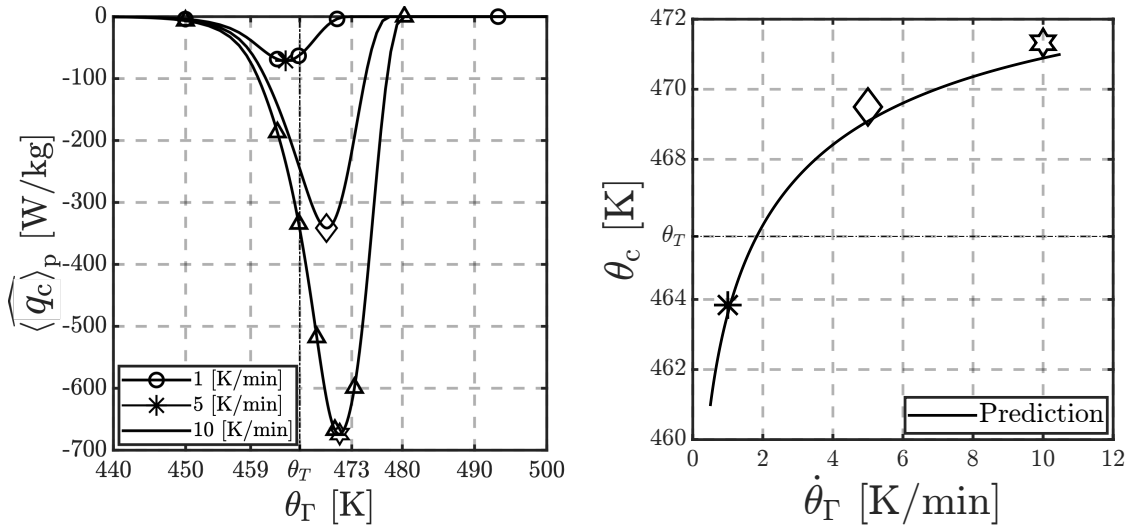


Figure 7.11. Chemical heating rate in the particles (a) and critical temperature for the chemical heating rate as a function of boundary heating rate (b). The shaded regions indicating  $\pm 1$  standard deviation from the mean from five realizations are omitted since standard deviations of less than 6 [W/kg] are observed. The coefficient of variation cannot be used since the means reach values close to zero before and after the transition regime.

## CHAPTER 8

### CONCLUSIONS

#### 8.1 Summary of Contributions

In conclusion, advancements have been made in the modeling and simulation of heterogeneous reactive materials. This dissertation has developed a thermodynamically consistent chemo-thermo-mechanical model and computational framework for the analysis of heterogeneous materials. The model has been calibrated using available experimental data, then applied to the  $\beta \rightarrow \delta$  phase transition of single crystal HMX as well as HMX based PBXs. The contributions of this work to the scientific community are summarized as follows.

#### **Contribution to the Continuum Formulation**

This dissertation has provided a concise presentation of the governing partial differential equations and balance laws necessary to model the desired systems which was derived in a thermodynamic context with respect of the Second Law (of Thermodynamics). These equations were given in both the Eulerian and Lagrangian settings with explicit transformations provided when necessary. Novel, theoretically derived continuum equations for the specific heats at constant elastic strains (i.e., constant pressure,  $c_p$ ) and at constant deformation (i.e., constant volume,  $c_v$ ) were also presented. Furthermore, a novel, theoretically derived equation which predicts the critical temperature at which maximum heat release or consumption occurs for Arrhenius type kinetics was provided and utilized as a tool of comparison to simulation

results. Finally, novel, nonlinear, temperature dependent models for the coefficient of thermal expansion and bulk modulus of material systems undergoing solid-solid phase transition were introduced.

### **Contribution to Computational Modeling**

This dissertation also provided algorithms for discretization and implementation needed to solve the governing equations numerically for the fields of interest. This work focused on the development and implementation of such algorithms using the finite element method. This has led to two (2) computational modeling publications. Williams and Matouš [101] detail the  $\beta \rightarrow \delta$  phase transition of single crystal HMX considering reaction phenomena, nonlinear thermal expansion, and nonlinear elastic parameters. Williams et al. [102] extend the work of [101] by investigating HMX based energetic materials with the addition of plasticity and microstructure considerations.

### **Contribution to Physical Understanding**

This dissertation further provided, in great detail, the results of investigating the multiphysics associated with solid-solid phase transformations. Specifically, detailed simulation results for single crystal HMX as well as HMX based plastic bonded explosives were provided with accompanying analysis. These results contributed insights into the intricate relationships between evolving material properties, microstructural geometry, and CTM response to thermo-mechanical stimuli. Specifically, this work contributed ideas on the physics of the evolution of the specific heats, elastic moduli, and coefficient of thermal expansion of solid materials undergoing phase transition. It also contributed physical understanding of the effect of microstructure on the behavior of plastic bonded explosives. Finally, it contributed physical understanding of

the material response of energetic materials experiencing various heating rates and mechanical loading conditions.

## 8.2 Future Directions

From this dissertation, a great deal of future directions may be taken in the progress of this work. Some of these potential undertakings are described below in the context of the contributions described in Section 8.1.

### **Pertaining to the Continuum Formulation**

The addition of more complex chemical models which include multi-step, multi-directional reactions will be a key component of realizing this endeavor. Kinetics models which include temperature and pressure dependency may prove crucial for advancement. The introduction of rate-dependent elastoplasticity will be necessary for shock simulations and for systems which include higher material complexity. Including damage mechanics in the formulation will provide further insight into the deterioration and debonding of the plastic binding matrix within PBXs.

### **Pertaining to Computational Modeling**

Extending simulations to three dimensions is important, largely in part due to the complex nature of the physics involved. Similarly, simulations on physically larger material systems using state-of-the-art massively parallel software will be particularly relevant. On a related note, computational domains with more complex (i.e., realistic) microstructural geometry will prove to be elucidating. More advanced numerical analysis techniques may be of great interest, especially for validation exercises which may require higher fidelity simulation results.

## **Pertaining to Physical Understanding**

The previously mentioned directions will naturally require more advanced methods of material parameter and geometry calibration; this would be yet another future direction to take. Beyond extending the work, the validation of the simulation results using the aforementioned simulation guided experiments, among others, will be more valuable. The conducting of experiments guided by the results of these and future computational simulations will be arduous but highly productive. To that end, guiding the synthesis of novel metastable materials will prove to be lucrative. Finally, for the case of HMX specific studies, extending this work beyond the pre-ignition phase will be worthwhile. Specifically, the modeling of deflagration and detonation is and will continue to be of great interest to the scientific community.

## APPENDIX A

### LAGRANGIAN FRAME REPRESENTATION

The governing equations of the CTM model can be expressed in the Lagrangian frame of reference through straightforward manipulations.

#### A.1 Conservation of Energy

In this section, we present the transformations needed for the conservation of energy, Eq. 2.32. The transformation rule for the scalar specific heat is simply  $c_p = C_p$ . By geometric arguments, it is natural to define the Lagrangian heat flux vector as

$${}^0\vec{\mathbf{q}} = \mathbf{J}\mathbf{F}^{-1} \vec{\mathbf{q}}. \quad (\text{A.1})$$

The spatial heat flux vector, given by Eq. 2.7, can be decomposed as

$$\begin{aligned} \vec{\mathbf{q}} &= -\Lambda \nabla \theta, \\ &= -\Lambda_{ij} \frac{\partial \theta}{\partial x_j}, \\ &= -\Lambda_{ij} \frac{\partial \theta}{\partial {}^0x_J} \frac{\partial {}^0x_J}{\partial x_j}, \\ &= -\Lambda_{ij} \frac{\partial \theta}{\partial {}^0x_J} \mathbf{F}_{Jj}^{-1}, \\ &= -\Lambda_{ij} \mathbf{F}_{jJ}^{-\top} \frac{\partial \theta}{\partial {}^0x_J}, \end{aligned}$$

or simply

$$\vec{\mathbf{q}} = -\Lambda \mathbf{F}^{-\top} {}^0\nabla \theta. \quad (\text{A.2})$$

Thus, Eq. A.1 becomes

$$\begin{aligned} {}^0\vec{\mathbf{q}} &= - [\mathbf{J}\mathbf{F}^{-1} \boldsymbol{\Lambda} \mathbf{F}^{-\top}] {}^0\nabla\theta, \\ &= -{}^0\boldsymbol{\Lambda} {}^0\nabla\theta, \end{aligned} \tag{A.3}$$

where the term in brackets is defined as the Lagrangian (material) conductivity tensor,  ${}^0\boldsymbol{\Lambda} \equiv \mathbf{J}\mathbf{F}^{-1} \boldsymbol{\Lambda} \mathbf{F}^{-\top}$ . From Eq. A.1, we also have that

$$\begin{aligned} \nabla \cdot \vec{\mathbf{q}} &= \nabla \cdot (\mathbf{F} {}^0\vec{\mathbf{q}}/\mathbf{J}) \\ &= \mathbf{F} [\nabla^0 \vec{\mathbf{q}}] / \mathbf{J} \\ &= \mathbf{F}_{iI} \left[ \frac{\partial^0 \vec{\mathbf{q}}_I}{\partial x_i} \right] / \mathbf{J} \\ &= \mathbf{F}_{iI} \left[ \frac{\partial^0 x_J}{\partial x_i} \frac{\partial^0 \vec{\mathbf{q}}_I}{\partial^0 x_J} \right] / \mathbf{J} \\ &= \mathbf{F}_{iI} \mathbf{F}_{Ji}^{-1} \frac{\partial^0 \vec{\mathbf{q}}_I}{\partial^0 x_J} / \mathbf{J} \\ &= \delta_{IJ} \frac{\partial^0 \vec{\mathbf{q}}_I}{\partial^0 x_J} / \mathbf{J} \\ &= \frac{\partial^0 \vec{\mathbf{q}}_I}{\partial^0 x_I} / \mathbf{J} \end{aligned}$$

or simply

$$\nabla \cdot \vec{\mathbf{q}} = {}^0\nabla \cdot {}^0\vec{\mathbf{q}}/\mathbf{J}. \tag{A.4}$$

Here, we have taken advantage of the fact that  $\partial\mathbf{F}/\partial\vec{\mathbf{x}} = \mathbf{0}$ . The transformation rule for mass fraction,  $y$ , is simply  $y = Y$  such that Eq. 3.2 becomes

$$\dot{Y}_\alpha = \nu_\alpha k_c (1 - Y_\delta), \tag{A.5}$$

such that the chemical heating term, Eq. 3.4, becomes

$$q_c = - \sum_{n=1}^{N_s} e_n \nu_n k_c (1 - Y_\delta) = -k_c (1 - Y_\delta) \Delta e^{\text{rxn}} = Q_c. \quad (\text{A.6})$$

The elastic heating term, Eq. 3.13, can be expressed in terms of Lagrangian variables using Eq. 3.14 as

$$\begin{aligned} q_e &= \frac{3\alpha\theta}{\rho} \left[ \text{dev}[\boldsymbol{\sigma}] - \left( J_e \frac{\partial^2 J_e}{\partial J_e^2} \right) \mathbf{1} \right] : \mathbf{d}_e \\ &= \frac{3\alpha\theta J}{\rho_0} \left[ \text{dev}[\boldsymbol{\sigma}] - \left( J_e \frac{\partial^2 J_e}{\partial J_e^2} \right) \mathbf{1} \right] : \left[ \mathbf{F}^{-\top} \dot{\mathbf{E}}_e \mathbf{F}^{-1} \right] \\ &= \frac{3\alpha\theta}{\rho_0} \left[ \mathbf{J} \mathbf{F}^{-1} \text{dev}[\boldsymbol{\sigma}] \mathbf{F}^{-\top} - \left( J_e \frac{\partial^2 J_e}{\partial J_e^2} \right) \mathbf{J} \mathbf{C}^{-1} \right] : \dot{\mathbf{E}}_e \\ &= \frac{3\alpha\theta}{\rho_0} \left[ \text{DEV}[\mathbf{S}] - \left( J_e \frac{\partial^2 J_e}{\partial J_e^2} \right) \mathbf{J} \mathbf{C}^{-1} \right] : \dot{\mathbf{E}}_e = Q_e, \end{aligned} \quad (\text{A.7})$$

where we use the conservation of mass to express  $\rho$  as  $\rho_0/J$ . Here,  $\dot{\mathbf{E}}_e \neq \dot{\mathbf{C}}_e/2$ , but rather we *define*  $\dot{\mathbf{E}}_e$  as

$$\dot{\mathbf{E}}_e \equiv \frac{1}{2} \left[ \dot{\mathbf{C}} - \left[ \mathbf{C} \mathbf{C}_p^{-1} \dot{\mathbf{C}}_p \right]^{\text{sym}} - 2\alpha\dot{\theta} \mathbf{C} \right]. \quad (\text{A.8})$$

Similarly, by noting that the normal to the yield surface in the Lagrangian frame is given as  $\mathbf{N} = \mathbf{F}^{-1} \mathbf{n} \mathbf{F}^{-\top}$ , and that the transformation rule for the scalar plastic consistency parameter is simply  $\dot{\lambda}_p = \dot{\Lambda}_p$ , the plastic heating term Eq. 3.15 becomes

$$\begin{aligned} q_p &= \frac{f_{\text{TQ}}}{\rho} \dot{\lambda}_p \boldsymbol{\sigma} : \mathbf{n} \\ &= \frac{f_{\text{TQ}} J}{\rho_0} \dot{\Lambda}_p \boldsymbol{\sigma} : \left[ \mathbf{F} \mathbf{N} \mathbf{F}^\top \right] \\ &= \frac{f_{\text{TQ}}}{\rho_0} \dot{\Lambda}_p \left[ \mathbf{F}^\top \mathbf{F} \mathbf{S} \mathbf{F}^\top \mathbf{F} \right] : \mathbf{N} \\ &= \frac{f_{\text{TQ}}}{\rho_0} \dot{\Lambda}_p \left[ \mathbf{C} \mathbf{S} \right] : \left[ \mathbf{N} \mathbf{C} \right] = Q_p. \end{aligned} \quad (\text{A.9})$$

Note that  $\mathbf{C} \mathbf{S} = \boldsymbol{\Sigma}$  is the Mandel stress measure [56].

In summary, by multiplying Eq. 2.32 throughout by  $\mathbf{J}$ , applying these transformation rules, applying the conservation of mass Eq. 2.5, and simplifying, we get the Lagrangian representation of the conservation of energy as

$$\rho_0 C_p \dot{\theta} + {}^0\nabla \cdot {}^0\vec{\mathbf{q}} = \rho_0 (R + Q_c + Q_e + Q_p) \quad \text{in } \Omega_0 \times \mathbb{R}^+. \quad (\text{A.10})$$

Here,  $R = r$  is the scalar heat source in the reference configuration.

## A.2 Conservation of Linear Momentum

In this section, we present the transformations needed for the conservation of linear momentum, Eq. 2.10. We begin by introducing the second (symmetric) Piola-Kirchhoff and Kirchhoff stress measures,

$$\mathbf{S} = \mathbf{J} \mathbf{F}^{-1} \boldsymbol{\sigma} \mathbf{F}^{-\top} = 2\rho_0 \frac{\partial \varphi}{\partial \mathbf{C}} = \text{DEV}[\mathbf{S}] + p \mathbf{J} \mathbf{C}^{-1}, \quad (\text{A.11a})$$

$$\text{DEV}[\mathbf{S}] \equiv \mu J_p J_\theta \text{DEV} \left[ \mathbf{J}^{-2/3} \widehat{\mathbf{C}}_p^{-1} \right] = \mathbf{J} \mathbf{F}^{-1} \text{dev}[\boldsymbol{\sigma}] \mathbf{F}^{-\top}, \quad (\text{A.11b})$$

where the deviator of a material tensor is given as  $\text{DEV}[\bullet] = (\bullet) - (\bullet : \mathbf{C}) \mathbf{C}^{-1}$ . In this case, it is easy to show that  $\mathbf{F}^{-1} \text{dev}[\widehat{\mathbf{b}}_e] \mathbf{F}^{-\top} = \text{DEV} \left[ \mathbf{J}^{-2/3} \widehat{\mathbf{C}}_p^{-1} \right]$  using  $\widehat{\mathbf{b}}_e = \mathbf{J}^{-2/3} \mathbf{F} \widehat{\mathbf{C}}_p^{-1} \mathbf{F}^\top$  and  $\text{tr}(\widehat{\mathbf{b}}_e) = \mathbf{1} : \widehat{\mathbf{b}}_e = \mathbf{1} : \left[ \mathbf{J}^{-2/3} \mathbf{F} \widehat{\mathbf{C}}_p^{-1} \mathbf{F}^\top \right] = \mathbf{C} : \left[ \mathbf{J}^{-2/3} \widehat{\mathbf{C}}_p^{-1} \right]$ . We note also that the scalar  $\varphi_e$ , Eq. 2.16, can be represented as a function of Lagrangian fields as

$$\rho_0 \varphi_e(\mathbf{C}, \mathbf{C}_p, \theta) = J_p J_\theta (\widehat{W}_e + U_e), \quad (\text{A.12a})$$

$$\widehat{W}_e(\mathbf{C}, \mathbf{C}_p, \theta) = \frac{1}{2} \mu(\theta) \left[ \mathbf{C} : \left[ \mathbf{J}^{-2/3} \widehat{\mathbf{C}}_p^{-1} \right] - 3 \right], \quad (\text{A.12b})$$

$$U_e(J_e, \theta) = \frac{1}{4} \kappa(\theta) \left[ (J_e - 1)^2 + (\log J_e)^2 \right], \quad (\text{A.12c})$$

where  $J_e(\mathbf{C}, \mathbf{C}_p, \theta) = J/(J_p J_\theta)$ . The spatial residuals given in Eq. 4.5 are easily represented in the material frame using straightforward pull-back operations where appropriate. The resulting material residual equations are given as

$$\mathcal{R}_u = \int_{\Omega_0} \mathbf{S}_{IJ} : \delta \mathbf{E}_{IJ} \, d\Omega_0, \quad (\text{A.13a})$$

$$\mathcal{R}_p = \int_{\Omega_0} \delta p [J - \gamma J_\theta J_p] \, d\Omega_0, \quad (\text{A.13b})$$

$$\mathcal{R}_\gamma = \int_{\Omega_0} \delta \gamma [U'_e - p] J_\theta J_p \, d\Omega_0. \quad (\text{A.13c})$$

Similarly, the associated spatial tangents given in Eq. 4.7 are also easily represented in the material frame using appropriate pull-back relations. The resulting tangent terms are given as

$$\mathcal{K}_{uu} = \int_{\Omega_0} [\delta \mathbf{E}_{IJ} : \mathbf{A}_{IJKL} : \delta \mathbf{E}_{KL} + \mathbf{S}_{IJ} : \delta \delta \mathbf{E}_{IJ}] \, d\Omega_0, \quad (\text{A.14a})$$

$$\mathcal{K}_{up} = \int_{\Omega_0} J \mathbf{C}_{IJ}^{-1} : \delta \mathbf{E}_{IJ} \, \delta p \, d\Omega_0 = \mathcal{K}_{pu}^\top, \quad (\text{A.14b})$$

$$\mathcal{K}_{u\gamma} = \mathcal{K}_{\gamma u}^\top = 0, \quad (\text{A.14c})$$

$$\mathcal{K}_{pp} = 0, \quad (\text{A.14d})$$

$$\mathcal{K}_{\gamma p} = - \int_{\Omega_0} \delta \gamma \, \delta p J_\theta J_p \, d\Omega_0 = \mathcal{K}_{p\gamma}^\top, \quad (\text{A.14e})$$

$$\mathcal{K}_{\gamma\gamma} = \int_{\Omega_0} \delta \gamma \, \delta \gamma \, U''_e J_\theta J_p \, d\Omega_0. \quad (\text{A.14f})$$

Explicit formulae for calculating  $\mathbf{A}_{ijkl}$  are provided in Section A.3 while

$$\delta \mathbf{E}_{IJ} \equiv \frac{1}{2} \delta \mathbf{C}_{IJ} = [\mathbf{F}^\top \delta \mathbf{F}]_{IJ}^{\text{sym}}, \quad (\text{A.15a})$$

$$\delta \delta \mathbf{E}_{IJ} \equiv [\delta \mathbf{F}^\top \delta \mathbf{F}]_{IJ}. \quad (\text{A.15b})$$

The Newton-Raphson equation given by Eq. 4.6 is identical. The function spaces for solving Eq. A.13 are entirely similar to those presented in Section 4.2.1. Namely, the

fields are functions of  ${}^0\vec{\mathbf{x}}$  while  $H^k(\Omega_0)$ ,  $k \in \{0, 1, 2\}$  Sobolev spaces over the reference configuration,  $\Omega_0$ , are employed.

### A.3 Plastic Integration Algorithm

The process described in Section 4.3.4 is entirely similar for the Lagrangian frame. Below, we summarize this process. The interested reader may find further discussions of this algorithm in [76, 79]. This concise summary of the algorithm, including consistent (exact) tangent terms to be used in Eq. A.14, is performed at each Gauss point for each Newton-Raphson iteration of the mechanical solver.

#### Material Plastic Integration Algorithm

1. Update the configuration.

$$\begin{aligned} [\mathbf{F}]_{n+1} &= \mathbf{1} + {}^0\nabla [\vec{\mathbf{u}}]_{n+1} \\ [J]_{n+1} &= \det([\mathbf{F}]_{n+1}) \\ [J_\theta]_{n+1} &= \vartheta^3([\theta]_{n+1}) \end{aligned}$$

2. Compute trial material elastic predictor state.

$$\begin{aligned} [\widetilde{\mathbf{C}}_p^{-1}] &= [\mathbf{C}_p^{-1}]_n \\ \text{DEV}[\widetilde{\mathbf{S}}] &= \mu [J_\theta]_{n+1} [J^{-2/3}]_{n+1} \text{DEV}[\widetilde{\mathbf{C}}_p^{-1}] \\ [\widetilde{\mathcal{M}}] &= \sqrt{[\mathbf{C}]_{n+1} \text{DEV}[\widetilde{\mathbf{S}}] : [\text{DEV}[\widetilde{\mathbf{S}}] \mathbf{C}]_{n+1}} \\ &= \sqrt{\mathbf{1} : [\mathbf{C}]_{n+1} \text{DEV}[\widetilde{\mathbf{S}}]}^2 \\ [\widetilde{\mathbf{N}}] &= \frac{\text{DEV}[\widetilde{\mathbf{S}}]}{[\widetilde{\mathcal{M}}]} \\ [\widetilde{\varepsilon}_p] &= [\varepsilon_p]_n \\ [\widetilde{I}_1] &= [J^{-2/3}]_{n+1} [\widetilde{\mathbf{C}}_p^{-1}] : [\mathbf{C}]_{n+1} \\ \bar{\mu} &= \frac{1}{3} \mu [J_\theta]_{n+1} [\widetilde{I}_1] \\ \Delta\lambda_p &= \zeta_0 = \zeta_1 = \zeta_2 = \zeta_3 = \zeta_4 := 0 \end{aligned}$$

3. Check for plastic loading.

$$[\widetilde{f}_p] = \frac{1}{[J_\theta]_{n+1}} [\widetilde{\mathcal{M}}] - \sqrt{\frac{2}{3}} (\sigma_0 + H [\widetilde{\varepsilon}_p])$$

IF  $[\widetilde{f}_p] \leq 0$ , set  $[\bullet]_{n+1} = [\bullet]$  and proceed to 5 (elastic step).

ELSE, proceed to 4 (plastic step).

4. Perform return mapping and update the scaling parameters.

$$\begin{aligned} \Delta\lambda_p &:= \frac{(3/2)[\widetilde{f}_p]}{\mu[\widetilde{I}_1] + H} \\ \zeta_0 &:= \frac{\mu[\widetilde{I}_1]}{[\mu[\widetilde{I}_1] + H]} \\ \zeta_1 &:= \frac{2\bar{\mu}\Delta\lambda_p}{[\widetilde{\mathcal{M}}]} \\ \zeta_2 &:= (1 - \zeta_0) \frac{2\Delta\lambda_p[\widetilde{\mathcal{M}}]}{3\bar{\mu}} \\ \zeta_3 &:= \zeta_0 - \zeta_1 + \zeta_2 \\ \zeta_4 &:= (\zeta_0 - \zeta_1) \frac{[\widetilde{\mathcal{M}}]}{\bar{\mu}} \end{aligned}$$

5. Compute tangents.

$$\begin{aligned} \mathbb{C}_{IJKL}^{\text{sym}} &\equiv \frac{1}{2} \left[ [\mathbf{C}_{IK}^{-1}]_{n+1} [\mathbf{C}_{JL}^{-1}]_{n+1} + [\mathbf{C}_{IL}^{-1}]_{n+1} [\mathbf{C}_{JK}^{-1}]_{n+1} \right] \\ [\widetilde{\mathbf{A}}]_{IJKL}^{\text{DEV}} &\equiv 2\bar{\mu} \left[ \mathbb{C}_{IJKL}^{\text{sym}} - \frac{1}{3} [\mathbf{C}_{IJ}^{-1}]_{n+1} [\mathbf{C}_{KL}^{-1}]_{n+1} \right] \\ &\quad - \frac{2}{3} [\widetilde{\mathcal{M}}] \left[ [\widetilde{\mathbf{N}}]_{IJ} [\mathbf{C}_{KL}^{-1}]_{n+1} + [\mathbf{C}_{IJ}^{-1}]_{n+1} [\widetilde{\mathbf{N}}]_{KL} \right] \\ \mathbf{A}_{IJKL}^{\text{DEV}} &\equiv [\widetilde{\mathbf{A}}]_{IJKL}^{\text{DEV}} - \zeta_1 [\widetilde{\mathbf{A}}]_{IJKL}^{\text{DEV}} - 2\bar{\mu}\zeta_3 [\widetilde{\mathbf{N}}]_{IJ} [\widetilde{\mathbf{N}}]_{KL} \\ &\quad - 2\bar{\mu}\zeta_4 [\widetilde{\mathbf{N}}]_{IJ} \text{DEV} \left[ [\widetilde{\mathbf{N}}] [\mathbf{C}]_{n+1} [\widetilde{\mathbf{N}}] \right]_{KL} \\ \mathbf{A}_{IJKL}^{\text{VOL}} &\equiv [p]_{n+1} [J]_{n+1} \left[ [\mathbf{C}_{IJ}^{-1}]_{n+1} [\mathbf{C}_{KL}^{-1}]_{n+1} - 2\mathbb{C}_{IJKL}^{\text{sym}} \right] \\ \mathbf{A} &\equiv \mathbf{A}^{\text{DEV}} + \mathbf{A}^{\text{VOL}} \end{aligned}$$

6. Update the intermediate configuration and stress.

$$[\mathbf{C}_p^{-1}]_{n+1} = [\widetilde{\mathbf{C}_p^{-1}}] - \frac{2}{3}\Delta\lambda_p \text{TR}\left([\widetilde{\mathbf{C}_p^{-1}}]\right) [\widetilde{\mathbf{N}}]$$

$$[\varepsilon_p]_{n+1} = [\widetilde{\varepsilon}_p] + \sqrt{\frac{2}{3}}\Delta\lambda_p$$

$$\text{DEV}[\mathbf{S}]_{n+1} = \text{DEV}[\widetilde{\mathbf{S}}] - 2\bar{\mu}\Delta\lambda_p[\widetilde{\mathbf{N}}]$$

$$[\mathbf{S}]_{n+1} = \text{DEV}[\mathbf{S}]_{n+1} + [p]_{n+1} [\mathbf{J}]_{n+1} [\mathbf{C}^{-1}]_{n+1}$$

## APPENDIX B

### CHEMO-THERMAL MODEL IN LIMIT OF SPATIAL HOMOGENEITY

The model described in Chapter 2 and specified in Chapter 3 can be analyzed in the case of spatial homogeneity under adiabatic conditions. In this case, the conservation of energy, Eq. 2.8, reduces to

$$c_p \dot{\theta} = q_c \quad \text{in } \Omega \times \mathbb{R}^+, \quad (\text{B.1a})$$

$$\theta(t) = \tilde{\theta}(t) \quad \text{on } \Gamma_\theta \times \mathbb{R}^+, \quad (\text{B.1b})$$

$$\vec{\mathbf{q}} \cdot \vec{\mathbf{n}} = 0 \quad \text{on } \Gamma_{\vec{\mathbf{q}}} \times \mathbb{R}^+, \quad (\text{B.1c})$$

$$\theta(t = 0) = \theta_0 \quad \text{in } \Omega, \quad (\text{B.1d})$$

while the reduced chemical conservation, Eq. 3.2, is

$$\dot{y}_\delta = k_c (1 - y_\delta) \quad \text{in } \Omega \times \mathbb{R}^+, \quad (\text{B.2a})$$

$$y_\delta(t = 0) = 0 \quad \text{in } \Omega, \quad (\text{B.2b})$$

$$y_\beta(t) = 1 - y_\delta(t) \quad \text{in } \Omega \times \mathbb{R}^+. \quad (\text{B.2c})$$

The reduced chemical heating term, Eq. 3.4, is

$$q_c = -k_c (1 - y_\delta) \Delta h^{\text{rxn}},$$

or, making use of Eq. B.2a,

$$q_c = -\dot{y}_\delta \Delta h^{\text{rxn}}. \quad (\text{B.3})$$

Combining Eqs. B.1a and B.3 thus yields

$$c_p \dot{\theta} = -y_\delta \Delta h^{\text{rxn}}. \quad (\text{B.4})$$

For the sake of this analysis, we consider  $\theta_0 = 453$  [K], i.e. the initiation temperature of the HMX  $\beta \rightarrow \delta$  reaction. It can readily be seen that near  $\theta \approx \theta_0$ , we have that  $c_p \approx {}^0c_p$  (i.e., constant, see Figure 6.6(a)) such that this equation can be integrated to find

$${}^0c_p \theta = -y_\delta \Delta h^{\text{rxn}} + C. \quad (\text{B.5})$$

Applying the conditions  $\theta(t=0) = \theta_0$  and  $y_\delta(t=0) = 0$  we calculate  $C$  as

$${}^0c_p \theta_0 = C, \quad (\text{B.6})$$

and conclude that temperature and mass fraction are related as

$$\theta(t) = \theta_0 - \left( \frac{\Delta h^{\text{rxn}}}{{}^0c_p} \right) y_\delta(t). \quad (\text{B.7})$$

For the parameters considered in this work, this is explicitly written as

$$\theta(t) = 453.0 - 43.35 y_\delta(t) \text{ [K]}. \quad (\text{B.8})$$

This gives us *implicit* solutions for  $y_\delta(t)$  and  $\theta(t)$ . Furthermore, this shows that in the large time limit where  $y_\delta \rightarrow 1$  [—], it is the case that  $\theta \rightarrow 409.7$  [K] roughly. Figure B.1(a) shows the result of using this in Eq. B.2a then solving the resulting ODE in  $y_\delta$  and  $t$ . Figure B.1(b) shows the associated temperature profile.

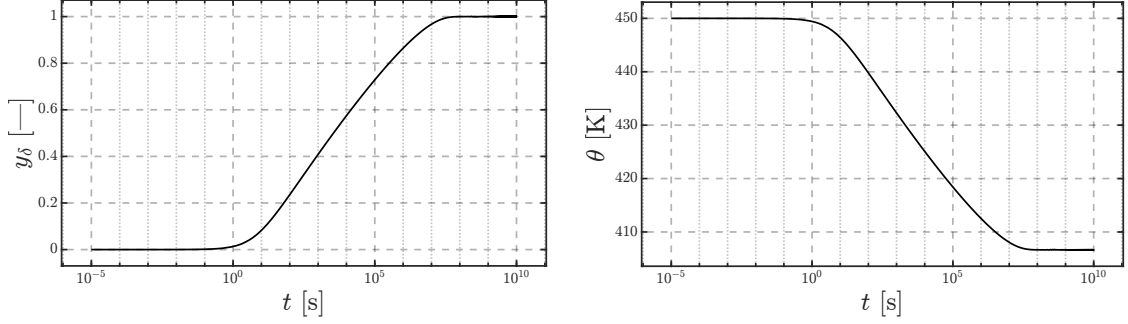


Figure B.1. Plots of (a)  $y_\delta$  and (b)  $\theta$  under spatially homogeneous, adiabatic conditions. Both plots employ a log scale for the  $t$  axis in order to highlight the dynamics.

For convenience, the full system of ODEs for the conditions considered in this section is provided below with relevant material parameters included.

$${}^0c_p \dot{\theta} = -\dot{y}_\delta \Delta h^{\text{rxn}}, \quad (\text{B.9a})$$

$$\dot{y}_\delta = A \hat{A}(\theta) \exp\left(-\frac{E_a}{R_u \theta}\right) (1 - y_\delta), \quad (\text{B.9b})$$

$$\hat{A}(\theta) = 0.0451\theta + 0.0088, \quad (\text{B.9c})$$

$$y_\delta(t = 0) = 0, \quad (\text{B.9d})$$

$$\theta(t = 0) = \theta_0, \quad (\text{B.9e})$$

where  ${}^0c_p = 1035$  [J/(kg·K)],  $\Delta h^{\text{rxn}} = 44870$  [J/kg],  $E_a/R_u = 51960$  [K], and  $A = 2.0 \times 10^{48}$  [s $^{-1}$ ]. Again,  $\theta_0$  can either be ‘ambient’ temperature (i.e., 300 [K]) or, for the aforementioned reasons, the HMX  $\beta \rightarrow \delta$  initiation temperature (i.e., 453 [K]).

## BIBLIOGRAPHY

1. R. A. Adams and J. J. Fournier. *Sobolev Spaces*, volume 140. Academic press, 2003.
2. L. Alawieh, T. Weihs, and O. Knio. A generalized reduced model of uniform and self-propagating reactions in reactive nanolaminates. *Combustion and Flame*, 160:1857–1869, 09 2013. doi: 10.1016/j.combustflame.2013.03.016.
3. R. J. Angel, M. Alvaro, R. Miletich, and F. Nestola. A simple and generalised p–t–v eos for continuous phase transitions, implemented in eosfit and applied to quartz. *Contributions to Mineralogy and Petrology*, 172(5): 29, 2017. doi: 10.1007/s00410-017-1349-x. URL <https://doi.org/10.1007/s00410-017-1349-x>.
4. *Calibration Methods for the Extended Prout-Tompkins Chemical Kinetics Model and Derived Cookoff Parameters for RDX, HMX, LX-10 and PBXN-109*, volume 3 of *Heat Transfer Summer Conference*, 07 2007. ASME/JSME. doi: 10.1115/HT2007-32279. URL <https://doi.org/10.1115/HT2007-32279>.
5. M. Baer. Modeling heterogeneous energetic materials at the mesoscale. *Thermochimica Acta*, 384(1):351 – 367, 2002. ISSN 0040-6031. doi: [https://doi.org/10.1016/S0040-6031\(01\)00794-8](https://doi.org/10.1016/S0040-6031(01)00794-8). URL <http://www.sciencedirect.com/science/article/pii/S0040603101007948>. ENERGETIC MATERIALS.
6. J. B. Baldo and W. N. d. Santos. Phase transitions and their effects on the thermal diffusivity behaviour of some SiO<sub>2</sub> polymorphs. *Cerâmica*, 48:172 – 177, 09 2002. ISSN 0366-6913. URL [http://www.scielo.br/scielo.php?script=sci\\_arttext&pid=S0366-69132002000300011&nrm=iso](http://www.scielo.br/scielo.php?script=sci_arttext&pid=S0366-69132002000300011&nrm=iso).
7. A. Barua and M. Zhou. Computational analysis of temperature rises in microstructures of HMX-Ethane PBXs. *Computational mechanics*, 52(1):151–159, 2013. ISSN 0178-7675.
8. M. Beneš and K. Matouš. Asynchronous multi-domain variational integrators for nonlinear hyperelastic solids. *Computer Methods in Applied Mechanics and Engineering*, 199(29):1992–2013, 2010. ISSN 0045-7825. doi: <https://doi.org/10.1016/j.cma.2010.02.017>. URL <https://www.sciencedirect.com/science/article/pii/S0045782510000757>.

9. D. I. Bolef and J. de Klerk. Anomalies in the elastic constants and thermal expansion of chromium single crystals. *Phys. Rev.*, 129:1063–1067, Feb 1963. doi: 10.1103/PhysRev.129.1063. URL <https://link.aps.org/doi/10.1103/PhysRev.129.1063>.
10. J. Burghardt, B. Leavy, J. Guilkey, Z. Xue, and R. Brannon. Application of Uintah-MPM to shaped charge jet penetration of aluminum. *IOP conference series. Materials Science and Engineering*, 10(1):012223–012223, 2010. ISSN 1757-899X.
11. H. Cady. Studies on the polymorphs of HMX. Technical Report LAMS-2652, Los Alamos Scientific Laboratory, 1961.
12. V. D. Cao, S. Pilehvar, C. Salas-Bringas, A. M. Szczotok, T. Q. Bui, M. Carmona, J. F. Rodriguez, and A.-L. Kjøniksen. Thermal performance and numerical simulation of geopolymers containing different types of thermoregulating materials for passive building applications. *Energy and Buildings*, 173:678–688, 2018. ISSN 0378-7788. doi: <https://doi.org/10.1016/j.enbuild.2018.06.011>. URL <https://www.sciencedirect.com/science/article/pii/S0378778817339245>.
13. V. D. Cao, T. Bui, and A.-L. Kjøniksen. Thermal analysis of multi-layer walls containing geopolymers and phase change materials for building applications. *Energy*, 186, 07 2019. doi: 10.1016/j.energy.2019.07.122.
14. C. Chen, Q. Tang, and T. Wang. A new thermo-elasto-plasticity constitutive equation for crystals. *Science China Physics, Mechanics & Astronomy*, 58(5):1–10, May 2015. ISSN 1869-1927. doi: 10.1007/s11433-015-5642-2. URL <https://doi.org/10.1007/s11433-015-5642-2>.
15. B. D. Coleman and W. Noll. The thermodynamics of elastic materials with heat conduction and viscosity. *Archive for Rational Mechanics and Analysis*, 13(1): 167–178, 1963. doi: 10.1007/BF01262690. URL <https://doi.org/10.1007/BF01262690>.
16. H.-L. Cui, G.-F. Ji, X.-R. Chen, Q.-M. Zhang, D.-Q. Wei, and F. Zhao. Phase transitions and mechanical properties of octahydro-1,3,5,7-tetranitro-1,3,5,7-tetrazocine in different crystal phases by molecular dynamics simulation. *Journal of Chemical & Engineering Data*, 55(9):3121–3129, 2010. doi: 10.1021/je100009m. URL <https://doi.org/10.1021/je100009m>.
17. L. Dagum and R. Menon. OpenMP: an industry standard API for shared-memory programming. *IEEE Computational Science and Engineering*, 5(1): 46–55, 1998. doi: 10.1109/99.660313.
18. S. Davison, N. Alger, D. Z. Turner, S. R. Subia, B. Carnes, M. J. Martinez, P. K. Notz, K. A. Klise, C. M. Stone, J. Field, Richard V., P. Newell, C. F. Jove-Colon,

- J. R. Red-Horse, J. E. Bishop, T. A. Dewers, P. L. Hopkins, M. Mesh, J. E. Bean, H. K. Moffat, and H. Yoon. Computational thermal, chemical, fluid, and solid mechanics for geosystems management. *NA*, 9 2011. doi: 10.2172/1029788.
19. P. M. Dickson, B. W. Asay, B. F. Henson, C. S. Fugard, and J. Wong. Measurement of phase change and thermal decomposition kinetics during cookoff of PBX 9501. *AIP Conference Proceedings*, 505(1):837–840, 2000. doi: 10.1063/1.1303599. URL <https://aip.scitation.org/doi/abs/10.1063/1.1303599>.
  20. P. M. Dickson, B. W. Asay, B. F. Henson, and L. B. Smilowitz. Thermal cook-off response of confined PBX-9501. *Proceedings of the Royal Society. A, Mathematical, physical, and engineering sciences*, 460(2052):3529–3546, 2004. ISSN 1364-5021.
  21. B. M. Dobratz and P. C. Crawford. *LLNL Explosives Handbook Properties of Chemical Explosives and Explosive Simulants*. Lawrence Livermore National Laboratory, 01 1985.
  22. S. Doll and K. Schweizerhof. On the Development of Volumetric Strain Energy Functions. *Journal of Applied Mechanics*, 67(1):17–21, 10 1999. ISSN 0021-8936. doi: 10.1115/1.321146. URL <https://doi.org/10.1115/1.321146>.
  23. L. Dong, D. S. Stone, and R. S. Lakes. Anelastic anomalies and negative poisson’s ratio in tetragonal batio3 ceramics. *Applied Physics Letters*, 96(14):141904, 2010. doi: 10.1063/1.3384996. URL <https://doi.org/10.1063/1.3384996>.
  24. S. Enibe. Thermal analysis of a natural circulation solar air heater with phase change material energy storage. *Renewable Energy*, 28(14):2269–2299, 2003. ISSN 0960-1481. doi: [https://doi.org/10.1016/S0960-1481\(03\)00071-5](https://doi.org/10.1016/S0960-1481(03)00071-5). URL <https://www.sciencedirect.com/science/article/pii/S0960148103000715>.
  25. W. S. Farren and G. I. Taylor. The heat developed during plastic extension of metals. *Proceedings of the Royal Society of London. Series A, Containing Papers of a Mathematical and Physical Character*, 107(743):422–451, 1925. ISSN 09501207. URL <http://www.jstor.org/stable/94269>.
  26. R. P. Fedkiw, B. Merriman, and S. Osher. High accuracy numerical methods for thermally perfect gas flows with chemistry. *Journal of Computational Physics*, 132(2):175 – 190, 1997. ISSN 0021-9991. doi: <https://doi.org/10.1006/jcph.1996.5622>. URL <http://www.sciencedirect.com/science/article/pii/S0021999196956223>.
  27. C. A. Felippa, K. Park, and C. Farhat. Partitioned analysis of coupled mechanical systems. *Computer Methods in Applied Mechanics and Engineering*, 190(24):3247 – 3270, 2001. ISSN 0045-7825. doi: [https://doi.org/10.1016/S0045-7825\(00\)00391-1](https://doi.org/10.1016/S0045-7825(00)00391-1). URL <http://www.sciencedirect>.

- [com/science/article/pii/S0045782500003911](https://doi.org/10.1063/1.5005997). Advances in Computational Methods for Fluid-Structure Interaction.
28. D. A. Frank-Kamenetskii. *Diffusion and Heat Exchange in Chemical Kinetics*. Princeton University Press, 2015. ISBN 9781400877195. URL <https://press.princeton.edu/books/hardcover/9780691653099/diffusion-and-heat-exchange-in-chemical-kinetics>.
  29. D. Funk, G. Laabs, P. Peterson, and B. Asay. Measurements of the stress/strain response of energetic materials as a function of strain rate and temperature: PBX 9501 and Mock 9501. In *AIP Conference Proceedings*, pages 145–148, 1996.
  30. W. Gautschi and W. F. Gahill. Exponential Integral and Related Functions. In M. Abramowitz and I. A. Stegun, editors, *Handbook of Mathematical Functions with Formulas, Graphs, and Mathematical Tables*, pages 227–252, New York City, New York, 1972. Dover.
  31. E. Glascoe, P. Hsu, H. Springer, M. DeHaven, N. Tan, and H. Turner. The response of the HMX-based material PBX-9 to thermal insults: thermal decomposition kinetics and morphological changes. Technical Report LLNL-JRNL-463953, Lawrence Livermore National Laboratory, 2010.
  32. J. Guilkey, T. Harman, and B. Banerjee. An Eulerian–Lagrangian approach for simulating explosions of energetic devices. *Computers & structures*, 85(11): 660–674, 2007. ISSN 0045-7949.
  33. C. Handley, B. Lambourn, N. Whitworth, H. James, and W. Belfield. Understanding the shock and detonation response of high explosives at the continuum and meso scales. *Applied Physics Reviews*, 5:011303, 03 2018. doi: 10.1063/1.5005997.
  34. D. M. Hanson-Parr and T. P. Parr. Thermal properties measurements of solid rocket propellant oxidizers and binder materials as a function of temperature. *Journal of Energetic Materials*, 17(1):1–48, 1999. doi: 10.1080/07370659908216094. URL <https://doi.org/10.1080/07370659908216094>.
  35. M. Herrmann, W. Engel, and N. Eisenreich. Phase transition of HMX and their significance for the sensitivity of explosives. In *Technical Meeting of Specialists MWDDEA AF-71-F/G-5304 – Physics of Explosives*, page 12, 1990.
  36. S. Hirotsu. Softening of bulk modulus and negative poisson’s ratio near the volume phase transition of polymer gels. *The Journal of Chemical Physics*, 94(5):3949–3957, 1991. doi: 10.1063/1.460672. URL <https://doi.org/10.1063/1.460672>.
  37. G. Holzapfel and J. Simo. Entropy elasticity of isotropic rubber-like solids at finite strains. *Computer Methods in Applied Mechanics Engineering*, 132(1–2): 17–44, 1996.

38. W. Hu, Y. Wu, F. Huang, and X. Wang. Numerical simulation analyses of  $\beta \rightarrow \delta$  phase transition for a finite-sized HMX single crystal subjected to thermal loading. *RSC Advances*, 8:24873–24882, 07 2018. doi: 10.1039/C8RA02649A.
39. M. Hunger, A. Entrop, I. Mandilaras, H. Brouwers, and M. Founti. The behavior of self-compacting concrete containing micro-encapsulated phase change materials. *Cement & concrete composites*, 31(10):731–743, 2009. ISSN 0958-9465.
40. T. L. Jackson and J. Buckmaster. Heterogeneous Propellant Combustion. *AIAA Journal*, 40:1122–1130, June 2002. doi: 10.2514/2.1761.
41. J. Ju. Energy-based coupled elastoplastic damage models at finite strains. *Journal of Engineering Mechanics*, 115(11):2507–2525, 1989.
42. R. Karpowicz and T. Brill. The  $\beta$ - $\delta$  transformation of HMX: its thermal analysis and relationship to propellants. *AIAA Journal*, 20:1586, 1982.
43. R. Kee, J. Grcar, M. Smooke, J. Miller, and E. Meeks. Premix: a fortran program for modeling steady laminar one-dimensional premixed flames. *Sandia Rep*, 143, 01 1985.
44. L. G. Koshigoe, R. L. Shoemaker, and R. E. Taylor. Specific heat of HMX. *AIAA Journal*, 22(11):1600–1601, 1984. doi: 10.2514/3.8823. URL <https://doi.org/10.2514/3.8823>.
45. N. Kumar, K. Matouš, and P. Geubelle. Reconstruction of periodic unit cells of multimodal random particulate composites using genetic algorithms. *Computational Materials Science*, 42:352–367, 04 2008. doi: 10.1016/j.commatsci.2007.07.043.
46. P. Lamberg, R. Lehtiniemi, and A.-M. Henell. Numerical and experimental investigation of melting and freezing processes in phase change material storage. *International Journal of Thermal Sciences*, 43(3):277–287, 2004. ISSN 1290-0729. doi: <https://doi.org/10.1016/j.ijthermalsci.2003.07.001>. URL <https://www.sciencedirect.com/science/article/pii/S1290072903001303>.
47. J. H. Lambert. Observaciones variae in mathesin puram. *Acta Helvetica Physico-Mathematico-Anatomico-Bota-nico-Medica*, 3:128–168, 1758.
48. H. Laurent, A. Vandenbroucke, S. Couëdo, G. Rio, and N. A. Hocine. An hyper-visco-hysteretic model for elastomeric behaviour under low and high temperatures: Experimental and numerical investigations. *Proceedings of the 5th European Conference on Constitutive Models for Rubber, ECCMR 2007*, 01 2007.
49. E. Lee. Elastic-plastic deformations at finite strains. *Journal of Applied Mechanics*, 36:1–6, 1969.

50. V. I. Levitas, B. F. Henson, L. B. Smilowitz, and B. W. Asay. Solid-solid phase transformation via virtual melting significantly below the melting temperature. *Phys. Rev. Lett.*, 92:235702, Jun 2004. doi: 10.1103/PhysRevLett.92.235702. URL <https://link.aps.org/doi/10.1103/PhysRevLett.92.235702>.
51. D. Li, T. Jaglinski, D. S. Stone, and R. S. Lakes. Temperature insensitive negative poisson's ratios in isotropic alloys near a morphotropic phase boundary. *Applied Physics Letters*, 101(25):251903, 2012. doi: 10.1063/1.4772940. URL <https://doi.org/10.1063/1.4772940>.
52. M. Li, W.-J. Tan, B. Kang, R.-J. Xu, and W. Tang. The elastic modulus of  $\beta$ -HMX crystals determined by nanoindentation. *Propellants, Explosives, Pyrotechnics*, 35:379–383, 2010.
53. T.-C. Ling (Bill) and C. S. Poon. Use of phase change materials for thermal energy storage in concrete: An overview. *Construction and Building Materials*, 46:55–62, 09 2013. doi: 10.1016/j.conbuildmat.2013.04.031.
54. C. Liu. On the minimum size of representative volume element: An experimental investigation. *Experimental Mechanics*, 45:238–243, 06 2005. doi: 10.1007/BF02427947.
55. Y. Long and J. Chen. Theoretical study of the thermodynamic properties, phase transition wave, and phase transition velocity for octahydro-1,3,5,7-tetranitro-1,3,5,7-tetrazocine. *Journal of Applied Physics*, 118(11):115901, 2015. doi: 10.1063/1.4930812. URL <https://doi.org/10.1063/1.4930812>.
56. J. Mandel. Plasticité Classique Et Viscoplasticité : Course Held at the Department of Mechanics of Solids at Udine, September-October 1971.
57. J. McGlaun, S. Thompson, and M. Elrick. CTH: A three-dimensional shock wave physics code. *International Journal of Impact Engineering*, 10(1):351 – 360, 1990. ISSN 0734-743X. doi: [https://doi.org/10.1016/0734-743X\(90\)90071-3](https://doi.org/10.1016/0734-743X(90)90071-3). URL <http://www.sciencedirect.com/science/article/pii/0734743X90900713>.
58. F. Meissonnier, E. Busso, and N. O'Dowd. Finite element implementation of a generalised non-local rate-dependent crystallographic formulation for finite strains. *International Journal of Plasticity*, 17(4):601–640, 2001. ISSN 0749-6419. doi: [https://doi.org/10.1016/S0749-6419\(00\)00064-4](https://doi.org/10.1016/S0749-6419(00)00064-4). URL <https://www.sciencedirect.com/science/article/pii/S0749641900000644>.
59. J. A. Nairn and J. E. Guilkey. Axisymmetric form of the generalized interpolation material point method. *International journal for numerical methods in engineering*, 101(2):127–147, 2015. ISSN 0029-5981.
60. P. Newell and Y. Xi. Effect of phase-change materials on properties of concrete. *ACI Materials Journal*, 109:71–80, 01 2012.

61. R. Nikbakht and H. Assadi. Phase-field modelling of self-propagating high-temperature synthesis of nial. *Acta Materialia*, 60:4041–4053, 06 2012. doi: 10.1016/j.actamat.2012.04.017.
62. S. Paolucci. *Principles of constitutive theory*, pages 191–270. Cambridge University Press, 2016. doi: 10.1017/CBO9781316106167.006.
63. J. Powers and S. Paolucci. Accurate spatial resolution estimates for reactive supersonic flow with detailed chemistry. *AIAA JOURNAL*, 43, 04 2005. doi: 10.2514/1.11641.
64. J. M. Powers. *Combustion Thermodynamics and Dynamics*. Cambridge University Press, 2016.
65. Y. Rabin and J. Plitz. Thermal Expansion of Blood Vessels and Muscle Specimens Permeated with DMSO, DP6, and VS55 at Cryogenic Temperatures. *Annals of Biomedical Engineering*, 33:1213–28, 10 2005. doi: 10.1007/s10439-005-5364-0.
66. P. Rae, H. Goldrein, S. Palmer, J. Field, and A. Lewis. Quasi-static studies of the deformation and failure of  $\beta$ -HMX based polymer bonded explosives. In *Mathematical, Physical and Engineering Science*, volume 458, pages 743–762, 2002.
67. P. Rae, D. Hooks, and C. Liu. The stress versus strain response of single  $\beta$ -HMX crystals in quasi-static compression. *Proceedings of the 13th International Detonation Symposium, IDS 2006*, pages 293–301, 01 2006.
68. S. Ran, C. T. Wolowiec, I. Jeon, N. Pouse, N. Kanchanavatee, B. D. White, K. Huang, D. Martien, T. DaPron, D. Snow, M. Williamsen, S. Spagna, P. S. Riseborough, and M. B. Maple. Phase diagram and thermal expansion measurements on the system  $\text{URu}_{2-x}\text{Fe}_x\text{Si}_2$ . *Proceedings of the National Academy of Sciences*, 113(47):13348–13353, 2016. ISSN 0027-8424. doi: 10.1073/pnas.1616542113. URL <https://www.pnas.org/content/113/47/13348>.
69. P. Rosakis, A. Rosakis, G. Ravichandran, and J. Hodowany. A thermodynamic internal variable model for the partition of plastic work into heat and stored energy in metals. *Journal of the Mechanics and Physics of Solids*, 48(3):581 – 607, 2000. ISSN 0022-5096. doi: [https://doi.org/10.1016/S0022-5096\(99\)00048-4](https://doi.org/10.1016/S0022-5096(99)00048-4). URL <http://www.sciencedirect.com/science/article/pii/S0022509699000484>.
70. A. Saada. *Elasticity Theory and Applications*. Pergamon unified engineering series. R.E. Krieger Publishing Company, 1983. ISBN 9780898745597. URL <https://books.google.com/books?id=IIUrAAAACAAJ>.
71. S. M. Selbach, J. R. Tolchard, A. Fossdal, and T. Grande. Non-linear thermal evolution of the crystal structure and phase transitions of  $\text{LaFeO}_3$  investigated

- by high temperature X-ray diffraction. *Journal of Solid State Chemistry*, 196: 249–254, 2012. ISSN 0022-4596.
72. T. D. Sewell, R. Menikoff, D. Bedrov, and G. D. Smith. A molecular dynamics simulation study of elastic properties of HMX. *The Journal of Chemical Physics*, 119(14):7417–7426, 2003. doi: 10.1063/1.1599273. URL <https://doi.org/10.1063/1.1599273>.
  73. M. Shabouei, W. Subber, C. W. Williams, K. Matouš, and J. M. Powers. Chemo-thermal model and gaussian process emulator for combustion synthesis of Ni/Al composites. *Combustion and Flame*, 207:153–170, 2019. ISSN 0010-2180. doi: <https://doi.org/10.1016/j.combustflame.2019.05.038>. URL <http://www.sciencedirect.com/science/article/pii/S0010218019302512>.
  74. H. Shang, F. Zhao, and H. Fu. Modeling shock responses of plastic bonded explosives using material point method. *AIP Conference Proceedings*, 1793(1): 040019, 2017. doi: 10.1063/1.4971513. URL <https://aip.scitation.org/doi/abs/10.1063/1.4971513>.
  75. Y.-B. Shi, L.-F. Bai, B.-Q. Liu, G.-Y. Yan, J.-M. Song, C.-Q. Huang, G.-A. Sun, J. Gong, and X. Ju. Theoretical investigation into the influence of molar ratio on mixture system:  $\alpha$ ,  $\gamma$ ,  $\delta$ -HMX molecules coexisting with  $\beta$ -HMX crystal. *Journal of Molecular Modeling*, 25(8):213–213, 2019. ISSN 1610-2940.
  76. J. Simo. A framework for finite strain elastoplasticity based on maximum plastic dissipation and the multiplicative decomposition: Part II computational aspects. *Computational Methods in Applied Mechanics and Engineering*, 68: 1–31, 1988.
  77. J. Simo. A framework for finite strain elastoplasticity based on maximum plastic dissipation and the multiplicative decomposition: Part I continuum formulation. *Computational Methods in Applied Mechanics and Engineering*, 66: 199–219, 1988.
  78. J. Simo and T. Hughes. *Computational Inelasticity*. Springer, 1998.
  79. J. Simo and T. Hughes. *Computational Inelasticity*. Interdisciplinary Applied Mathematics. Springer New York, 2000. ISBN 9780387975207. URL <https://books.google.com/books?id=ftL2AJL8OPYC>.
  80. J. Simo and J. Ju. On continuum damage-elastoplasticity at finite strains: A computational framework. *Computational Mechanics*, 5:375–400, 1989.
  81. C. B. Skidmore, D. S. Phillips, S. F. Son, and B. W. Asay. Characterization of HMX particles in PBX 9501. *AIP Conference Proceedings*, 429, 571, 1998.
  82. W. Ślebodziński. Sur les équations de Hamilton. *Bull. Acad. Roy. Belg.(5)*, 17: 864–870, 1931.

83. L. Smilowitz, B. F. Henson, B. W. Asay, and P. M. Dickson. The  $\beta$ - $\delta$  phase transition in the energetic nitramine-octahydro-1,3,5,7-tetranitro-1,3,5,7-tetrazocine: Kinetics. *J. Chem. Phys.*, 117:3789, 2002.
84. H. K. Springer, S. Bastea, A. L. Nichols, C. M. Tarver, and J. E. Reaugh. Modeling the effects of shock pressure and pore morphology on hot spot mechanisms in HMX. *Propellants, Explosives, Pyrotechnics*, 43(8):805–817, 2018. ISSN 0721-3115.
85. K. Srinivasan, K. Matouš, and P. Guebelle. Generalized finite element method for modeling nearly incompressible bimaterial hyperelastic solids. *Computer Methods in Applied Mechanics Engineering*, 197:4882–4893, 2008.
86. K. Srinivasan, K. Matouš, P. Geubelle, and T. Jackson. Thermomechanical modeling of regressing heterogeneous solid propellants. *J. Comput. Physics*, 228:7883–7901, 11 2009. doi: 10.1016/j.jcp.2009.07.003.
87. R. Stojanović, S. Djurić, and L. Vujošević. On finite thermal deformations. *Arch. Mech. Stosow.*, 16:103–108, 1964.
88. R. Strehlow, H. Barthel, and H. Krier. Initiation, combustion and transition to detonation in homogeneous and heterogeneous reactive mixtures. Technical Report AFOSR-TR-81-0840, University of Illinois at Urbana Champaign, 1981.
89. F. Tan, S. Hosseinizadeh, J. Khodadadi, and L. Fan. Experimental and computational study of constrained melting of phase change materials (PCM) inside a spherical capsule. *International Journal of Heat and Mass Transfer*, 52(15):3464–3472, 2009. ISSN 0017-9310. doi: <https://doi.org/10.1016/j.ijheatmasstransfer.2009.02.043>. URL <https://www.sciencedirect.com/science/article/pii/S0017931009001896>.
90. G. Tarjus, P. Schaaf, and J. Talbot. Random sequential addition: A distribution function approach. *Journal of Statistical Physics*, 63(1-2):167–202, Apr. 1991. doi: 10.1007/BF01026598.
91. G. I. Taylor and H. Quinney. The latent energy remaining in a metal after cold working. *Proceedings of the Royal Society of London. Series A, Containing Papers of a Mathematical and Physical Character*, 143(849):307–326, 1934. ISSN 09501207. URL <http://www.jstor.org/stable/96095>.
92. A. Teetsov and W. McCrone. The microscopical study of polymorph stability diagrams. *Microsc. Cryst. Front.*, 15:13, 1965.
93. C. Truesdell and W. Noll. *The Non-Linear Field Theories of Mechanics*. Springer, 2004.
94. M. Čanadija and J. Brnić. Associative coupled thermoplasticity at finite strain with temperature-dependent material parameters. *International Journal of Plasticity*, 20:1851–1874, 10 2004. doi: 10.1016/j.ijplas.2003.11.016.

95. L. Vujošević and V. Lubarda. Finite-strain thermoelasticity based on multiplicative decomposition of deformation gradient. *Theoretical and Applied Mechanics*, 28–29:379–399, 2002.
96. R. Weese and A. Burnham. Coefficient of thermal expansion of the beta and delta polymorphs of HMX. *Propellants, Explosives, Pyrotechnics*, 30(5):344–350, 2005.
97. R. Weese, J. Maienschein, and C. Perrino. Kinetics of the  $\beta \rightarrow \delta$  solid-solid phase transition of HMX, octahydro-1,3,5,7-tetranitro-1,3,5,7-tetrazocine. *Thermochimica Acta*, 401:1–7, 2003.
98. A. Wemhoff and A. Burnham. Calibration of parameters in beta-delta HMX phase transformation kinetics using computer simulations. Technical Report UCRL-TR-218130, Lawrence Livermore National Laboratory, 2006.
99. C. Westbrook, Y. Mizobuchi, T. Poinsoot, P. Smith, and J. Warnatz. Computational combustion. *Proceedings of the Combustion Institute*, 30:125–157, 01 2005. doi: 10.1016/j.proci.2004.08.275.
100. T. Willey, L. Lauderbach, F. Gagliardi, T. Buuren, E. Glascoe, J. Tringe, J. Lee, H. Springer, and J. Ilavsky. Mesoscale evolution of voids and microstructural changes in HMX-based explosives during heating through the  $\beta \rightarrow \delta$  phase transition. *Journal of Applied Physics*, 118:055901, 08 2015. doi: 10.1063/1.4927614.
101. C. W. Williams and K. Matouš. Prediction of nonlinear specific heat during single crystal HMX phase transition, 2023. URL <https://arxiv.org/abs/2301.05010>.
102. C. W. Williams, K. Matouš, and G. Srivastava. Continuum Modeling Predictions of Nonlinear Specific Heat in Phase Transition of Energetic Materials, 2023. URL <https://ssrn.com/abstract=4355933>.
103. J. J. Xiao, W. R. Wang, J. Chen, G. F. Ji, W. Zhu, and H. M. Xiao. Study on structure, sensitivity and mechanical properties of hmx and hmx-based pbxs with molecular dynamics simulation. *Computational and Theoretical Chemistry*, 999:21 – 27, 2012. ISSN 2210-271X. doi: <https://doi.org/10.1016/j.comptc.2012.08.006>. URL <http://www.sciencedirect.com/science/article/pii/S2210271X1200401X>.
104. J. Yoh and K.-H. Kim. Shock compression of condensed matter using Eulerian multimaterial method: Applications to multidimensional shocks, deflagration, detonation, and laser ablation. *Journal of Applied Physics*, 103:113507, 2008.
105. J. J. Yoh and M. McClelland. *An Overview of Thermal-Chemical-Mechanical Modeling of HMX-Based Explosives*, chapter 650, pages 1–5. American Institute of Aeronautics and Astronautics, 2005. doi: 10.2514/6.2005-4554. URL <https://arc.aiaa.org/doi/abs/10.2514/6.2005-4554>.

*This document was prepared & typeset with pdfL<sup>A</sup>T<sub>E</sub>X, and formatted with  
NDdiss2<sub>ε</sub> classfile (v3.2017.2[2017/05/09])*